Supplemental Information

Stealing from a Distant Neighbor: An Unexpectedly Fast Long-Span Peroxy Radical Hydrogen-Shift Reaction in a Long-Chain Diether

Hongmin Yu [a], *Thomas Golin Almeida* [b], *Samir P. Rezgui* [c], *Vili-Taneli Salo* [b], *John D. Crounse* [a], *Brian M. Stoltz* [c], *Henrik G. Kjaergaard* [b], *Paul O. Wennberg* [*,a,d]

[a] Division of Geological and Planetary Sciences, California Institute of Technology, 1200 E. California Blvd, Pasadena, CA, 91125

[b] Department of Chemistry, University of Copenhagen, Universitetsparken 5, DK-2100 Copenhagen Ø, Denmark

[c] Division of Chemistry and Chemical Engineering, California Institute of Technology, 1200 E. California Blvd, Pasadena, CA, 91125

[d] Division of Engineering and Applied Science, California Institute of Technology, 1200 E. California Blvd, Pasadena, CA, 91125

*Correspondence to P.O. Wennberg (wennberg@caltech.edu).

Contents

1 Additional Oxidation Mechanisms and GC analysis

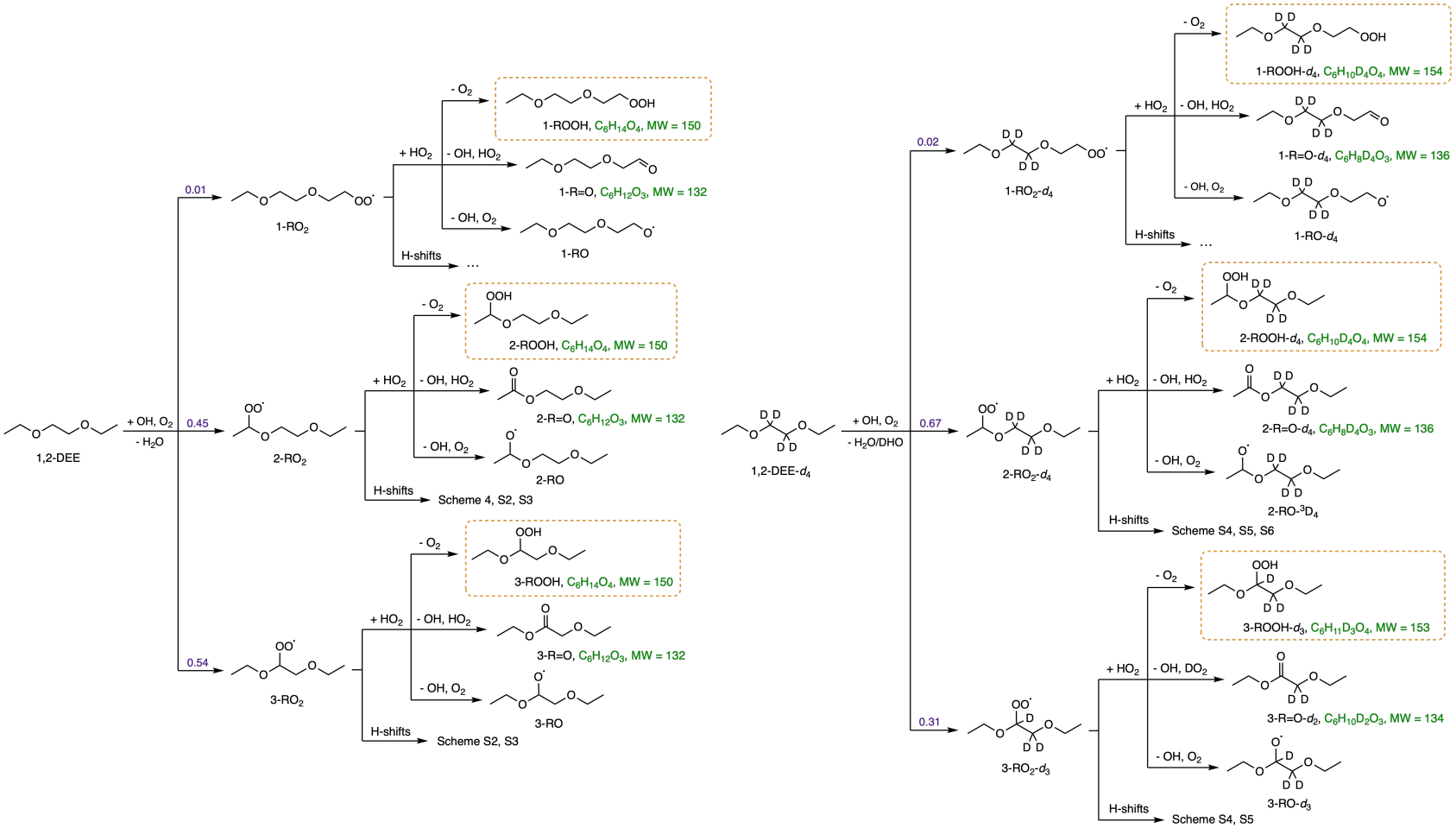

Scheme S1: Initial step of OH-initiated photo-oxidation of 1,2-DEE (left) and 1,2-DEE-d_4 (right). The branching fractions of the initial steps are denoted in purple (derived in Section S8.1). The subsequent bimolecular reactions of generated RO_2 with HO_2 and respective products are also shown. Further pathways from RO_2 H-shift reactions are shown in Fig. 4 in the main text and S2 to S6. The molecular masses of major closed-shell products are denoted in green. Products detectable by our instrument are shown in orange boxes.

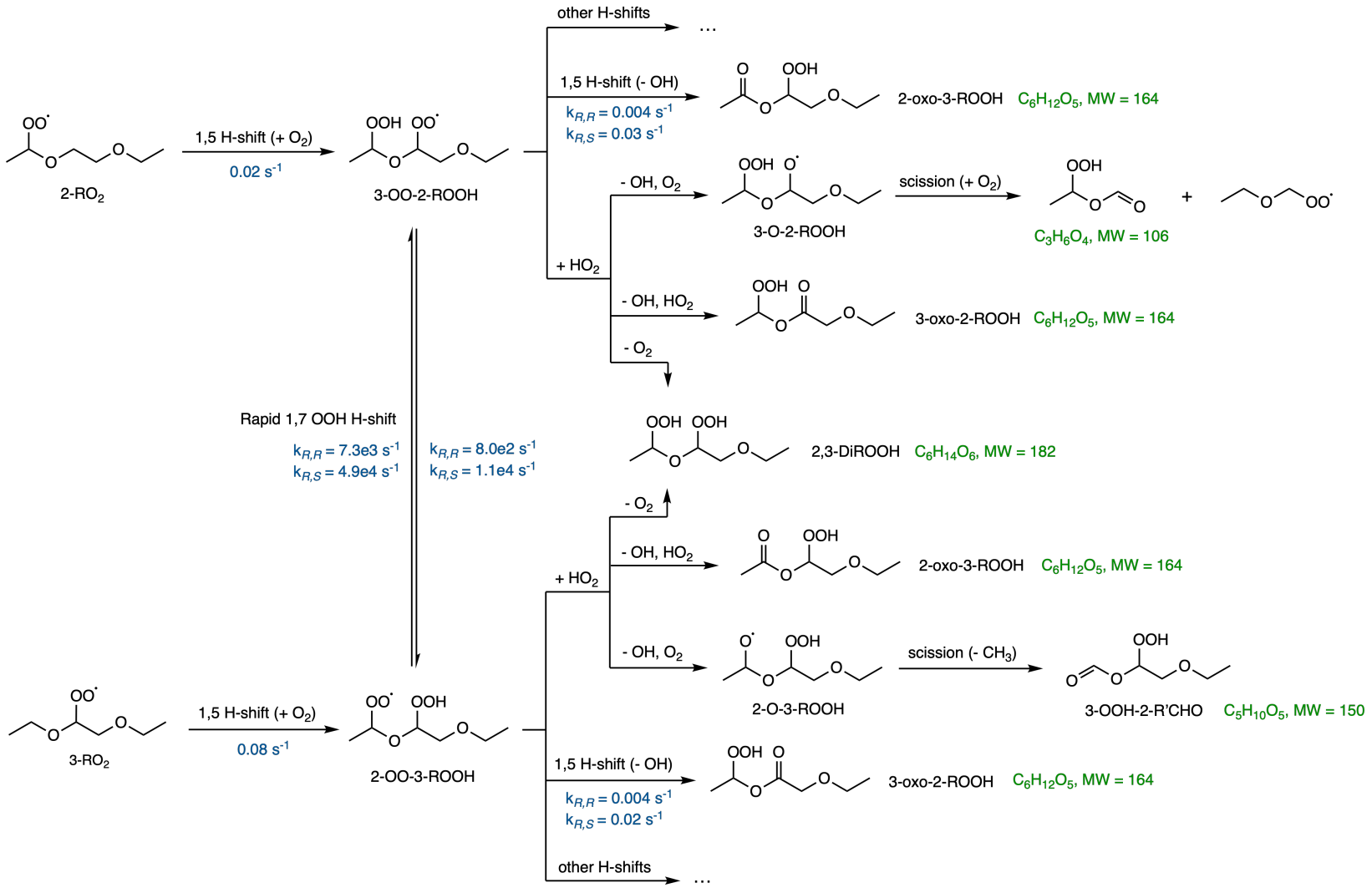

Scheme S2: Mechanism of 1,2-DEE 2-RO_2 and 3-RO_2 1,5 H-shift reactions. The H-shift rate coefficients are calculated at 294 K and denoted in blue. Subsequent reactions of generated hydroperoxy RO_2 (2-OO-3-ROOH and 3-OO-2-ROOH), including their bimolecular reaction with HO_2, unimolecular H-shift reactions, and respective products are also shown. The molecular masses of major closed-shell products are denoted in green.

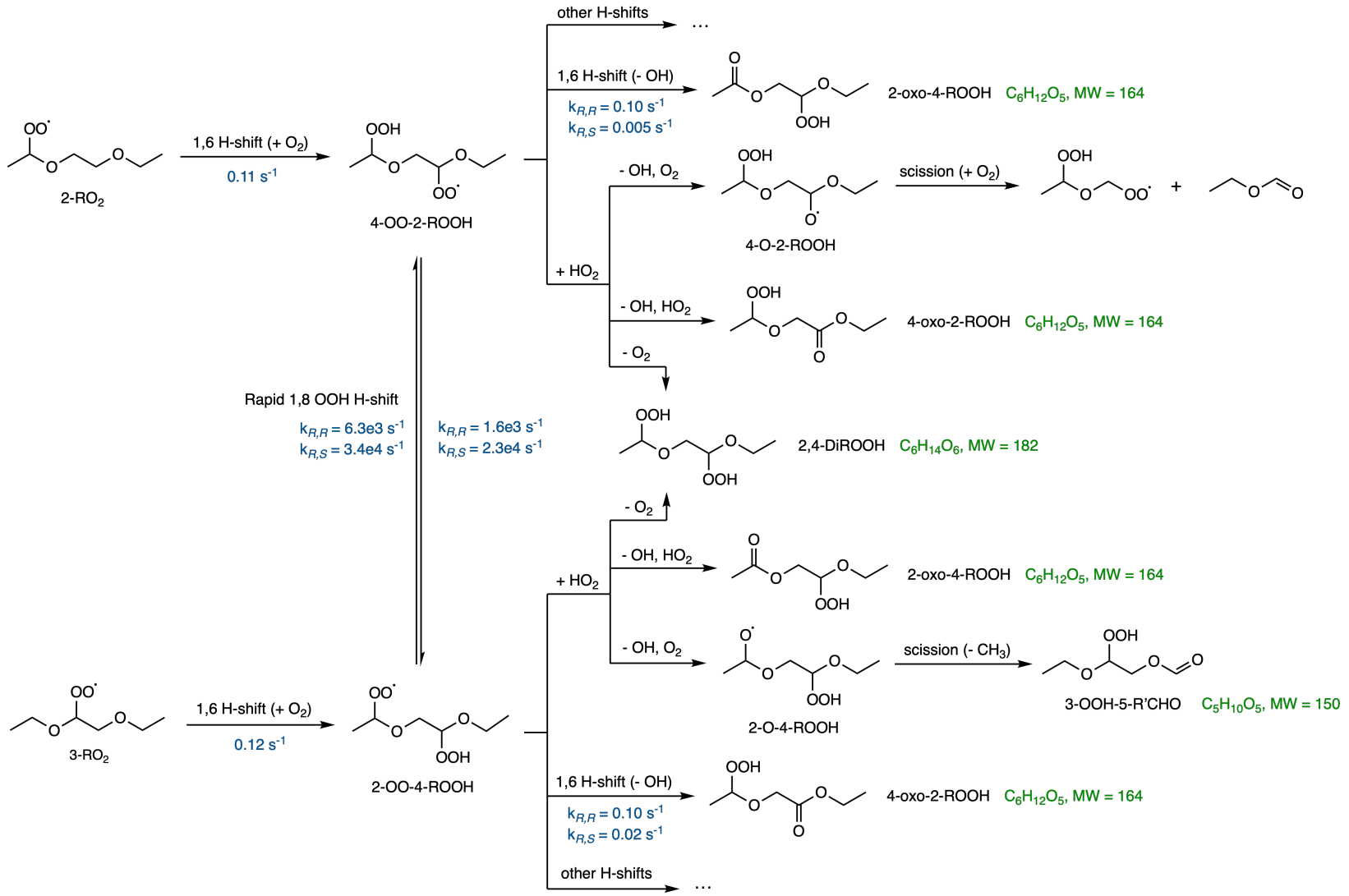

Scheme S3: Mechanism of 1,2-DEE 2-RO_2 and 3-RO_2 1,6 H-shift reactions. The H-shift rate coefficients are calculated at 294 K and denoted in blue. Subsequent reactions of generated hydroperoxy RO_2 (2-OO-4-ROOH and 4-OO-2-ROOH), including their bimolecular reaction with HO_2, unimolecular H-shift reactions, and respective products are also shown. The molecular masses of major closed-shell products are denoted in green.

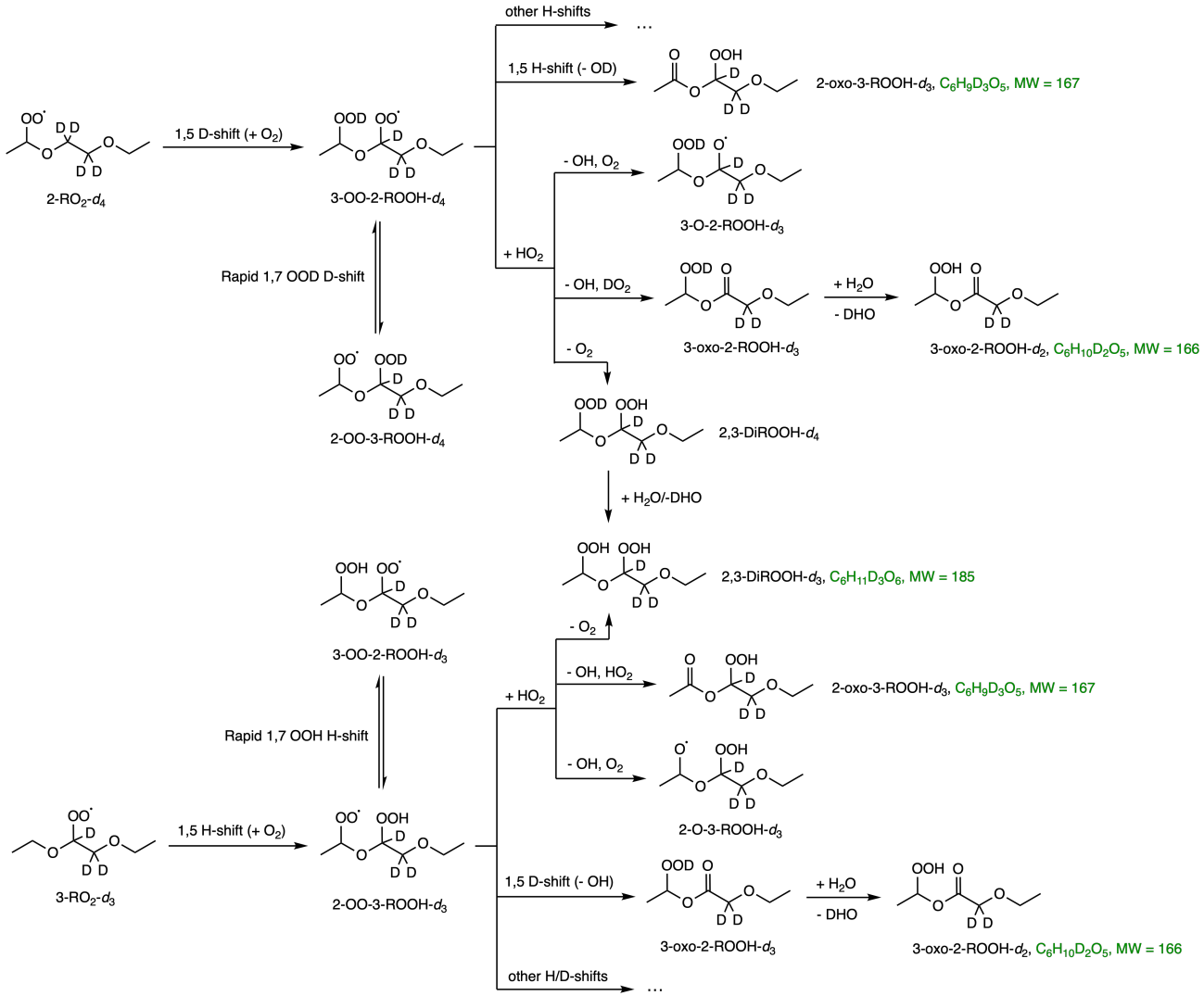

Scheme S4: Mechanism of 1,2-DEE 2-RO_2-d_4 and 3-RO_2-d_3 1,5 H-shift reactions. Subsequent reactions of generated hydroperoxy RO_2 (deuterated 2-OO-3-ROOH and 3-OO-2-ROOH), including their bimolecular reaction with HO_2, unimolecular H-shift reactions, fast H/D exchange of hydroperoxide deuterium atom ($-OOD \xrightarrow{H_2O/-DHO} -OOH$), and respective products are also shown. The molecular masses of major closed-shell products are denoted in green.

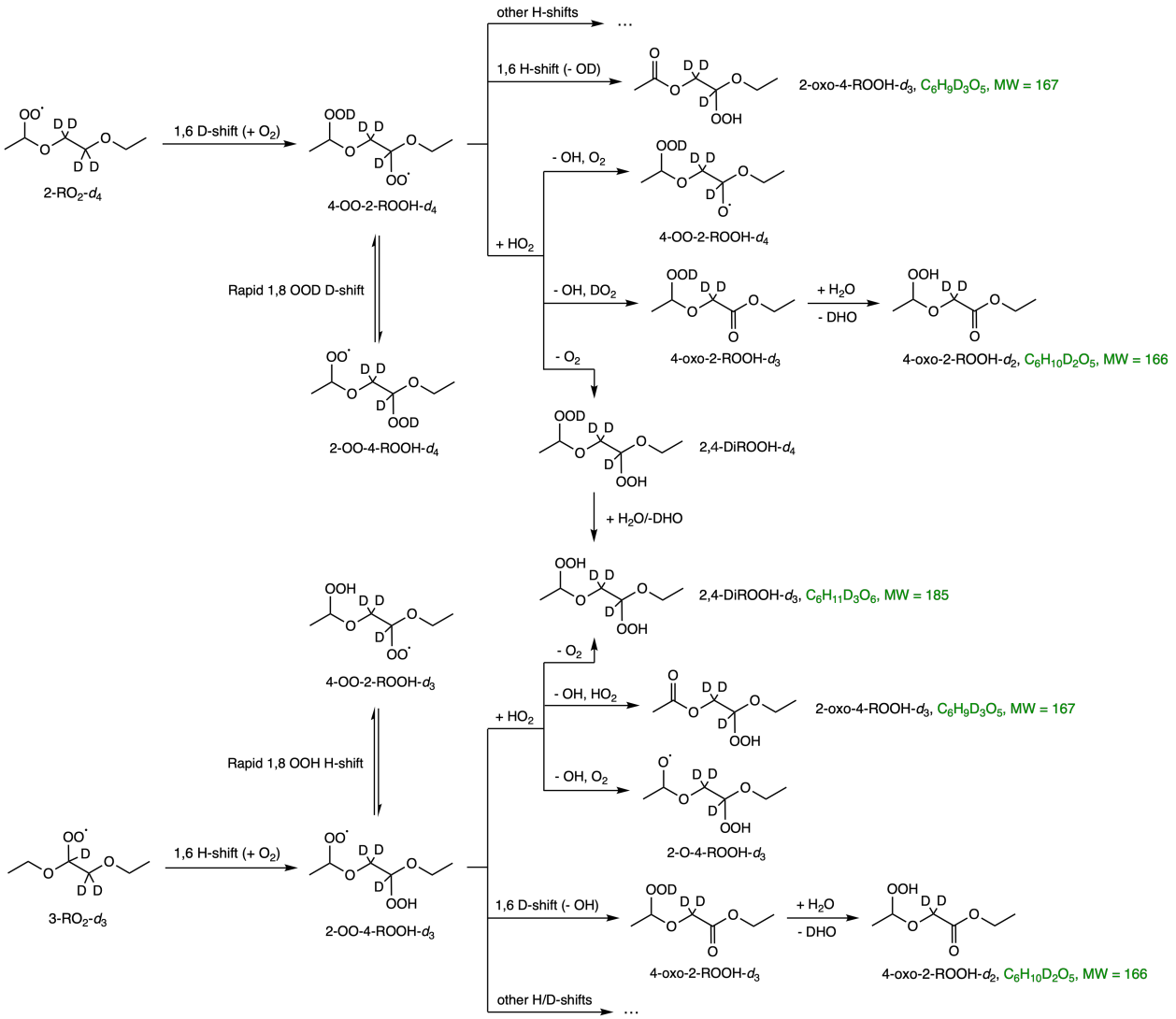

Scheme S5: Mechanism of 1,2-DEE 2-RO_2-d_4 and 3-RO_2-d_3 1,6 H-shift reactions. Subsequent reactions of generated hydroperoxy RO_2 (deuterated 2-OO-4-ROOH and 4-OO-2-ROOH), including their bimolecular reaction with HO_2, unimolecular H-shift reactions, fast H/D exchange of hydroperoxide deuterium atom ($-OOD \xrightarrow{H_2O/-DHO} -OOH$), and respective products are also shown. The molecular masses of major closed-shell products are denoted in green.

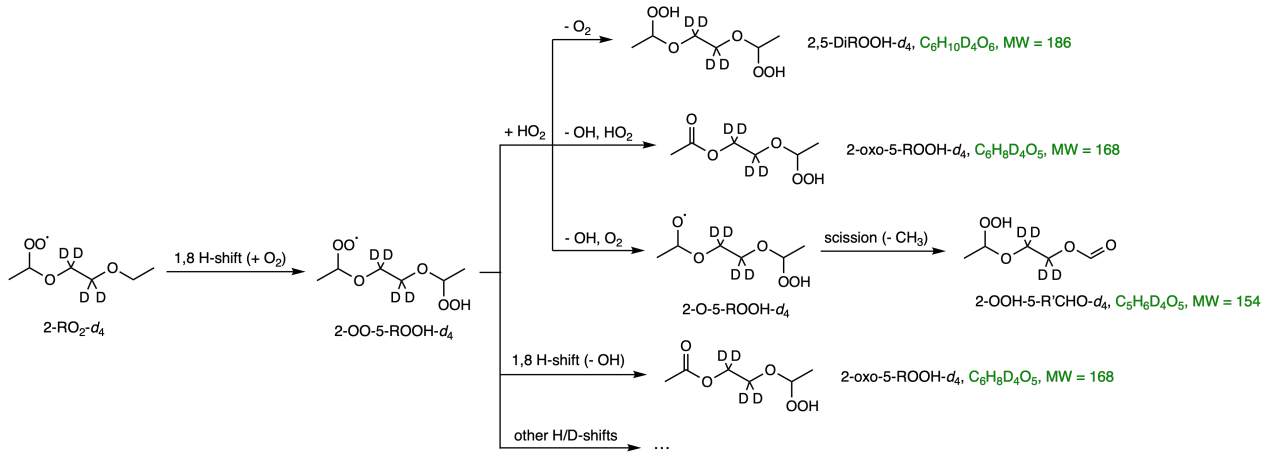

Scheme S6: Mechanism of 1,2-DEE 2-RO_2-d_4 1,8 H-shift reactions. Subsequent reactions of generated hydroperoxy RO_2 (2-OO-4-ROOH and 4-OO-2-ROOH), including their bimolecular reaction with HO_2, unimolecular H-shift reactions, and respective products are also shown. The molecular masses of major closed-shell products are denoted in green.

1.1 Gas Chromatograms

The following gas chromatograms come from 1,2-DEE oxidation experiment No.12 (Table S1) and a 1,2-DEE-d_4 oxidation experiment conducted under similar conditions.

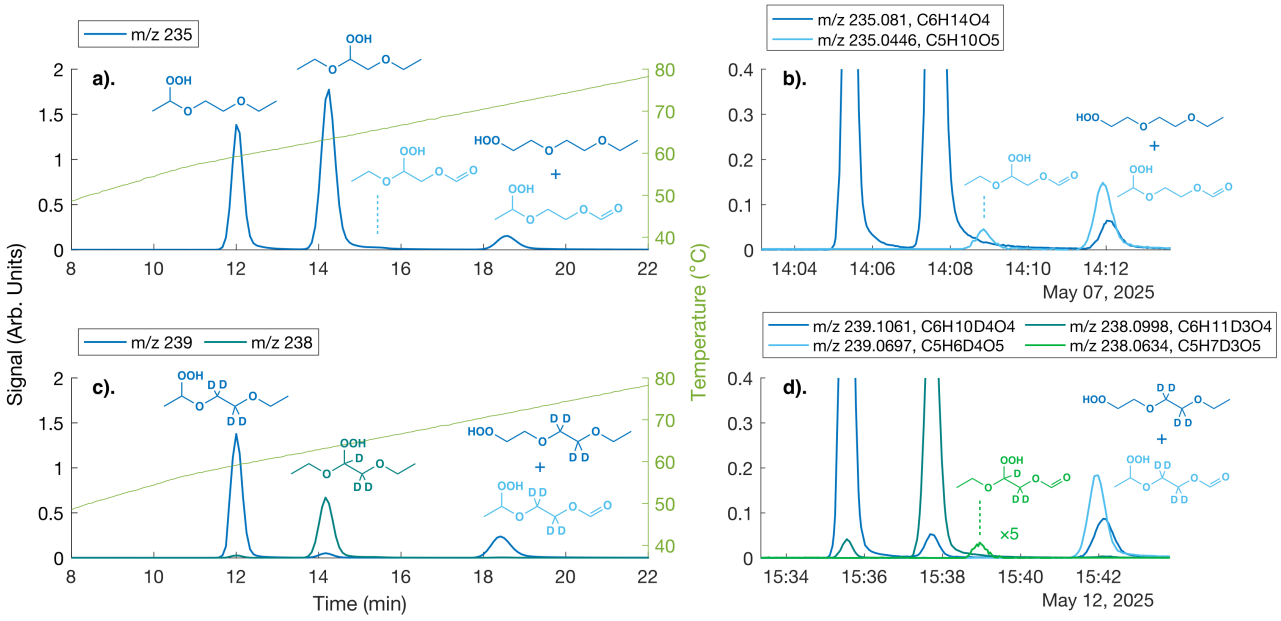

Figure S1: Gas chromatograms of ROOHs (Scheme S1) and C5 ketohydroperoxides (Fig. 4, S3, S6). **(a)** GC traces from 1,2-DEE oxidation, **(b)** Zoomed-in view of **(a)** with high-resolution mass spectrometry (HR-MS) data, **(c)** GC traces from 1,2-DEE-d_4 oxidation, **(d)** Zoomed-in view of **(c)** with HR-MS data. Certain signals are scaled up by a factor denoted in the figure. HR-MS analysis are applied to resolve the overlapping GC signals of the ROOHs, 2-OOH-5-R'CHO, and 3-OOH-5-R'CHO (tentatively assigned), and facilitate our quantification of those compounds (Table S35).

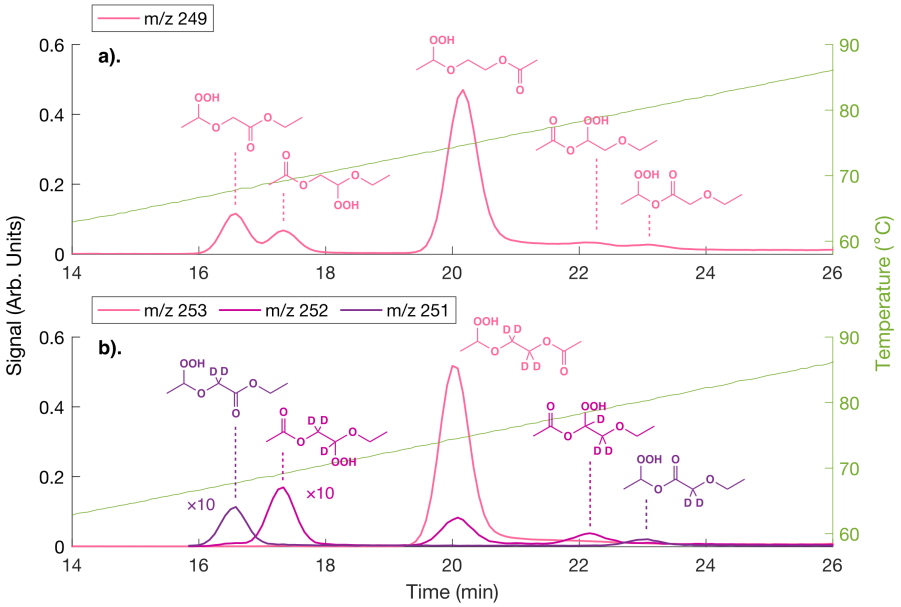

Figure S2: Gas chromatograms of C6 ketohydroperoxides. **(a)** GC traces from 1,2-DEE oxidation (Fig. 4, S2, S3), **(b)** GC traces from 1,2-DEE-d_4 oxidation (Scheme S4, S5, S6). Signals for m/z 252 and 251 are scaled up by a factor of 10 as denoted in the figure. The GC peak at m/z 252 eluting at ~20 min, ~2% of the m/z 253 peak, likely corresponds to 2-oxo-5-ROOH formed from the "non-fully deuterated" 1,2-DEE-d_3 due to the 98% isotopic purity of the ethylene glycol-d_4 used in the synthesis (see Section S2). The assignments of 2-oxo-4-ROOH vs. 2-oxo-3-ROOH (m/z 252 in **(b)**) and 4-oxo-2-ROOH vs. 3-oxo-2-ROOH (m/z 251 in **(b)**) are tentative based on calculated 1,5 and 1,6 H-shift rate coefficients of primary RO_2 (Table S3), as well as oxidation of authentic standards in Figure S3. The larger GC peaks are assigned to products from the faster 1,6 H-shifts.

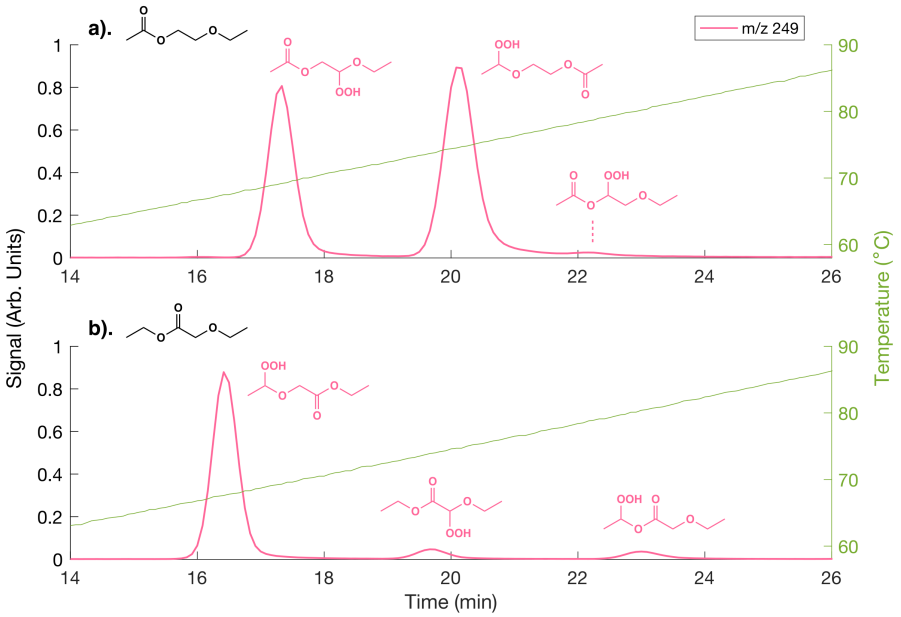

Figure S3: Gas chromatograms of oxidation of 1,2-DEE 2-R=O and 3-R=O standards at high [HO_2]. **(a)** 2-R=O, aka 2-ethoxyethyl acetate (Sigma Aldrich, 98%) **(b)** 3-R=O, aka ethyl ethoxyacetate (TCI, >95%). Peak assignments are made based on structure-activity relationship (SAR) prediction of OH reactions with those compounds[1,2] and HO_2 reactions with generated RO_2,[3] and experimental results from 1,2-DEE oxidation.

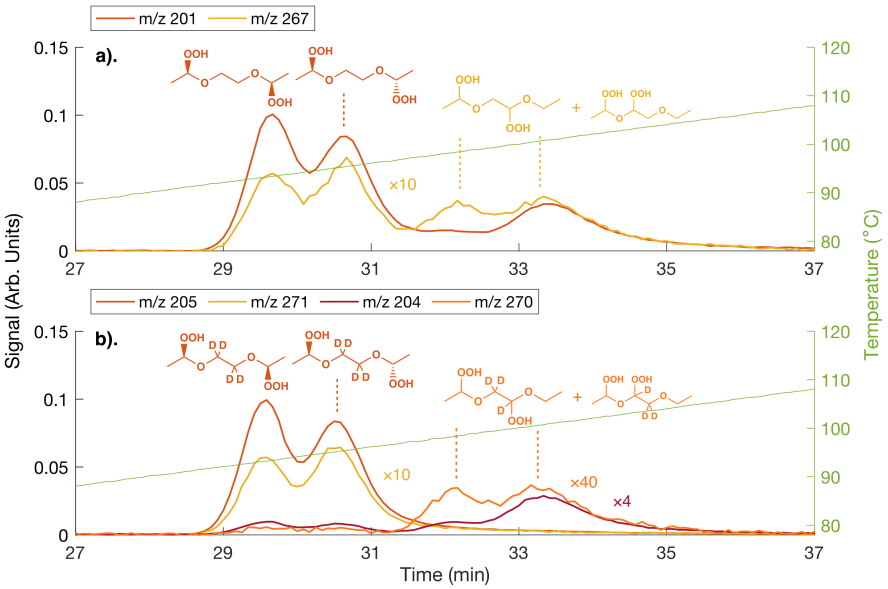

Figure S4: Gas chromatograms of dihydroperoxides (Scheme 4, S2 to S6) **(a)** GC traces from 1,2-DEE oxidation, **(b)** GC traces from 1,2-DEE-d_4. Certain signals are scaled up by a factor denoted in the figure. GC signals at m/z = mass neutral + 85 and + 19 of the products are shown. For the four GC peaks detected at m/z 204/270, the two eluting at ~30 min likely correspond to 2,5-DiROOH formed from 1,2-DEE-d_3 as discussed in Figure S2. Based on calculated 1,5 and 1,6 H-shift rate coefficients of primary RO_2, the two peaks eluting at ~33 min are attributed primarily to 2,4-DiROOH stereoisomers, with possible minor contributions from 2,3-DiROOH. Assignments of different stereoisomers of 2,5-DiROOH are tentative based on based on our expectation of the strength of the interaction between the molecule and the column. The (*R,S*) diastereomer likely has stronger intramolecular interactions between the two hydroperoxide groups which weakens the compound's interaction with the column, and thus elute earlier than the (*R,R*) diastereomer.

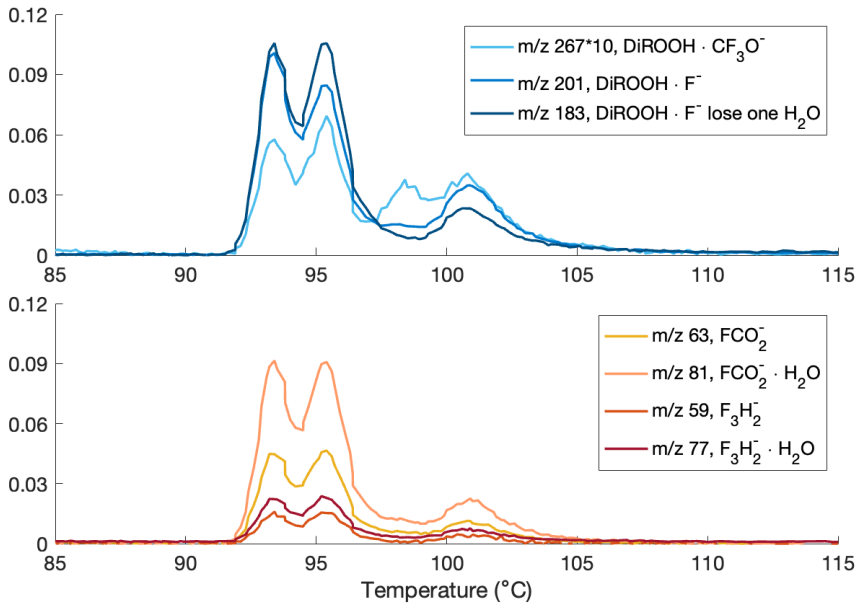

Figure S5: Gas chromatograms of major product ions of DiROOHs from 1,2-DEE oxidation. The signals of all detected product ions are summed to quantify the overall yields of DiROOHs (Table S35).

2 Synthetic Procedure

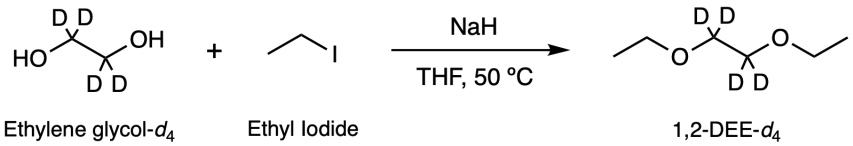

Ethylene glycol-d_4 Ethyl Iodide 1,2-DEE-d_4

Unless otherwise stated, reactions were performed in flame-dried glassware under ambient conditions using dry, deoxygenated solvents. Solvents were dried by passage through an activated alumina column under argon. Reagents were purchased from commercial sources and used as received. Ethylene glycol (D_4, 98%) was purchased from Cambridge Isotope Laboratories, Inc., and was stored in a nitrogen filled glovebox after opening. Reaction temperatures were controlled by an IKAmag temperature modulator. Thin-layer chromatography (TLC) was performed using E. Merck silica gel 60 F254 pre-coated plates (250 μm) and visualized by UV fluorescence quenching, potassium permanganate staining, or p-anisaldehyde staining. Silicycle Silia*Flash* P60 Academic Silica gel (particle size 40–63 μm) was used for flash chromatography. Mass spectra were obtained using a Hewlett Packard 5972 GC-MS system with separation on an INNOWAX column (Agilent technologies).

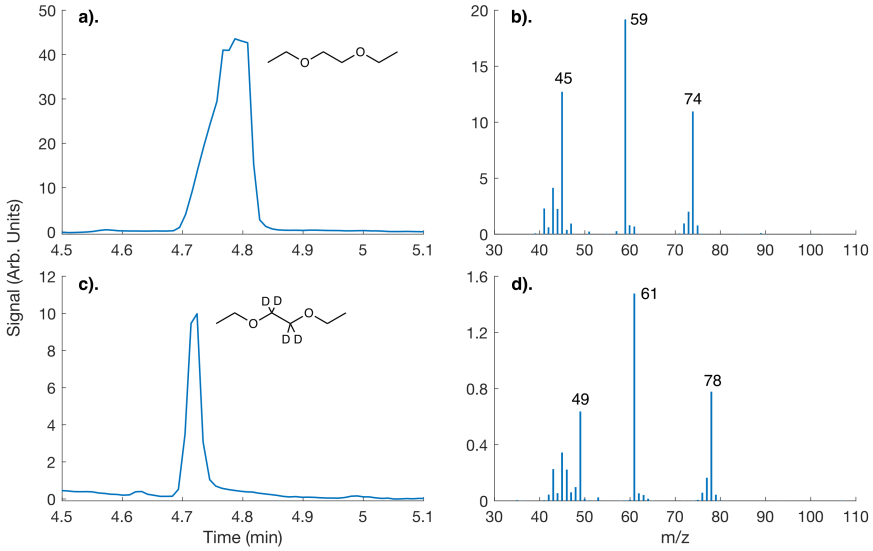

Figure S6: GC-MS spectra of **(a)** and **(b)** 1,2-DEE (authentic standard), **(c)** and **(d)** 1,2-DEE-d_4 (synthesized). Both samples are run in dicholoromethane (DCM) solution. **(a)** and **(c)** present the total ion chromatograms, with comparable retention times for the standard and the synthesized compound. **(b)** and **(d)** present the corresponding mass spectra of the GC peak, where the m/z shifts in the major fragment ions confirms successful incorporation of deuterium atoms and the identity of the synthesized compound.

To a flame dried 250 mL three-neck round bottom flask equipped with a reflux condenser was added NaH (818.0 mg, 20.45 mmol, 2.5 equiv) and THF (80 mL, 0.1M). Ethylene glycol-d_4 (EG-D4, 1.0g, 8.18 mmol, 1.0 equiv) was then added dropwise and the reaction mixture was stirred at 23 °C for 30 minutes. Ethyl iodide

(EtI, 3.19 g, 20.45 mmol, 2.5 equiv) was then added and the reaction mixture was warmed to 50 °C and stirred at this temperature for 16 h, at which point TLC analysis indicated consumption of EG-D4. Saturated aqueous NH_4Cl solution (50 mL) was slowly added to the reaction mixture, followed by Et_2O (100 mL). The reaction mixture was further diluted with water (100 mL) and the product was extracted with Et_2O (3×100 mL). The combined organic layers were washed with brine, dried over Na_2SO_4, filtered, and concentrated to near dryness to afford an ethereal solution containing 1,2-DEE-d_4 as determined by GC/MS analysis (Figure S6).

3 Experimental conditions

VOCs (1,2-DEE and CH_3OH) are transferred into the chamber through gas-tight 500 cm^3 glass bulbs. The desired mixing ratios were prepared via serial dilution using a vacuum/N_2 system, with pressure in the bulbs measured by pressure sensors (MKS 1000 and 10 Torr Baratron pressure transducers). Liquid phase reagent (H_2O_2) is added by directly evaporating a known amount of the solution into the chamber.

Table S1: Experimental conditions. All concentrations are in ppb. All experiments are conducted at ambient temperature of 294 ± 1K.

Exp. No.	$[1,2\text{-DEE}]_0$	$[CH_3OH]_0$	$[H_2O_2]_0$	Bulb type	Bulb #	Oxidation time (min)
1	337	93099	2064	350 nm	8	15
2	313	91054	2060	254 nm	8	1 2
3	429	92956	2110	254 nm	2	8
4	296	91848	2439	350 nm	2	60
5	316	93841	2166	350 nm	8	15 100
6	303	91014	2090	254 nm	1	8 12
7	297	93272	2481	350 nm	1	120 150
8	339	93506	2008	254 nm	4	2 4
9	301	91593	2044	350 nm	4	35 65
10	312	90881	2017	350 nm	2	60 80
11	306	92336	1994	254 nm	2	4 8
12	302	92682	2010	254 nm	1	8 16

Exp. No.	[1,2-DEE]$_0$	[CH_3OH]$_0$	[H_2O_2]$_0$	Bulb type	Bulb #	Oxidation time (min)
13	278	89462	1926	254 nm	8	1
						2

4 CIMS Calibration

The oxidation products are detected mainly as product ions clustered with CF_3O^- reagent ion (*m/z* 85), with a detection limit of ~10 ppt and with a 1 sec integration period. The CIMS signal for each compound is first normalized by the sum of the signals for the reagent ions, including CF_3O^- and its clusters with H_2O and H_2O_2 (detected at *m/z* 85, *m/z* 103, and *m/z* 119). Because of the high number of these reagent ions, in order to remain in a linear regime, we use the isotopologues of these reagent ion clusters at *m/z* + 1 (i.e. the clusters with $^{13}CF_3O^-$ at *m/z* 86) for normalization. Thus, the sensitivities listed in Table S2 below are normalized by the sum of *m/z* 86 + *m/z* 104 + *m/z* 120.

The instrumental sensitivities of the compounds are estimated by calculating their CF_3O^--molecule collision rate coefficients using their calculated dipole moments and polarizabilities, assuming that all collisions leads to formation of quantifiable product ions. The ion-molecule collision rate coefficients are calculated using the parameterization by Su et al.[4] The dipole moments and polarizabilities are calculated at the B3LYP/cc-pVTZ level following the method by Garden et al.[5] In summary, all conformers are generated via 3-fold of all dihedral angles, and first screened at B3LYP/6-31+G(d) level, the conformers have electronic energy within the 15 kJ/mol cut-off are further optimized at the B3LYP/cc-pVTZ level. Conformers with an electronic energy difference of less than 0.00005 Hatree and dipole moment difference of less than 0.015 Debye are recognized as duplicated conformers. Subsequently, the dipole moment and polarizability are calculated for each unique conformer at the same level. The dipole moment is calculated based on the weighted averages of the low energy conformers, and the polarizabilties are based on the lowerst-energy conformer.

The sensitivities of oxidation products listed in Table S2 are calibrated based on the calculated ion-molecule collision rate and measured sensitivity of ethylene glycol, which is chosen as the standard for determining the sensitivities of other compounds given its ability to form well-bound cluster with CF_3O^-. The CIMS sensitivity of ethylene glycol (Sigma-Aldrich, 99.8%) is determined by evaporating a known amount of ethylene glycol into the Teflon chamber and measuring the gas phase standard by the CIMS.

Table S2: Calculated dipole moments (μ_D), polarizabilities (α), CF_3O^--molecule collision rate coefficients (k_c), and CIMS sensitivities for molecules of interests in our system. [a] Normalized relative to that of ethylene glycol. [b] measured sensitivity data and uncertainties

Molecule	m/z	μ_D (D)	α (Å^3)	k_c (10^{-9} cm^3 molecule^{-1} s^{-1})	Relative k_c [a]	Sensitivity (10^{-4} cts/pptv)
Ethylene glycol 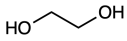	147	2.08	5.11	1.90	1	2.50 (± 0.20)[b]
3-ROOH 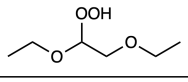	235	2.43	14.00	2.02	1.06	2.65 (± 0.21)
2-ROOH 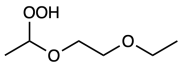	235	3.32	13.79	2.49	1.31	3.27 (± 0.26)
1-ROOH 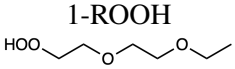	235	3.44	13.82	2.55	1.34	3.35 (± 0.27)
2-oxo-3-ROOH 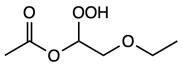	249	3.65	13.93	2.61	1.38	3.44 (± 0.28)
3-oxo-2-ROOH 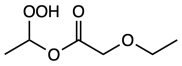	249	3.34	13.89	2.46	1.30	3.24 (± 0.26)
2-oxo-4-ROOH 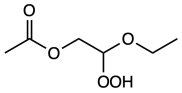	249	3.14	13.79	2.35	1.24	3.10 (± 0.25)
4-oxo-2-ROOH 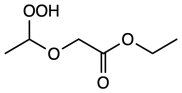	249	4.01	13.81	2.81	1.48	3.69 (± 0.30)
2-oxo-5-ROOH 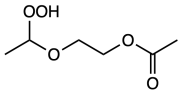	249	3.51	13.64	2.54	1.34	3.34 (± 0.27)
2-OOH-5-R'CHO 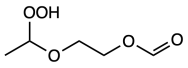	235	3.58	11.81	2.57	1.35	3.38 (± 0.27)
3-OOH-5-R'CHO 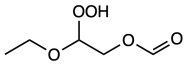	235	2.79	11.94	2.16	1.13	2.84 (± 0.23)
(*R,R*)-2,3-DiROOH 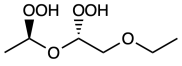	267	2.08	15.21	1.82	0.96	2.39 (± 0.19)
(*R,S*)-2,3-DiROOH 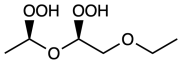	267	2.78	15.07	2.18	1.15	2.87 (± 0.23)
(*R,R*)-2,4-DiROOH 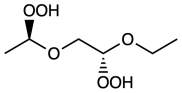	267	2.54	15.05	2.05	1.08	2.70 (± 0.22)

Molecule	m/z	μ_D (D)	α (Å^3)	k_c (10^{-9} cm^3 molecule^{-1} s^{-1})	Relative k_c	Sensitivity (10^{-4} cts/pptv)
(*R,S*)-2,4-DiROOH 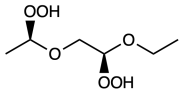	267	2.46	15.08	2.22	1.17	2.92 (± 0.23)
(*R,R*)-2,5-DiROOH 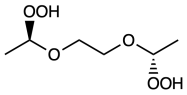	267	3.77	14.95	2.64	1.39	3.47 (± 0.28)
(*R,S*)-2,5-DiROOH 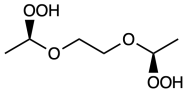	267	3.56	14.88	2.57	1.35	3.38 (± 0.27)

5 Computational Results

5.1 1,2-DEE RO_2 H-shift rate coefficients

The RO_2 H/D-shift rate coefficients $k(T)$ were calculated with a Multi-Conformer Transition State Theory (MC-TST) approach,[6,7] using Equation S1. Calculation results for first- and second-generation peroxyl radical products at the ROCCSD(T)-F12a/VDZ-F12 // ωB97X-D/aug-cc-pVTZ level of theory are shown in Table S3 and Table S4 respectively.

$$k_{MC}(T) = \kappa \frac{k_B T}{h} \frac{\sum_i^{TS} \exp\left(\frac{-\Delta E_i}{k_B T}\right) Q_{TS,i}}{\sum_j^{R} \exp\left(\frac{-\Delta E_j}{k_B T}\right) Q_{R,j}} \exp\left(\frac{-\Delta^{\ddagger} E_0}{k_B T}\right) \quad \text{(S1)}$$

Results calculated with lowest-conformer transition state theory (Equation S2) are also shown for comparison.

$$k_{LC}(T) = \kappa \frac{k_B T}{h} \frac{Q_{TS,0}}{Q_{R,0}} \exp\left(\frac{-\Delta^{\ddagger} E_0}{k_B T}\right) \quad \text{(S2)}$$

where $Q_{TS,0}$ and $Q_{R,0}$ are the lowest-confomer partition function of the transition state and reactant respectively.

The minor second-generation peroxyl radical products 2-OO-3-ROOH and 3-OO-2-ROOH are connected by a H-scrambling reaction pathway, a H-shift where the abstraction site is a hydroperoxyl group. The 2-OO-4-ROOH and 4-OO-2-ROOH isomers are connected in the same manner, via another H-scrambling pathway. Previous work,[8] suggests that H-scrambling rate coefficients calculated based on F12

energetics may be unreliable. For this reason, we report here rate coefficients calculated for these reactions at the ωB97X-D/aug-cc-pVTZ level of theory, in Table S5. The rate coefficients calculated for H-scrambling reactions are much larger than those of competing H-shifts, so that we assume an equilibrium is established between the isomers connected by these pathways as soon as either of them is formed from O_2-addition. This means that the reaction pathways directly available to one of the connected RO_2 isomers are readily available to the other, and vice-versa. Thus, the rate coefficients for these cases (shown in Table S4) were calculated assuming that the reactant is a merged-well system, where the conformers of the higher-energy RO_2 isomer are thermally accessible to the lower-energy isomer. In other words, the sum in the denominator of Equation S1 is over all conformers of both RO_2, and the reaction energy barrier $\Delta^{\ddagger}E_0$ is the zero-point corrected energy difference between the lowest-conformer of the TS and the lowest-conformer of the lowest-energy RO_2 reactant isomer.

Table S3: Reaction energy barriers ($\Delta^{\ddagger}E_0$) calculated as the zero-point corrected energy difference between the lowest-conformer of the TS and reactant, multi- and lowest-conformer TST rate coefficients (k_{MC} and k_{LC}), multi- and lowest-conformer ratio of partition functions ($Q_{TS/R,MC}$ and $Q_{TS/R,LC}$), and Eckart tunneling factor (κ), calculated at the ROCCSD(T)-F12a/VDZ-F12 // ωB97X-D/aug-cc-pVTZ level of theory and 298.15 K, for first-generation RO_2 H/D-shift reactions. α-OR and β-OR notation indicate the H-shift abstraction site.

T = 298.15 K; ROCCSD(T)-F12a/VDZ-F12 // ωB97X-D/aug-cc-pVTZ							
Reactant	**Reaction**	$\Delta^{\ddagger}E_0$ [kcal mol^{-1}]	k_{MC} [s^{-1}]	$Q_{TS/R,MC}$	k_{LC} [s^{-1}]	$Q_{TS/R,LC}$	κ
1-RO_2 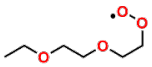	1,6 H-shift	21.68	2.36×10^{-3}	0.0253	7.11×10^{-3}	0.0762	116.2
	1,7 H-shift	19.27	2.53×10^{-2}	0.0095	7.77×10^{-2}	0.0293	56.4
	1,9 H-shift	18.55	1.39×10^{-2}	0.0013	8.53×10^{-2}	0.0080	67.9
2-RO_2 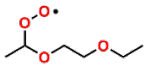	1,5 H-shift	20.50	3.18×10^{-2}	0.0928	5.99×10^{-2}	0.1746	58.5
	1,6 H-shift	18.76	1.49×10^{-1}	0.0219	5.36×10^{-1}	0.0786	62.3
	1,8 H-shift	16.85	7.03×10^{-1}	0.0052	2.99	0.0220	49.1
3-RO_2 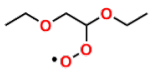	1,5 H-shift	19.87	1.08×10^{-1}	0.1102	3.60×10^{-1}	0.3687	57.3
	1,6 H-shift (α-OR)	18.55	1.52×10^{-1}	0.0126	7.59×10^{-1}	0.0631	76.3
	1,6 H-shift (β-OR)	25.42	6.84×10^{-6}	0.0550	1.37×10^{-5}	0.1102	85.9
	1,7 H-shift	24.97	2.06×10^{-6}	0.0143	6.12×10^{-6}	0.0426	46.7
1-RO_2-d_4 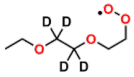	1,6 D-shift	22.73	4.76×10^{-5}	0.0246	1.40×10^{-4}	0.0723	14.3
	1,7 D-shift	20.30	7.03×10^{-4}	0.0090	2.12×10^{-3}	0.0269	9.7
	1,9 H-shift	18.46	1.58×10^{-2}	0.0013	9.70×10^{-2}	0.0078	67.9
2-RO_2-d_4 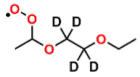	1,5 D-shift	21.61	6.77×10^{-4}	0.0873	1.31×10^{-3}	0.1693	8.6
	1,6 D-shift	19.84	3.73×10^{-3}	0.0205	1.36×10^{-2}	0.0749	10.2
	1,8 H-shift	16.82	7.31×10^{-1}	0.0051	3.15	0.0219	49.0
3-RO_2-d_3 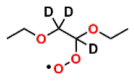	1,5 H-shift	19.83	1.38×10^{-1}	0.1326	3.80×10^{-1}	0.3642	57.3
	1,6 H-shift (α-OR)	18.47	2.07×10^{-1}	0.0152	8.45×10^{-1}	0.0620	76.2
	1,6 H-shift (β-OR)	25.38	8.82×10^{-6}	0.0663	1.45×10^{-5}	0.1091	86.0
	1,7 H-shift	24.93	2.75×10^{-6}	0.0177	6.56×10^{-6}	0.0422	46.7

Table S4: Reaction energy barriers ($\Delta^{\ddagger}E_0$) calculated as the zero-point corrected energy difference between the lowest-conformer of the TS and reactant, multi- and lowest-conformer TST rate coefficients (k_{MC} and k_{LC}), multi- and lowest-conformer ratio of partition functions ($Q_{\mathrm{TS/R},MC}$ and $Q_{\mathrm{TS/R},LC}$), and Eckart tunneling factor (κ), calculated at the ROCCSD(T)-F12a/VDZ-F12 // ωB97X-D/aug-cc-pVTZ level of theory and 298.15 K, for second-generation RO_2 H-shift reactions assuming established equilibria between 3-OO-2-ROOH and 2-OO-3-ROOH and between 4-OO-2-ROOH and 2-OO-4-ROOH via H-scrambling reactions (see Table S5).

T = 298.15 K; ROCCSD(T)-F12a/VDZ-F12 // ωB97X-D/aug-cc-pVTZ							
Reactant	**Reaction**	$\Delta^{\ddagger}E_0$ [kcal mol^{-1}]	k_{MC} [s^{-1}]	$Q_{\mathrm{TS/R},MC}$	k_{LC} [s^{-1}]	$Q_{\mathrm{TS/R},LC}$	κ
3-OO-2-ROOH 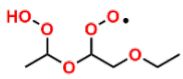	(*R,R*) 1,5 H-shift (α-OOH)	23.90	5.62×10^{-3}	2.2108	1.77×10^{-3}	0.6982	135.5
	(*R,R*) 1,6 H-shift (ζ-OOH)	20.55	5.45×10^{-2}	0.1590	2.26×10^{-2}	0.0660	63.7
	(*R,S*) 1,5 H-shift (α-OOH)	22.54	3.65×10^{-2}	0.6284	5.70×10^{-3}	0.0982	312.1
	(*R,S*) 1,6 H-shift (ζ-OOH)	19.88	1.05×10^{-1}	0.1004	1.11×10^{-1}	0.1061	63.1
2-OO-3-ROOH 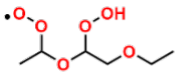	(*R,R*) 1,5 H-shift (α-OOH)	22.84	5.95×10^{-3}	0.3470	3.86×10^{-3}	0.2254	151.2
	(*R,R*) 1,6 H-shift (β-OOH)	21.23	4.39×10^{-2}	0.2592	7.20×10^{-2}	0.4249	99.6
	(*R,R*) 1,8 H-shift (δ-OOH)	18.46	5.28×10^{-1}	0.0736	6.50×10^{-1}	0.0905	39.3
	(*R,S*) 1,5 H-shift (α-OOH)	23.25	2.23×10^{-2}	1.5233	9.50×10^{-3}	0.6478	260.9
	(*R,S*) 1,6 H-shift (β-OOH)	22.90	5.55×10^{-3}	0.5635	3.97×10^{-3}	0.4032	97.1
	(*R,S*) 1,8 H-shift (δ-OOH)	19.13	1.11×10^{-1}	0.0480	2.02×10^{-1}	0.0873	39.3
4-OO-2-ROOH 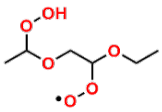	(*R,R*) 1,5 H-shift (ζ-OOH)	20.02	8.74×10^{-2}	0.0848	2.42×10^{-1}	0.2350	78.9
	(*R,R*) 1,6 H-shift (α-OOH)	21.71	1.34×10^{-1}	0.2509	3.70×10^{-1}	0.6921	702.7
	(*R,S*) 1,5 H-shift (ζ-OOH)	19.71	6.66×10^{-2}	0.0505	2.03×10^{-1}	0.1538	59.7
	(*R,S*) 1,6 H-shift (α-OOH)	22.50	6.45×10^{-3}	0.0935	2.38×10^{-2}	0.3446	343.2
2-OO-4-ROOH 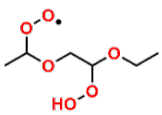	(*R,R*) 1,5 H-shift (β-OOH)	22.09	8.73×10^{-3}	0.4850	4.25×10^{-3}	0.2365	44.8
	(*R,R*) 1,6 H-shift (α-OOH)	21.31	1.29×10^{-1}	0.1383	6.17×10^{-1}	0.6619	624.7
	(*R,R*) 1,8 H-shift (γ-OOH)	20.61	1.95×10^{-2}	0.0736	4.85×10^{-2}	0.1816	54.9
	(*R,S*) 1,5 H-shift (β-OOH)	21.62	1.42×10^{-2}	0.1822	3.52×10^{-2}	0.4502	88.6
	(*R,S*) 1,6 H-shift (α-OOH)	22.25	1.98×10^{-2}	0.1662	3.77×10^{-2}	0.3156	389.5
	(*R,S*) 1,8 H-shift (γ-OOH)	19.95	2.35×10^{-2}	0.0285	1.04×10^{-1}	0.1266	56.0
2-OO-5-ROOH 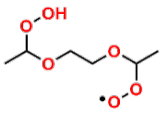	(*R,R*) 1,5 H-shift (δ-OOH)	21.03	7.88×10^{-3}	0.0997	1.01×10^{-2}	0.1273	33.0
	(*R,R*) 1,6 H-shift (γ-OOH)	20.30	1.55×10^{-2}	0.0553	3.63×10^{-2}	0.1296	34.3
	(*R,R*) 1,8 H-shift (α-OOH)	20.09	5.49×10^{-3}	0.0171	2.97×10^{-2}	0.0922	27.5
	(*R,S*) 1,5 H-shift (δ-OOH)	20.57	1.47×10^{-2}	0.0519	2.86×10^{-2}	0.1006	54.4
	(*R,S*) 1,6 H-shift (γ-OOH)	19.49	6.55×10^{-2}	0.0279	1.52×10^{-1}	0.0648	72.5
	(*R,S*) 1,8 H-shift (α-OOH)	20.80	1.17×10^{-3}	0.0118	3.81×10^{-3}	0.0383	28.3
2-OO-5-ROOH-d_4 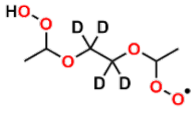	(*R,R*) 1,5 D-shift (δ-OOH)	22.16	2.29×10^{-4}	0.0988	2.86×10^{-4}	0.1233	6.6
	(*R,R*) 1,6 D-shift (γ-OOH)	21.40	5.39×10^{-4}	0.0541	1.22×10^{-3}	0.1221	7.8
	(*R,R*) 1,8 H-shift (α-OOH)	20.09	5.80×10^{-3}	0.0179	2.99×10^{-2}	0.0920	27.5
	(*R,S*) 1,5 D-shift (δ-OOH)	21.67	2.90×10^{-4}	0.0510	5.44×10^{-4}	0.0957	7.0
	(*R,S*) 1,6 D-shift (γ-OOH)	20.57	1.36×10^{-3}	0.0261	3.14×10^{-3}	0.0603	10.1
	(*R,S*) 1,8 H-shift (α-OOH)	20.78	1.20×10^{-3}	0.0116	3.96×10^{-3}	0.0382	28.2

Table S5: Reaction energy barriers ($\Delta^{\ddagger}E_0$) calculated as the zero-point corrected energy difference between the lowest-conformer of the TS and reactant, multi- and lowest-conformer TST rate coefficients (k_{MC} and k_{LC}), multi- and lowest-conformer ratio of partition functions ($Q_{\mathrm{TS/R},MC}$ and $Q_{\mathrm{TS/R},LC}$), and Eckart tunneling factor (κ), calculated at the ωB97X-D/aug-cc-pVTZ level of theory and 298.15 K, for second-generation RO_2 H-scrambling (OOH H-shift) reactions.

T = 298.15 K; ωB97X-D/aug-cc-pVTZ							
Reactant	**Reaction**	$\Delta^{\ddagger}E_0$ [kcal mol^{-1}]	k_{MC} [s^{-1}]	$Q_{\mathrm{TS/R},MC}$	k_{LC} [s^{-1}]	$Q_{\mathrm{TS/R},LC}$	κ
3-OO-2-ROOH 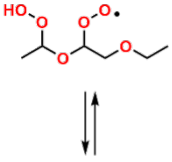	(*R*,*R*) 1,7 H-shift (-OOH)	15.41	9.95×10^{2}	0.2845	6.90×10^{2}	0.1972	111.1
	(*R*,*S*) 1,7 H-shift (-OOH)	14.30	1.30×10^{4}	0.4764	5.37×10^{3}	0.1964	133.7
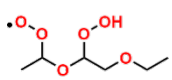							
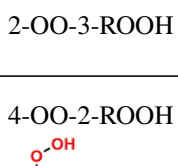 2-OO-3-ROOH	(*R*,*R*) 1,7 H-shift (-OOH)	13.63	8.49×10^{3}	0.1209	3.09×10^{4}	0.4400	111.1
	(*R*,*S*) 1,7 H-shift (-OOH)	12.02	5.56×10^{4}	0.0435	9.37×10^{4}	0.0734	133.7
4-OO-2-ROOH 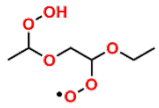	(*R*,*R*) 1,8 H-shift (-OOH)	14.52	1.95×10^{3}	0.0717	7.58×10^{3}	0.2781	193.7
	(*R*,*S*) 1,8 H-shift (-OOH)	12.95	2.63×10^{4}	0.0878	4.55×10^{4}	0.1517	150.4
							
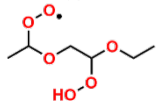	(*R*,*R*) 1,8 H-shift (-OOH)	13.48	7.19×10^{3}	0.0453	5.27×10^{4}	0.3323	193.7
2-OO-4-ROOH	(*R*,*S*) 1,8 H-shift (-OOH)	11.28	3.73×10^{4}	0.0074	1.17×10^{5}	0.0233	150.4

5.2 Temperature Dependence of RO_2 H-shift Rate Coefficients

The temperature dependence of H/D-shift rate coefficients was obtained from calculated MC-TST results over the 250-350K temperature range, fitted with a modified Arrhenius expression:

$$k(T) = A \cdot \exp\left(\frac{-E_a}{RT}\right) \cdot \exp\left(\frac{-B}{RT^3}\right) \tag{S3}$$

Fitted modified Arrhenius expression parameters A, E_a, and B are shown in Tables S6 and S7.

Table S6: Rate coefficients calculated with MC-TST at the ROCCSD(T)-F12a/VDZ-F12 // ωB97X-D/aug-cc-pVTZ level of theory, at 294 and 298.15 K, for first-generation RO_2 H/D-shift reactions. Modified Arrhenius expression parameters A, E_a, and B (Equation S3) fitted with calculated rate coefficients over the 250-350 K temperature range. α-OR and β-OR notation indicate the H-shift abstraction site.

Reactant	Reaction	k (294.00 K) [s^{-1}]	k (298.15 K) [s^{-1}]	A [s^{-1}]	E_a [kcal mol^{-1}]	B [kcal K^2 mol^{-1}]
1-RO_2 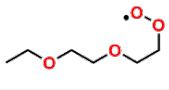	1,6 H-shift	1.67×10^{-3}	2.36×10^{-3}	1.69×10^{10}	19.13	-1.42×10^{5}
	1,7 H-shift	1.85×10^{-2}	2.53×10^{-2}	6.47×10^{9}	16.84	-1.14×10^{5}
	1,9 H-shift	1.05×10^{-2}	1.39×10^{-2}	1.01×10^{9}	16.26	-1.28×10^{5}
2-RO_2 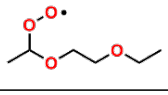	1,5 H-shift	2.27×10^{-2}	3.18×10^{-2}	4.06×10^{11}	19.76	-1.68×10^{5}
	1,6 H-shift	1.11×10^{-1}	1.49×10^{-1}	2.16×10^{10}	16.66	-1.28×10^{5}
	1,8 H-shift	5.50×10^{-1}	7.03×10^{-1}	3.12×10^{9}	14.56	-1.24×10^{5}
3-RO_2 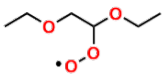	1,5 H-shift	7.82×10^{-2}	1.08×10^{-1}	2.42×10^{11}	18.54	-1.50×10^{5}
	1,6 H-shift (α-OR)	1.15×10^{-1}	1.52×10^{-1}	1.75×10^{10}	16.78	-1.50×10^{5}
	1,6 H-shift (β-OR)	4.53×10^{-6}	6.84×10^{-6}	6.00×10^{10}	23.19	-1.29×10^{5}
	1,7 H-shift	1.30×10^{-6}	2.06×10^{-6}	7.79×10^{9}	22.25	-8.89×10^{4}
1-RO_2-$^3D_4$ 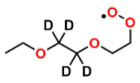	1,6 D-shift	3.10×10^{-5}	4.76×10^{-5}	9.19×10^{10}	22.30	-1.28×10^{5}
	1,7 D-shift	4.78×10^{-4}	7.03×10^{-4}	1.44×10^{10}	19.07	-8.05×10^{4}
	1,9 H-shift	1.19×10^{-2}	1.58×10^{-2}	8.36×10^{8}	15.96	-1.19×10^{5}
2-RO_2-$^3D_4$ 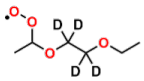	1,5 D-shift	4.43×10^{-4}	6.77×10^{-4}	3.53×10^{11}	21.17	-9.70×10^{4}
	1,6 D-shift	2.57×10^{-3}	3.73×10^{-3}	4.05×10^{10}	18.82	-9.23×10^{4}
	1,8 H-shift	5.37×10^{-1}	7.31×10^{-1}	4.07×10^{9}	14.81	-1.34×10^{5}
3-RO_2-$^3D_3$ 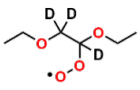	1,5 H-shift	1.00×10^{-1}	1.38×10^{-1}	4.19×10^{11}	18.73	-1.51×10^{5}
	1,6 H-shift (α-OR)	1.56×10^{-1}	2.07×10^{-1}	2.73×10^{10}	16.84	-1.48×10^{5}
	1,6 H-shift (β-OR)	5.58×10^{-6}	8.82×10^{-6}	4.54×10^{10}	22.54	-9.82×10^{4}
	1,7 H-shift	1.73×10^{-6}	2.75×10^{-6}	4.72×10^{10}	23.66	-1.35×10^{5}

Table S7: Rate coefficients calculated with MC-TST at the ROCCSD(T)-F12a/VDZ-F12 // ωB97X-D/aug-cc-pVTZ level of theory, at 294 and 298.15 K, for second-generation RO_2 H-shift reactions. Modified Arrhenius expression parameters A, E_a, and B (Equation S3) fitted with calculated rate coefficients over the 250-350 K temperature range.

Reactant	Reaction	k (294.00 K) [s^{-1}]	k (298.15 K) [s^{-1}]	A [s^{-1}]	E_a [kcal mol^{-1}]	B [kcal K^2 mol^{-1}]
3-OO-2-ROOH 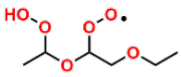	(*R,R*) 1,5 H-shift (α-OOH)	3.90×10^{-3}	5.62×10^{-3}	1.06×10^{13}	23.49	-2.36×10^{5}
	(*R,R*) 1,6 H-shift (ζ-OOH)	3.86×10^{-2}	5.45×10^{-2}	3.53×10^{11}	18.99	-1.34×10^{5}
	(*R,S*) 1,5 H-shift (α-OOH)	2.68×10^{-2}	3.65×10^{-2}	4.66×10^{12}	22.43	-2.83×10^{5}
	(*R,S*) 1,6 H-shift (ζ-OOH)	7.69×10^{-2}	1.05×10^{-1}	2.46×10^{10}	16.61	-9.79×10^{4}
2-OO-3-ROOH 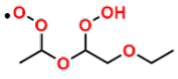	(*R,R*) 1,5 H-shift (α-OOH)	4.18×10^{-3}	5.95×10^{-3}	6.61×10^{12}	23.28	-2.45×10^{5}
	(*R,R*) 1,6 H-shift (β-OOH)	3.12×10^{-2}	4.39×10^{-2}	1.53×10^{11}	18.46	-1.19×10^{5}
	(*R,R*) 1,8 H-shift (δ-OOH)	3.87×10^{-1}	5.28×10^{-1}	6.25×10^{10}	16.11	-8.95×10^{4}
	(*R,S*) 1,5 H-shift (α-OOH)	1.62×10^{-2}	2.23×10^{-2}	8.73×10^{12}	23.14	-2.87×10^{5}
	(*R,S*) 1,6 H-shift (β-OOH)	3.80×10^{-3}	5.55×10^{-3}	5.71×10^{11}	20.71	-1.42×10^{5}
	(*R,S*) 1,8 H-shift (δ-OOH)	8.12×10^{-2}	1.11×10^{-1}	1.53×10^{10}	16.16	-8.52×10^{4}
4-OO-2-ROOH 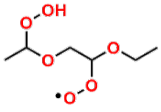	(*R,R*) 1,5 H-shift (ζ-OOH)	6.39×10^{-2}	8.74×10^{-2}	6.82×10^{10}	17.69	-1.30×10^{5}
	(*R,R*) 1,6 H-shift (α-OOH)	1.04×10^{-1}	1.34×10^{-1}	9.07×10^{10}	18.84	-2.40×10^{5}
	(*R,S*) 1,5 H-shift (ζ-OOH)	4.99×10^{-2}	6.66×10^{-2}	6.00×10^{9}	16.31	-1.22×10^{5}
	(*R,S*) 1,6 H-shift (α-OOH)	4.91×10^{-3}	6.45×10^{-3}	1.61×10^{11}	21.65	-3.00×10^{5}
2-OO-4-ROOH 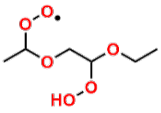	(*R,R*) 1,5 H-shift (β-OOH)	5.88×10^{-3}	8.73×10^{-3}	7.14×10^{11}	20.17	-1.06×10^{5}
	(*R,R*) 1,6 H-shift (α-OOH)	1.01×10^{-1}	1.29×10^{-1}	4.35×10^{10}	18.53	-2.49×10^{5}
	(*R,R*) 1,8 H-shift (γ-OOH)	1.39×10^{-2}	1.95×10^{-2}	2.90×10^{10}	17.73	-9.98×10^{4}
	(*R,S*) 1,5 H-shift (β-OOH)	1.02×10^{-2}	1.42×10^{-2}	2.96×10^{11}	20.20	-1.81×10^{5}
	(*R,S*) 1,6 H-shift (α-OOH)	1.51×10^{-2}	1.98×10^{-2}	7.30×10^{10}	19.98	-2.52×10^{5}
	(*R,S*) 1,8 H-shift (γ-OOH)	1.71×10^{-2}	2.35×10^{-2}	9.27×10^{9}	17.11	-1.14×10^{5}
2-OO-5-ROOH 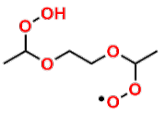	(*R,R*) 1,5 H-shift (δ-OOH)	5.37×10^{-3}	7.88×10^{-3}	4.87×10^{11}	20.18	-1.18×10^{5}
	(*R,R*) 1,6 H-shift (γ-OOH)	1.08×10^{-2}	1.55×10^{-2}	1.02×10^{11}	18.61	-1.00×10^{5}
	(*R,R*) 1,8 H-shift (α-OOH)	3.78×10^{-3}	5.49×10^{-3}	1.99×10^{11}	19.90	-1.24×10^{5}
	(*R,S*) 1,5 H-shift (δ-OOH)	1.05×10^{-2}	1.47×10^{-2}	1.50×10^{12}	21.49	-2.12×10^{5}
	(*R,S*) 1,6 H-shift (γ-OOH)	4.79×10^{-2}	6.55×10^{-2}	3.16×10^{11}	19.43	-1.89×10^{5}
	(*R,S*) 1,8 H-shift (α-OOH)	8.08×10^{-4}	1.17×10^{-3}	9.76×10^{11}	22.68	-2.07×10^{5}
2-OO-5-ROOH-d_4 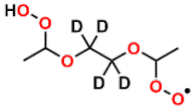	(*R,R*) 1,5 D-shift (δ-OOH)	1.45×10^{-4}	2.29×10^{-4}	1.27×10^{12}	22.53	-9.43×10^{4}
	(*R,R*) 1,6 D-shift (γ-OOH)	3.50×10^{-4}	5.39×10^{-4}	1.44×10^{11}	20.43	-6.58×10^{4}
	(*R,R*) 1,8 H-shift (α-OOH)	3.99×10^{-3}	5.80×10^{-3}	2.19×10^{11}	19.96	-1.28×10^{5}
	(*R,S*) 1,5 D-shift (δ-OOH)	1.85×10^{-4}	2.90×10^{-4}	1.44×10^{12}	22.67	-1.12×10^{5}
	(*R,S*) 1,6 D-shift (γ-OOH)	9.05×10^{-4}	1.36×10^{-3}	2.50×10^{11}	20.62	-1.03×10^{5}
	(*R,S*) 1,8 H-shift (α-OOH)	8.29×10^{-4}	1.20×10^{-3}	6.93×10^{11}	22.33	-1.95×10^{5}

5.3 Octane- and Ethoxypentane-derived RO_2 H-shift Rate Coefficients

H-shift reaction rate coefficients for three additional peroxyl radicals, one derived from octane (OCT 2-RO_2) and two derived from ethoxypentane (EP 2-RO_2 and EP 7-RO_2), were calculated with the same methods as the ones used for DEE RO_2 H-shifts. Calculation results for these systems are shown in Table S8. Results for DEE 2-RO_2 are included for comparison.

Analysis of the calculation results for RO_2 H-shift reactions in Figure S7 suggests that the difference in selectivity observed for ether- and hydrocarbon-derived RO_2 is not due to entropic factors, given that the ratio of partition functions $Q_{\mathrm{TS/R},MC}$ (third term in Equation S1) decreases with increasing span in a similar fashion in all systems. In fact, there is a slight increase in $Q_{\mathrm{TS/R},MC}$ when going from a 1,7 to a 1,8 span in OCT 2-RO_2. The increase in entropic penalty due to the loss of many internal rotors in the transition state of the longer-span pathway (as seen from the lowest-conformer ratio of partition functions $Q_{\mathrm{TS/R},LC}$) is partly counteracted by an increase in conformational entropy, likely due to a relaxation in angle and/or torsional ring-strain. This indicates that the selectivity differences among systems are controlled by differences in reaction energy barrier heights. Here, we explore how inductive, stereoelectronic, and steric effects impact this selectivity.

Previous studies[9,10] suggested that the altered intramolecular H-shift selectivity observed when different (endocyclic) functional groups are present in the ring-like transition states may be partly due to geometrical factors and stereoelectronic constraints. As endocyclic bond lengths and angles differ with substitution at the substrate's backbone, the H-shift spans at which optimal orbital interactions are possible may also change. In the case of RO_2 H-shifts, optimal overlap between the singly-occupied molecular orbital (SOMO) and the σ_{CH} orbital, required for the reaction to take place, occur with a O−−H−−C angle of ∼180° and a C−O−O−−H dihedral angle of ∼90°. As the H-shift span increases from 1,4 to 1,8, geometrical constraints imposed by (angle) ring-strain relax, so that the reacting functional groups can more easily orient themselves to maximize the overlap between the SOMO and σ_{CH} orbital. As seen from Table S9, the O−−H−−C angle and the C−O−O−−H dihedral angle in the TS deviate less from their optimum as the H-shift span increases. However, the trends are very similar for ether and hydrocarbon-derived RO_2. We conclude, therefore, that stereoelectronic effects due to differing geometrical constraints are not significant enough to explain why the selectivity towards the 1,8 H-shift is so large for DEE 2-RO_2 in comparison to OCT 2-RO_2.

Table S8: Reaction energy barriers ($\Delta^{\ddagger}E_0$) calculated as the zero-point corrected energy difference between the lowest-conformer of the TS and reactant, multi- and lowest-conformer TST rate coefficients (k_{MC} and k_{LC}), multi- and lowest-conformer ratio of partition functions ($Q_{TS/R,MC}$ and $Q_{TS/R,LC}$), and Eckart tunneling factor (κ), calculated at the ROCCSD(T)-F12a/VDZ-F12 // ωB97X-D/aug-cc-pVTZ level of theory and 298.15 K, for H-shift reactions available to OCT 2-RO_2, DEE 2-RO_2, EP 2-RO_2, and EP 7-RO_2.

T = 298.15 K; ROCCSD(T)-F12a/VDZ-F12 // ωB97X-D/aug-cc-pVTZ							
Reactant	**Reaction**	$\Delta^{\ddagger}E_0$ [kcal mol^{-1}]	k_{MC} [s^{-1}]	$\frac{\Sigma Q_{TS}}{\Sigma Q_R}$	k_{LC} [s^{-1}]	$\frac{Q_{TS}}{Q_R}$	κ
DEE 2-RO_2	1,5 H-shift	20.50	2.93×10^{-2}	0.0853	5.99×10^{-2}	0.1746	58.5
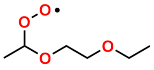	1,6 H-shift	18.76	1.47×10^{-1}	0.0215	5.36×10^{-1}	0.0786	62.3
	1,8 H-shift	16.85	6.94×10^{-1}	0.0051	2.99	0.0220	49.1
EP 2-RO_2	1,5 H-shift	19.07	1.37×10^{-1}	0.0541	1.94×10^{-1}	0.0768	38.5
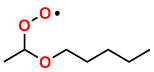	1,6 H-shift	21.25	1.28×10^{-3}	0.0124	4.58×10^{-3}	0.0447	62.3
	1,7 H-shift	20.28	4.49×10^{-3}	0.0094	9.27×10^{-3}	0.0193	56.2
	1,8 H-shift	20.21	1.23×10^{-3}	0.0038	5.74×10^{-3}	0.0177	34.1
EP 7-RO_2	1,4 H-shift	33.18	4.22×10^{-9}	0.1926	5.65×10^{-9}	0.2579	7328.8
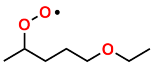	1,5 H-shift	23.79	9.28×10^{-5}	0.0894	7.45×10^{-5}	0.0718	46.1
	1,6 H-shift	19.17	5.83×10^{-2}	0.0230	1.78×10^{-1}	0.0699	45.7
	1,8 H-shift	20.07	4.23×10^{-3}	0.0045	1.36×10^{-2}	0.0144	78.4
OCT 7-RO_2	1,4 H-shift	32.76	1.47×10^{-8}	0.2727	2.04×10^{-8}	0.3790	8857.6
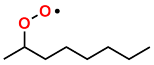	1,5 H-shift	22.13	1.59×10^{-3}	0.0940	2.73×10^{-3}	0.1615	45.7
	1,6 H-shift	21.83	8.71×10^{-4}	0.0278	2.58×10^{-3}	0.0824	50.6
	1,7 H-shift	21.45	5.24×10^{-4}	0.0084	1.32×10^{-3}	0.0213	53.2
	1,8 H-shift	23.62	3.50×10^{-5}	0.0090	5.19×10^{-5}	0.0134	129.0

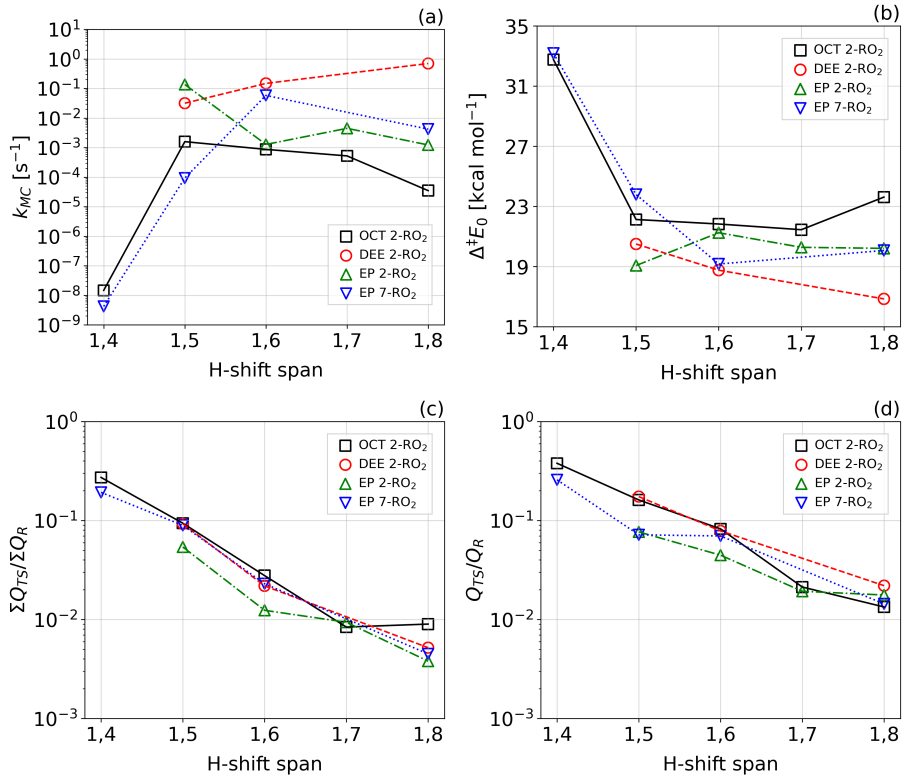

Figure S7: Calculation results for H-shift reactions available to OCT 2-RO$_2$, DEE 2-RO$_2$, EP 2-RO$_2$, and EP 7-RO$_2$, at the ROCCSD(T)-F12a/VDZ-F12 // ωB97X-D/aug-cc-pVTZ level of theory and 298.15 K. **(a)** Multi-conformer reaction rate coefficients k_{MC}; **(b)** Reaction energy barriers $\Delta^{\ddagger}E_0$ calculated as the zero-point corrected energy difference between the lowest-conformer of the TS and reactant; **(c)** Multi-confomer ratio of partion functions $Q_{\mathrm{TS/R},MC}$ (third term in Equation S1); **(d)** Lowest-conformer ratio of partition functions $Q_{\mathrm{TS/R},LC}$.

Table S9: Angles ($\angle$) and dihedral angles (ϕ) related to the proper overlap between n_O and σ^*_{CH} or σ_{CH} orbitals, in optimized geometries calculated at the ωB97X-D/aug-cc-pVTZ level of theory, for OCT 2-RO$_2$, DEE 2-RO$_2$, EP 2-RO$_2$, and EP 7-RO$_2$ H-shift transition states.

System	Species	$\angle$ O−−H−−C	ϕ C−O−O−−H	ϕ C−O−C−−H
DEE 2-RO$_2$	1,5 H-shift TS	146.2°	-49.5°	33.8°
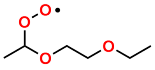	1,6 H-shift TS	158.6°	-72.1°	72.4°
	1,8 H-shift TS	176.9°	82.4°	-81.9°
EP 2-RO$_2$	1,5 H-shift TS	145.9°	-50.1°	34.9°
	1,6 H-shift TS	159.0°	-72.3°	—
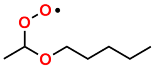	1,7 H-shift TS	168.2°	82.0°	—
	1,8 H-shift TS	176.6°	-96.1°	—
EP 7-RO$_2$	1,4 H-shift TS	133.4°	-34.6°	—
	1,5 H-shift TS	152.6°	-53.7°	—
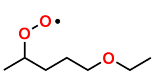	1,6 H-shift TS	161.2°	-75.5°	-65.5°
	1,8 H-shift TS	173.7°	-100.1°	-62.9°
OCT 7-RO$_2$	1,4 H-shift TS	133.5°	-34.4°	—
	1,5 H-shift TS	152.6°	-52.9°	—
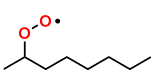	1,6 H-shift TS	161.9°	-75.7°	—
	1,7 H-shift TS	169.2°	-88.5°	—
	1,8 H-shift TS	171.9°	95.8°	—

5.4 Local Electrophilicity Indices

The effect of induction by distal oxyl groups on H-shift energy barriers was probed with site-selective differences in a local electrophilicity index $\Delta\omega^+$.[11,12] To the extent that polar effects affect H-shift transition states' relative stability, the intramolecular attack of an electrophilic radical center (such as the peroxyl group in RO_2) should be selective towards abstraction sites leading to more nucleophilic radical products (i.e. in reactions with more negative $\Delta\omega^+$ values), as per the principle of polarity-match.[13,14] This index difference $\Delta\omega^+$ is calculated from the global electrophilicity index ω and the condensed Fukui function for nucleophilic attack $f^+(\mathrm{X})$ at the radical-center X. The former is obtained as follows:[15]

$$\omega = \frac{\mu^2}{2\eta} \tag{S4}$$

where μ is the electronic chemical potential and η is the absolute chemical hardness of the species,[16,17] which are in turn calculated with Equations S5 and S6:

$$\mu = -\chi = \frac{-(I + A)}{2} \tag{S5}$$

$$\eta = I - A \tag{S6}$$

where χ is the absolute electronegativity, I is the vertical ionization potential, and A is the vertical electron affinity. These values were obtained from single-point calculations done for a cationic $(N-1)$ and an anionic $(N+1)$ electronic configuration, at the optimized geometry of the neutral species:

$$I = E_{N-1} - E_N \tag{S7}$$

$$A = E_N - E_{N+1} \tag{S8}$$

where E is the electronic energy and N is the number of electrons in the radical. The structure of the H-shift products (QOOH) were obtained by redrawing the geometry of the reactant's lowest-energy conformer, removing a hydrogen atom from the abstraction site and replacing the peroxyl group by a hydroperoxyl group, and re-optimizing the geometry at the same level of theory.

The Fukui function for nucleophilic attack f^+ is a local measure of the electrophilic power of a given attack site in a molecule, and describes the local change in electron density as a response to the addition of electrons to the system.[18] The best attack sites will see the largest relative increase in electron density upon interaction with a nucleophile, and will therefore display a larger value of f^+. Using the finite differences approximation,[19] the Fukui function $f^+(\mathrm{X})$ condensed onto the radical center X is calculated as the local electron density difference between the anionic $(N + 1)$ and the neutral (N) form of the species,

$$f^+(\mathrm{X}) = \rho_{N+1}(\mathrm{X}) - \rho_N(\mathrm{X}) \tag{S9}$$

$$\rho(\mathrm{X}) = -q(\mathrm{X}) \tag{S10}$$

where $q(\mathrm{X})$ is the partial charge at the radical center X, calculated with natural population analysis.[20] Finally, the local electrophilicity index ω^+ for RO_2 reactants and H-shift products is calculated as,[11]

$$\omega^+ = \omega f^+(\mathrm{X}) \tag{S11}$$

and the corresponding site-specific difference in this index is calculated as:

$$\Delta\omega^+ = \omega^+(\text{product}) - \omega^+(\text{reactant}) \tag{S12}$$

An analogous measure $\Delta\omega^k$,[12] using the natural spin density $\rho_s(\mathrm{X})$ at the radical center X instead of the Fukui function $f^+(\mathrm{X})$ as a local descriptor,[21] was also calculated:

$$\omega^k = \omega\rho_s(\mathrm{X}) \tag{S13}$$

$$\Delta\omega^k = \omega^k(\text{product}) - \omega^k(\text{reactant}) \tag{S14}$$

The observed trends in $\Delta\omega^+$ and $\Delta\omega^k$ were very similar. The results from these calculations are shown in Figure S8 and Table S10.

Table S10: Vertical ionization potential (I), vertical electron affinity (A), global electrophilicity index (ω), Fukui function for nucleophilic attack $f^+(\mathrm{X})$ condensed onto the radical center X, spin density ($\rho_s(\mathrm{X})$) at the radical X, Fukui function-based local electrophilicity index (ω^+), Spin density-based local electrophilicity index (ω^k), and site-specific differences in local electrophilicity indices $\Delta\omega^+ = \omega^+(\text{QOOH}) - \omega^+(\text{RO}_2)$ and $\Delta\omega^k = \omega^k(\text{QOOH}) - \omega^k(\text{RO}_2)$, calculated at the ωB97X-D/aug-cc-pVTZ level of theory and using natural population analysis, for OCT 2-RO_2, DEE 2-RO_2, EP 2-RO_2, EP 7-RO_2, and their respective 1, n H-shift products (1, n QOOH).

System	Species	I [eV]	A [eV]	ω [eV]	$f^+(\mathrm{X})$	$\rho_s(\mathrm{X})$	ω^+ [eV]	ω^k [eV]	$\Delta\omega^+$ [eV]	$\Delta\omega^k$ [eV]
DEE 2-RO_2	RO_2	10.24	0.35	1.42	0.58	0.69	0.82	0.98	—	—
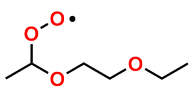	1,5 QOOH	7.58	-0.19	0.88	0.54	0.84	0.47	0.73	-0.34	-0.24
	1,6 QOOH	7.54	-0.12	0.90	0.63	0.86	0.57	0.77	-0.25	-0.21
	1,8 QOOH	7.11	-0.69	0.66	0.48	0.85	0.32	0.56	-0.50	-0.41
EP 2-RO_2	RO_2	10.32	0.54	1.51	0.59	0.70	0.88	1.06	—	—
	1,5 QOOH	7.13	-0.41	0.75	0.56	0.84	0.42	0.63	-0.47	-0.43
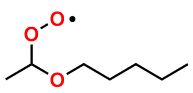	1,6 QOOH	7.58	-0.29	0.84	0.63	0.94	0.53	0.80	-0.35	-0.26
	1,7 QOOH	7.32	-0.53	0.73	0.56	0.95	0.41	0.69	-0.48	-0.36
	1,8 QOOH	7.37	-0.67	0.70	0.58	0.95	0.40	0.66	-0.48	-0.40

System	Species	I [eV]	A [eV]	ω [eV]	$f^+(\mathrm{X})$	$\rho_s(\mathrm{X})$	ω^+ [eV]	ω^k [eV]	$\Delta\omega^+$ [eV]	$\Delta\omega^k$ [eV]
EP 7-RO_2	RO_2	10.33	0.42	1.46	0.57	0.69	0.84	1.01	—	—
	1,4 QOOH	7.86	0.08	1.01	0.61	0.94	0.62	0.96	-0.22	-0.05
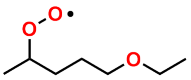	1,5 QOOH	7.54	-0.37	0.81	0.59	0.95	0.48	0.77	-0.36	-0.24
	1,6 QOOH	6.76	-0.73	0.61	0.47	0.85	0.28	0.52	-0.55	-0.49
	1,8 QOOH	6.86	-0.86	0.58	0.45	0.85	0.26	0.49	-0.58	-0.52
OCT 7-RO_2	RO_2	10.31	0.44	1.46	0.57	0.69	0.84	1.01	—	—
	1,4 QOOH	7.91	0.13	1.04	0.63	0.94	0.65	0.97	-0.19	-0.04
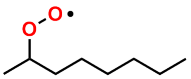	1,5 QOOH	7.30	-0.52	0.73	0.59	0.95	0.43	0.70	-0.41	-0.32
	1,6 QOOH	7.25	-0.54	0.72	0.60	0.95	0.43	0.68	-0.41	-0.33
	1,7 QOOH	7.28	-0.59	0.71	0.60	0.95	0.43	0.67	-0.41	-0.34
	1,8 QOOH	7.38	-0.66	0.70	0.58	0.95	0.41	0.66	-0.43	-0.35

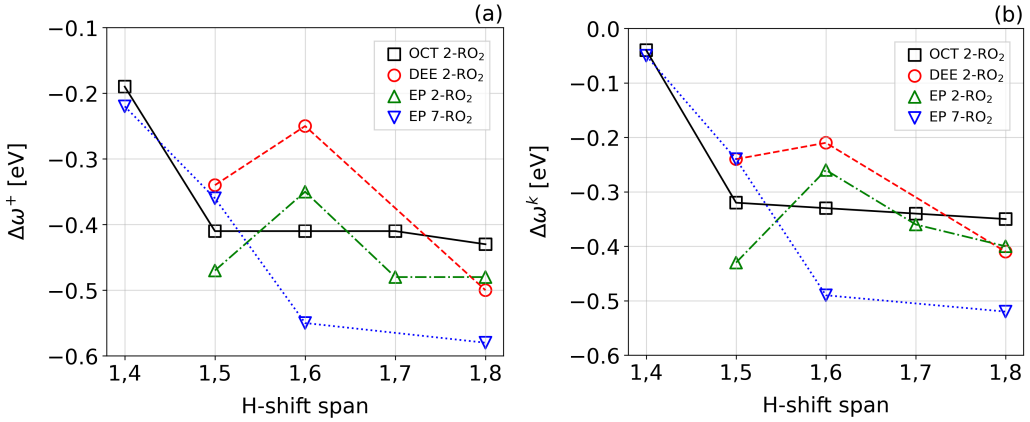

Figure S8: **(a)** Site-specific differences in condensed Fukui function-based local electrophilicity indices $\Delta\omega^+ = \omega^+(\mathrm{QOOH}) - \omega^+(\mathrm{RO_2})$ and in **(b)** Spin density-based local electrophilicity indices $\Delta\omega^k = \omega^k(\mathrm{QOOH}) - \omega^k(\mathrm{RO_2})$, calculated with natural population analysis at the ωB97X-D/aug-cc-pVTZ level of theory, for H-shift reactions available to OCT 2-RO_2, DEE 2-RO_2, EP 2-RO_2, and EP 7-RO_2.

5.5 Non-covalent Interaction Analysis

The impact of steric effects on H-shift selectivity was probed with non-covalent interaction (NCI) analysis,[22,23] using the Multiwfn v3.8 software.[24,25] The reduced density gradient (RDG) $s(\rho)$ is an unitless quantity, calculated from the ratio between the electron density ρ and its gradient $\nabla\rho$, useful for identifying regions where non-covalent interactions take place, as well as assessing their strength.

$$s(\rho) = \frac{1}{2\left(3\pi^2\right)^{1/3}} \frac{|\nabla\rho|}{\rho^{4/3}} \tag{S15}$$

Close to critical points, such as bond critical points or ring critical points as defined by the theory of atoms in molecules,[26] the density gradient $\nabla\rho$ approaches zero (and

therefore so does the reduced gradient). Regions in space associated with weaker, non-covalent interactions, however, display small electron densities ρ in addition to small $s(\rho)$. Moreover, the second-order derivative of the electron density ($\nabla^2\rho$) can be used to characterize the nature of these interactions. More specifically, the sign of the second-largest eigenvalue of $\nabla^2\rho$ (λ_2) at a given point indicates if the interaction is attractive or repulsive. While the largest eigenvalue λ_3 is associated with the internuclear axis (between e.g. two interacting fragments) and is positive for all weak interactions, λ_2 is associated with the plane orthogonal to the internuclear axis and is negative for attractive interactions, such as H-bonds or van der Waals interactions, and positive for repulsive interactions, such as steric clashes.

Plots of $s(\rho)$ versus $\text{sign}(\lambda_2)\rho$ calculated for OCT 2-RO_2, DEE 2-RO_2, EP 2-RO_2, EP 7-RO_2, and their respective H-shift transition states, at the ωB97X-D/aug-cc-pVTZ level of theory and using a high quality grid, are shown in Figures S9-S28. Visual interpretation of RDG plots is mostly qualitative: troughs dipping below $s(\rho)$ ~0.5 represent NCI interactions. Larger, deeper troughs, towards more positive/negative values of $\text{sign}(\lambda_2)\rho$ are associated with stronger repulsive/attractive interactions. For all systems, the decrease in transition state (angle) ring-strain with increasing H-shift span (from 1,4 to 1,6) is clearly seen from a shift in repulsive NCI troughs towards less positive values of $\text{sign}(\lambda_2)\rho$. Less obvious, but still apparent, is an increase in the size of attractive and repulsive NCI troughs for longer-span H-shift transition states (compared to a 1,6 span TS), consistent with the appearance of transannular interactions. That being said, analysis of relative steric strain by comparing RDG plots for 1,8 H-shift transition states across different RO_2 is challenging with this qualitative view.

A quantitative NCI analysis, based on an index calculated from electron desity integrals over NCI regions,[23] was also used here:

$$q_{\text{bind}} = q_{\text{rep}} - q_{\text{att}} \tag{S16}$$

$$q_{\text{rep}} = \int_{\Omega_{\text{NCI}}} \rho^{4/3}(\mathbf{r})\mathrm{d}\mathbf{r} \qquad \lambda_2(\mathbf{r}) > 0 \tag{S17}$$

$$q_{\text{att}} = \int_{\Omega_{\text{NCI}}} \rho^{4/3}(\mathbf{r})\mathrm{d}\mathbf{r} \qquad \lambda_2(\mathbf{r}) < 0 \tag{S18}$$

where the q_{rep} and q_{att} indices describe repulsive and attractive contributions, respectively, to the overall NCI interaction index q_{bind}. This index has been shown to closely reflect the potential energy curves of H-bonded complexes as the interacting fragments move relative to each other.[23] A density exponential value of 4/3, a grid size of 0.1 bohr, and a cutoff $s(\rho)$ value of 0.6 for defining NCI domains were used in the calculations. Calculated NCI domain isosurfaces, volumes and q_{bind} indices are shown in Figures S9-S28 and Tables S12-S31. A summary of calculated NCI

indices is also shown in Table S11.

Table S11: Non-covalent interaction (NCI) indices based on electron density integrals over all domains (Tables S12-S31 and Figures S9-S28) contained within a reduced density gradient $s(\rho) < 0.6$ isosurface for attractive (q_{att}), repulsive (q_{rep}), and overall ($q_{\text{bind}} = q_{\text{rep}} - q_{\text{att}}$) interactions. Calculated were done at the ωB97X-D/aug-cc-pVTZ level of theory with a grid spacing of 0.1 bohr and an electron density exponent of 4/3, for OCT 2-RO_2, DEE 2-RO_2, EP 2-RO_2, EP 7-RO_2, and their respective 1,n H-shift transition states. Activation NCI indices calculated as $\Delta^{\ddagger}q = q(\text{TS}) - q(RO_2)$.

System	Species	q_{att} [a.u.]	q_{rep} [a.u.]	q_{bind} [a.u.]	$\Delta^{\ddagger}q_{\text{att}}$ [a.u.]	$\Delta^{\ddagger}q_{\text{rep}}$ [a.u.]	$\Delta^{\ddagger}q_{\text{bind}}$ [a.u.]
DEE 2-RO_2	RO_2	0.0008	0.0016	0.0008	—	—	—
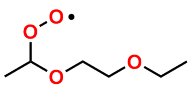	1,5 H-shift TS	0.0000	0.0064	0.0064	-0.0008	0.0048	0.0056
	1,6 H-shift TS	0.0000	0.0028	0.0028	-0.0008	0.0012	0.0020
	1,8 H-shift TS	0.0011	0.0059	0.0048	0.0003	0.0043	0.0040
EP 2-RO_2	RO_2	0.0008	0.0025	0.0017	—	—	—
	1,5 H-shift TS	0.0011	0.0086	0.0075	0.0004	0.0062	0.0058
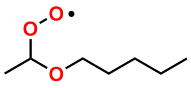	1,6 H-shift TS	0.0004	0.0040	0.0036	-0.0004	0.0015	0.0019
	1,7 H-shift TS	0.0019	0.0077	0.0058	0.0011	0.0052	0.0041
	1,8 H-shift TS	0.0017	0.0062	0.0045	0.0009	0.0037	0.0028
EP 7-RO_2	RO_2	0.0005	0.0014	0.0009	—	—	—
	1,4 H-shift TS	0.0013	0.0098	0.0084	0.0008	0.0084	0.0076
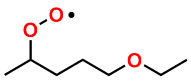	1,5 H-shift TS	0.0019	0.0102	0.0083	0.0013	0.0088	0.0074
	1,6 H-shift TS	0.0002	0.0023	0.0021	-0.0003	0.0009	0.0012
	1,8 H-shift TS	0.0025	0.0060	0.0036	0.0019	0.0046	0.0027
OCT 7-RO_2	RO_2	0.0003	0.0009	0.0006	—	—	—
	1,4 H-shift TS	0.0000	0.0084	0.0084	-0.0003	0.0076	0.0078
	1,5 H-shift TS	0.0001	0.0064	0.0063	-0.0001	0.0056	0.0057
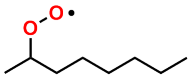	1,6 H-shift TS	0.0000	0.0016	0.0016	-0.0003	0.0008	0.0010
	1,7 H-shift TS	0.0030	0.0080	0.0050	0.0027	0.0071	0.0044
	1,8 H-shift TS	0.0035	0.0094	0.0059	0.0032	0.0085	0.0053

Table S12: NCI domain volumes and indices at $s(\rho) < 0.6$ for DEE 2-RO_2.

Domain	1	2	3	4	5	total
q_{att} [a.u.]	0.000000	0.000003	0.000799	0.000000	0.000030	0.000832
q_{rep} [a.u.]	0.000036	0.000248	0.000974	0.000044	0.000305	0.001607
q_{bind} [a.u.]	0.000036	0.000245	0.000175	0.000044	0.000274	0.000775
$V_{\lambda_2<0}$ [bohr^3]	0.000	0.002	0.425	0.000	0.023	0.450
$V_{\lambda_2>0}$ [bohr^3]	0.015	0.136	0.561	0.009	0.167	0.888

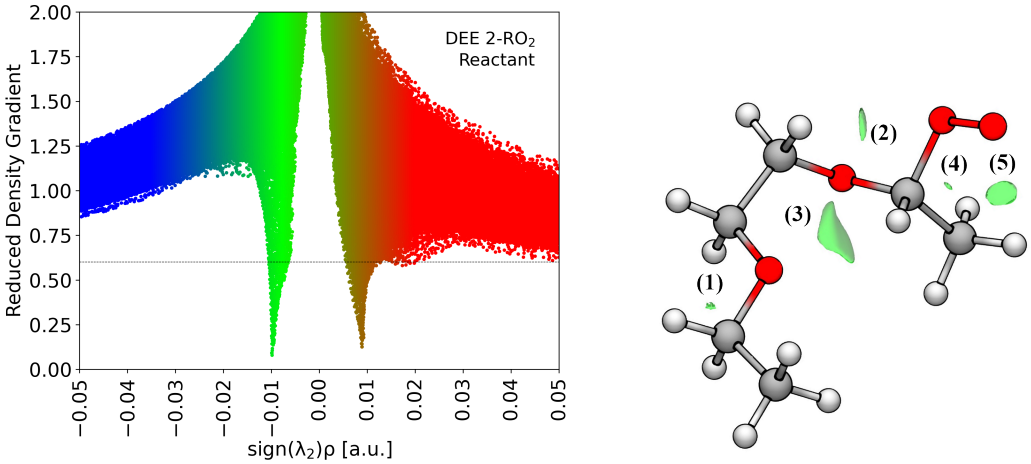

Figure S9: RDG plot (left) and NCI domains at $s(\rho) < 0.6$ for DEE 2-RO_2 (right).

Table S13: NCI domain volumes and indices at $s(\rho) < 0.6$ for DEE 2-RO_2 1,5 H-shift TS.

Domain	1	2	total
q_{att} [a.u.]	0.000000	0.000000	0.000000
q_{rep} [a.u.]	0.006246	0.000123	0.006369
q_{bind} [a.u.]	0.006246	0.000123	0.006369
$V_{\lambda_2<0}$ [bohr^3]	0.000	0.000	0.000
$V_{\lambda_2>0}$ [bohr^3]	0.874	0.007	0.881

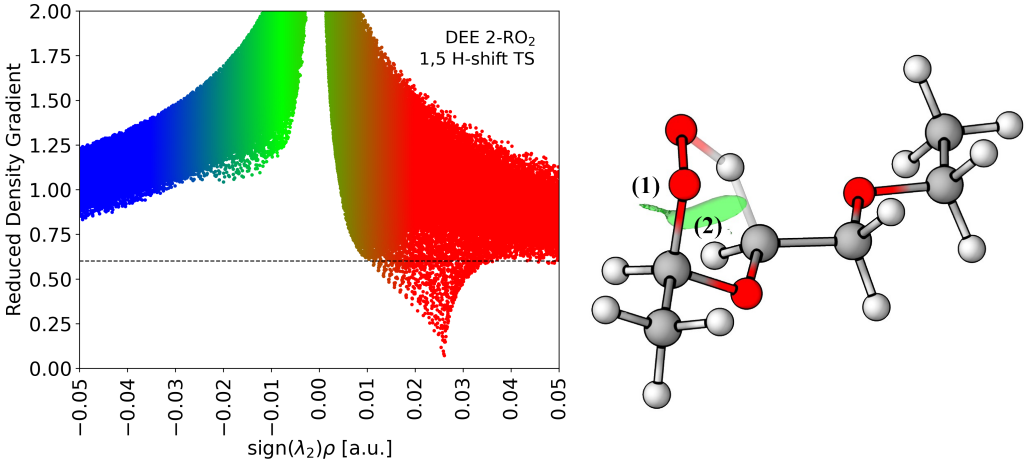

Figure S10: RDG plot (left) and NCI domains at $s(\rho) < 0.6$ for DEE 2-RO_2 1,5 H-shift TS (right).

Table S14: NCI domain volumes and indices at $s(\rho) < 0.6$ for DEE 2-RO_2 1,6 H-shift TS.

Domain	1	2	3	4	total
q_{att} [a.u.]	0.000000	0.000000	0.000000	0.000000	0.000000
q_{rep} [a.u.]	0.000313	0.000330	0.002109	0.000059	0.002811
q_{bind} [a.u.]	0.000313	0.000330	0.002109	0.000059	0.002811
$V_{\lambda_2<0}$ [bohr^3]	0.000	0.000	0.000	0.000	0.000
$V_{\lambda_2>0}$ [bohr^3]	0.113	0.064	0.774	0.023	0.974

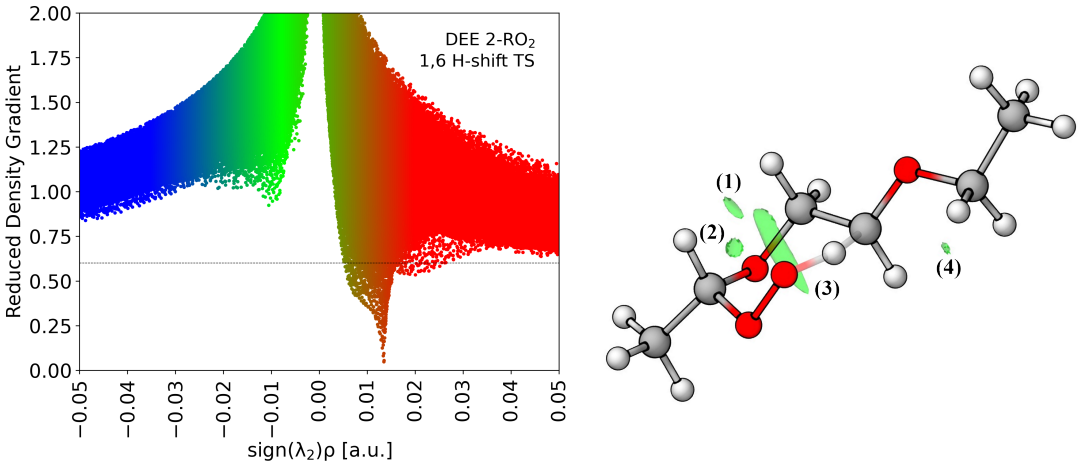

Figure S11: RDG plot (left) and NCI domains at $s(\rho) < 0.6$ for DEE 2-RO_2 1,6 H-shift TS (right).

Table S15: NCI domain volumes and indices at $s(\rho) < 0.6$ for DEE 2-RO_2 1,8 H-shift TS.

Domain	1	2	3	4	total
q_{att} [a.u.]	0.000593	0.000222	0.000289	0.000000	0.001104
q_{rep} [a.u.]	0.001302	0.001306	0.002722	0.000588	0.005918
q_{bind} [a.u.]	0.000708	0.001084	0.002434	0.000588	0.004815
$V_{\lambda_2<0}$ [bohr^3]	0.240	0.107	0.180	0.000	0.527
$V_{\lambda_2>0}$ [bohr^3]	0.370	0.425	1.714	0.186	2.695

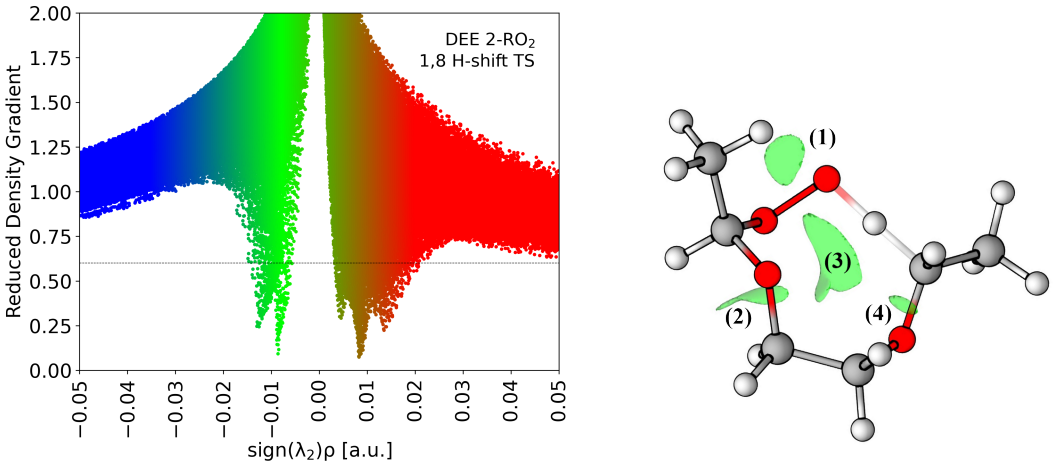

Figure S12: RDG plot (left) and NCI domains at $s(\rho) < 0.6$ for DEE 2-RO_2 1,8 H-shift TS (right).

Table S16: NCI domain volumes and indices at $s(\rho) < 0.6$ for EP 2-RO_2.

Domain	1	2	3	4	total
q_{att} [a.u.]	0.000000	0.000589	0.000000	0.000195	0.000784
q_{rep} [a.u.]	0.000713	0.000977	0.000331	0.000448	0.002469
q_{bind} [a.u.]	0.000713	0.000389	0.000331	0.000252	0.001685
$V_{\lambda_2<0}$ [bohr^3]	0.000	0.395	0.000	0.127	0.522
$V_{\lambda_2>0}$ [bohr^3]	0.129	0.622	0.115	0.215	1.081

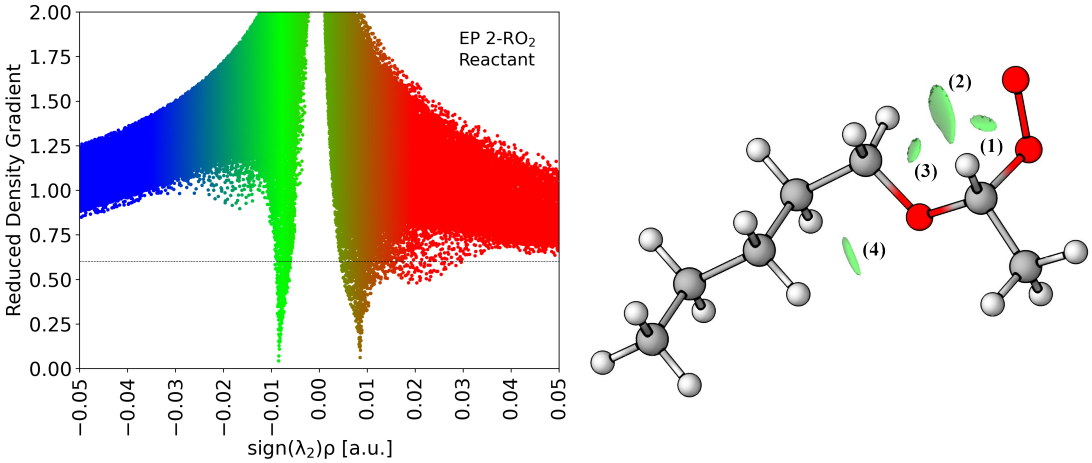

Figure S13: RDG plot (left) and NCI domains at $s(\rho) < 0.6$ for EP 2-RO_2 (right).

Table S17: NCI domain volumes and indices at $s(\rho) < 0.6$ for EP 2-RO_2 1,5 H-shift TS.

Domain	1	2	3	4	total
q_{att} [a.u.]	0.000000	0.000000	0.000925	0.000218	0.001143
q_{rep} [a.u.]	0.000106	0.006318	0.001694	0.000504	0.008622
q_{bind} [a.u.]	0.000106	0.006318	0.000769	0.000286	0.007478
$V_{\lambda_2<0}$ [bohr^3]	0.000	0.000	0.722	0.134	0.856
$V_{\lambda_2>0}$ [bohr^3]	0.006	0.893	1.301	0.224	2.424

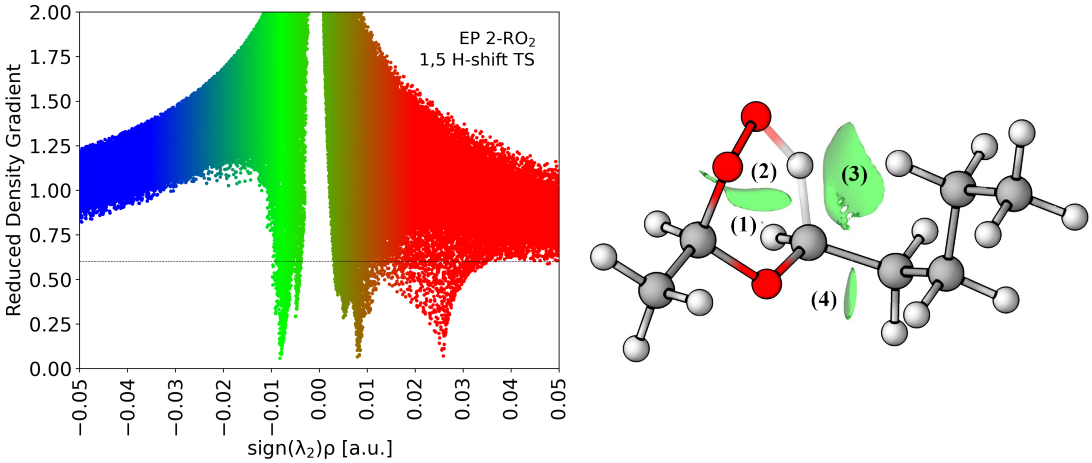

Figure S14: RDG plot (left) and NCI domains at $s(\rho) < 0.6$ for EP 2-RO_2 1,5 H-shift TS (right).

Table S18: NCI domain volumes and indices at $s(\rho) < 0.6$ for EP 2-RO_2 1,6 H-shift TS.

Domain	1	2	3	4	total
q_{att} [a.u.]	0.000000	0.000000	0.000391	0.000000	0.000391
q_{rep} [a.u.]	0.000224	0.000342	0.003427	0.000020	0.004012
q_{bind} [a.u.]	0.000224	0.000342	0.003036	0.000020	0.003621
$V_{\lambda_2<0}$ [bohr^3]	0.000	0.000	0.324	0.000	0.324
$V_{\lambda_2>0}$ [bohr^3]	0.085	0.067	1.658	0.025	1.835

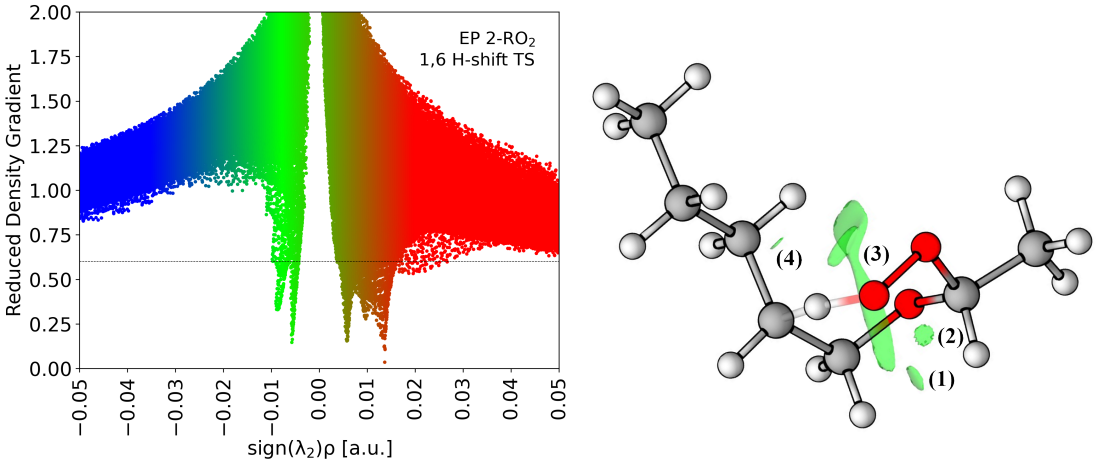

Figure S15: RDG plot (left) and NCI domains at $s(\rho) < 0.6$ for EP 2-RO_2 1,6 H-shift TS (right).

Table S19: NCI domain volumes and indices at $s(\rho) < 0.6$ for EP 2-RO_2 1,7 H-shift TS.

Domain	1	2	3	total
q_{att} [a.u.]	0.000000	0.000342	0.001529	0.001870
q_{rep} [a.u.]	0.000035	0.000808	0.006816	0.007659
q_{bind} [a.u.]	0.000035	0.000466	0.005287	0.005788
$V_{\lambda_2<0}$ [bohr^3]	0.000	0.168	0.571	0.739
$V_{\lambda_2>0}$ [bohr^3]	0.015	0.287	2.509	2.811

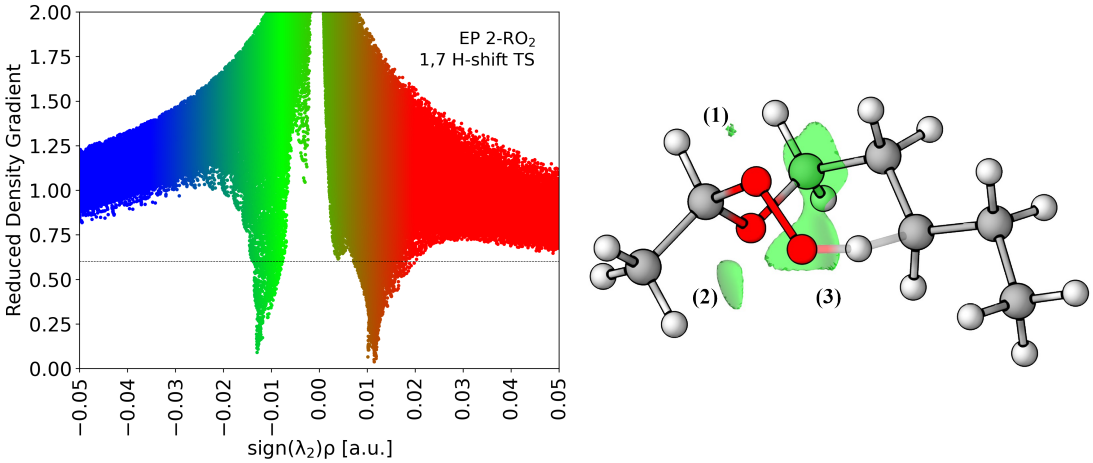

Figure S16: RDG plot (left) and NCI domains at $s(\rho) < 0.6$ for EP 2-RO_2 1,7 H-shift TS (right).

Table S20: NCI domain volumes and indices at $s(\rho) < 0.6$ for EP 2-RO_2 1,8 H-shift TS.

Domain	1	2	total
q_{att} [a.u.]	0.000000	0.001665	0.001665
q_{rep} [a.u.]	0.000324	0.005854	0.006178
q_{bind} [a.u.]	0.000324	0.004189	0.004513
$V_{\lambda_2<0}$ [bohr^3]	0.000	0.918	0.918
$V_{\lambda_2>0}$ [bohr^3]	0.065	3.423	3.488

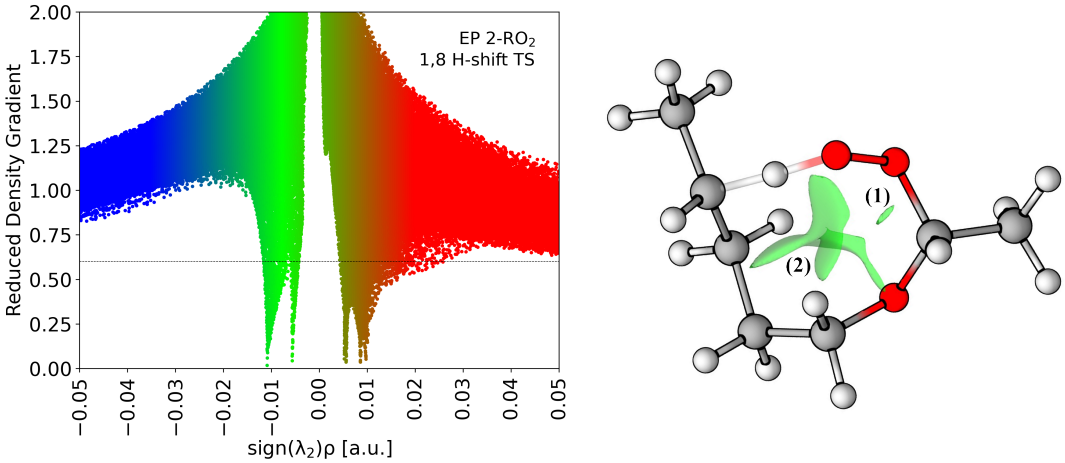

Figure S17: RDG plot (left) and NCI domains at $s(\rho) < 0.6$ for EP 2-RO_2 1,8 H-shift TS (right).

Table S21: NCI domain volumes and indices at $s(\rho) < 0.6$ for EP 7-RO_2.

Domain	1	2	3	4	total
q_{att} [a.u.]	0.000000	0.000136	0.000267	0.000105	0.000509
q_{rep} [a.u.]	0.000031	0.000388	0.000543	0.000441	0.001403
q_{bind} [a.u.]	0.000031	0.000251	0.000276	0.000335	0.000893
$V_{\lambda_2<0}$ [bohr^3]	0.000	0.091	0.159	0.067	0.317
$V_{\lambda_2>0}$ [bohr^3]	0.013	0.190	0.238	0.202	0.643

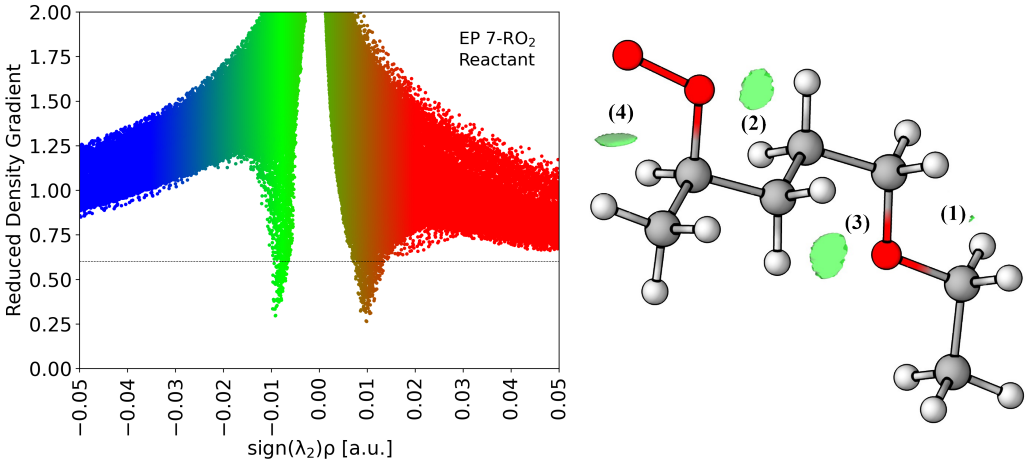

Figure S18: RDG plot (left) and NCI domains at $s(\rho) < 0.6$ for EP 7-RO_2 (right).

Table S22: NCI domain volumes and indices at $s(\rho) < 0.6$ for EP 7-RO_2 1,4 H-shift TS.

Domain	1	2	3	4	total
q_{att} [a.u.]	0.000000	0.001276	0.000055	0.000000	0.001330
q_{rep} [a.u.]	0.000035	0.001358	0.000076	0.008311	0.009780
q_{bind} [a.u.]	0.000035	0.000082	0.000021	0.008311	0.008449
$V_{\lambda_2<0}$ [bohr^3]	0.000	0.793	0.130	0.000	0.923
$V_{\lambda_2>0}$ [bohr^3]	0.015	1.116	0.156	0.576	1.863

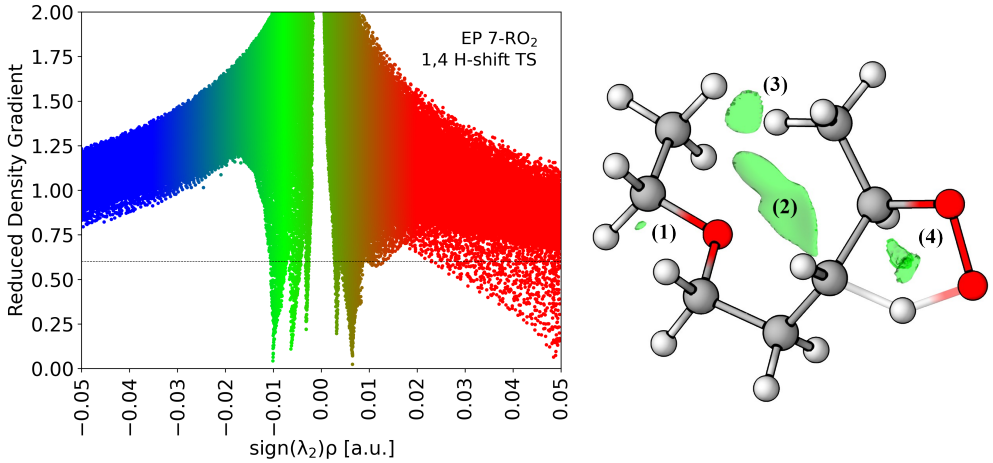

Figure S19: RDG plot (left) and NCI domains at $s(\rho) < 0.6$ for EP 7-RO_2 1,4 H-shift TS (right).

Table S23: NCI domain volumes and indices at $s(\rho) < 0.6$ for EP 7-RO_2 1,5 H-shift TS.

Domain	1	2	3	4	5	total
q_{att} [a.u.]	0.000000	0.000779	0.000000	0.000000	0.001073	0.001852
q_{rep} [a.u.]	0.000123	0.001091	0.006069	0.000048	0.002855	0.010186
q_{bind} [a.u.]	0.000123	0.000311	0.006069	0.000048	0.001782	0.008334
$V_{\lambda_2<0}$ [bohr^3]	0.000	0.316	0.000	0.000	0.755	1.071
$V_{\lambda_2>0}$ [bohr^3]	0.048	0.346	0.839	0.010	2.080	3.323

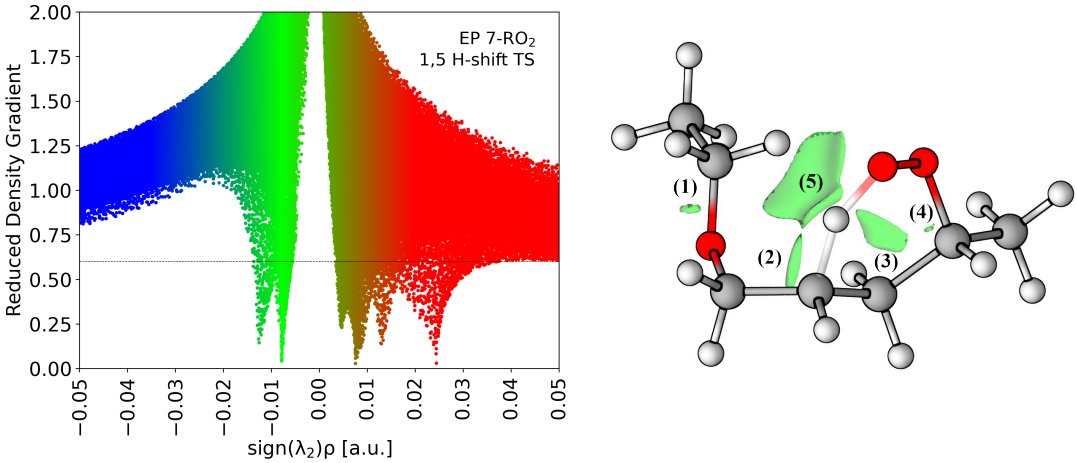

Figure S20: RDG plot (left) and NCI domains at $s(\rho) < 0.6$ for EP 7-RO_2 1,5 H-shift TS (right).

Table S24: NCI domain volumes and indices at $s(\rho) < 0.6$ for EP 7-RO_2 1,6 H-shift TS.

Domain	1	2	3	4	5	total
q_{att} [a.u.]	0.000000	0.000000	0.000166	0.000000	0.000000	0.000166
q_{rep} [a.u.]	0.000039	0.000036	0.000410	0.001617	0.000195	0.002297
q_{bind} [a.u.]	0.000039	0.000036	0.000244	0.001617	0.000195	0.002131
$V_{\lambda_2<0}$ [bohr^3]	0.000	0.000	0.111	0.000	0.000	0.111
$V_{\lambda_2>0}$ [bohr^3]	0.016	0.039	0.201	0.761	0.041	1.058

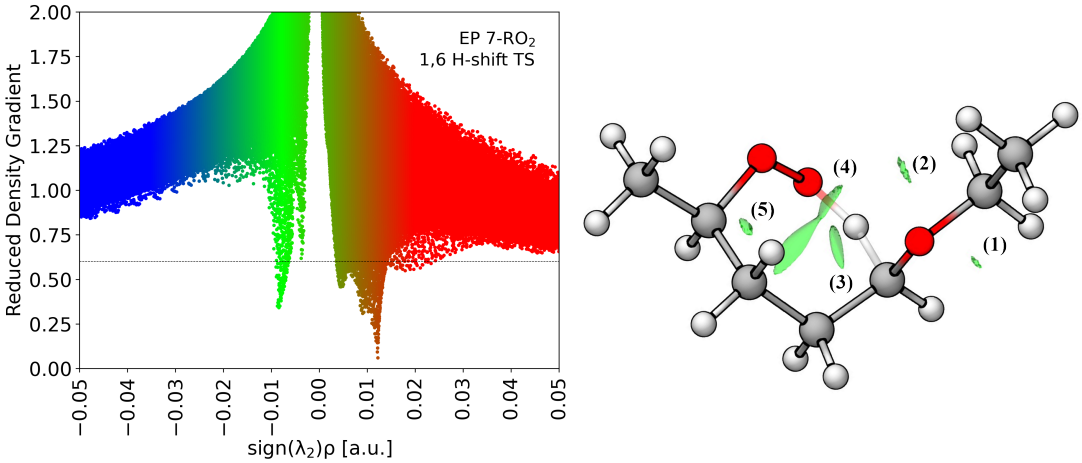

Figure S21: RDG plot (left) and NCI domains at $s(\rho) < 0.6$ for EP 7-RO_2 1,6 H-shift TS (right).

Table S25: NCI domain volumes and indices at $s(\rho) < 0.6$ for EP 7-RO_2 1,8 H-shift TS.

Domain	1	2	3	4	total
q_{att} [a.u.]	0.000000	0.000000	0.000635	0.001819	0.002453
q_{rep} [a.u.]	0.000704	0.000050	0.000730	0.004549	0.006034
q_{bind} [a.u.]	0.000704	0.000050	0.000095	0.002730	0.003580
$V_{\lambda_2<0}$ [bohr^3]	0.000	0.000	0.397	0.923	1.320
$V_{\lambda_2>0}$ [bohr^3]	0.194	0.105	0.375	2.716	3.390

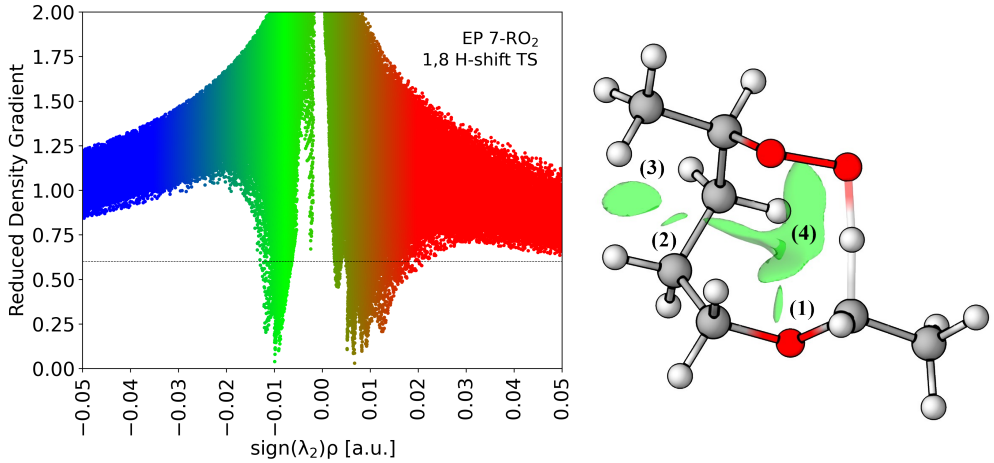

Figure S22: RDG plot (left) and NCI domains at $s(\rho) < 0.6$ for EP 7-RO_2 1,8 H-shift TS (right).

Table S26: NCI domain volumes and indices at $s(\rho) < 0.6$ for OCT 2-RO_2.

Domain	1	2	total
q_{att} [a.u.]	0.000147	0.000108	0.000254
q_{rep} [a.u.]	0.000392	0.000462	0.000854
q_{bind} [a.u.]	0.000245	0.000354	0.000600
$V_{\lambda_2<0}$ [bohr^3]	0.097	0.068	0.165
$V_{\lambda_2>0}$ [bohr^3]	0.192	0.211	0.403

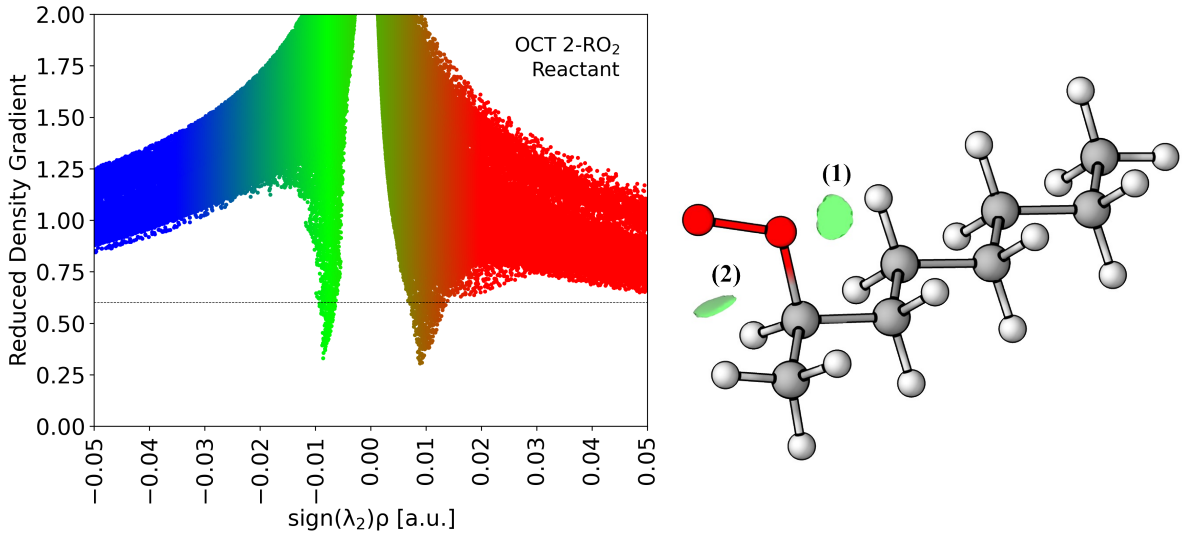

Figure S23: RDG plot (left) and NCI domains at $s(\rho) < 0.6$ for OCT 2-RO_2 (right).

Table S27: NCI domain volumes and indices at $s(\rho) < 0.6$ for OCT 2-RO_2 1,4 H-shift TS.

Domain	1	total
q_{att} [a.u.]	0.000000	0.000000
q_{rep} [a.u.]	0.008434	0.008434
q_{bind} [a.u.]	0.008434	0.008434
$V_{\lambda_2<0}$ [bohr^3]	0.000	0.000
$V_{\lambda_2>0}$ [bohr^3]	0.584	0.584

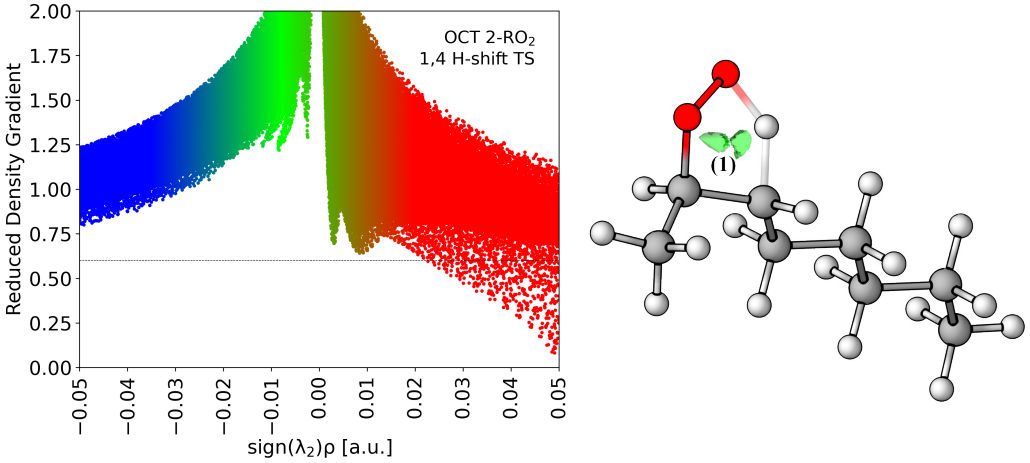

Figure S24: RDG plot (left) and NCI domains at $s(\rho) < 0.6$ for OCT 2-RO_2 1,4 H-shift TS (right).

Table S28: NCI domain volumes and indices at $s(\rho) < 0.6$ for OCT 2-RO_2 1,5 H-shift TS.

Domain	1	2	3	total
q_{att} [a.u.]	0.000129	0.000000	0.000000	0.000129
q_{rep} [a.u.]	0.000273	0.000035	0.006141	0.006449
q_{bind} [a.u.]	0.000144	0.000035	0.006141	0.006320
$V_{\lambda_2<0}$ [bohr^3]	0.146	0.000	0.000	0.146
$V_{\lambda_2>0}$ [bohr^3]	0.264	0.007	0.839	1.110

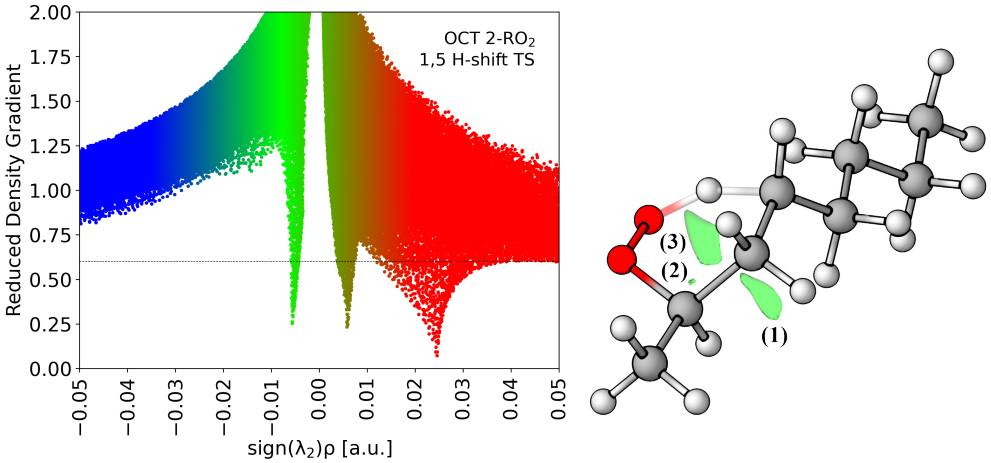

Figure S25: RDG plot (left) and NCI domains at $s(\rho) < 0.6$ for OCT 2-RO_2 1,5 H-shift TS (right).

Table S29: NCI domain volumes and indices at $s(\rho) < 0.6$ for OCT 2-RO_2 1,6 H-shift TS.

Domain	1	2	total
q_{att} [a.u.]	0.000000	0.000000	0.000000
q_{rep} [a.u.]	0.000108	0.001504	0.001612
q_{bind} [a.u.]	0.000108	0.001504	0.001612
$V_{\lambda_2<0}$ [bohr^3]	0.000	0.000	0.000
$V_{\lambda_2>0}$ [bohr^3]	0.023	0.581	0.604

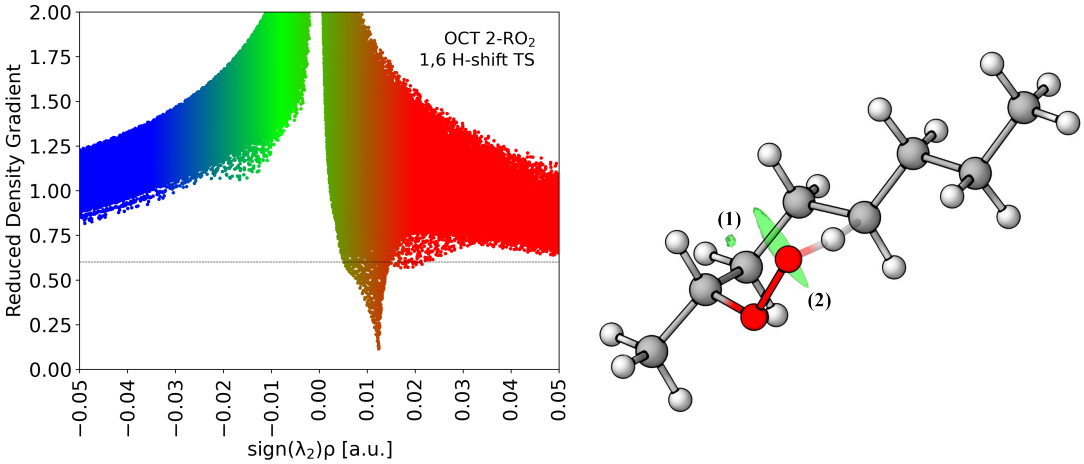

Figure S26: RDG plot (left) and NCI domains at $s(\rho) < 0.6$ for OCT 2-RO_2 1,6 H-shift TS (right).

Table S30: NCI domain volumes and indices at $s(\rho) < 0.6$ for OCT 2-RO_2 1,7 H-shift TS.

Domain	1	2	3	4	total
q_{att} [a.u.]	0.000012	0.000437	0.000000	0.002508	0.002958
q_{rep} [a.u.]	0.000172	0.000547	0.000037	0.007223	0.007979
q_{bind} [a.u.]	0.000160	0.000111	0.000037	0.004715	0.005022
$V_{\lambda_2<0}$ [bohr^3]	0.027	0.314	0.000	1.029	1.370
$V_{\lambda_2>0}$ [bohr^3]	0.275	0.321	0.053	2.995	3.644

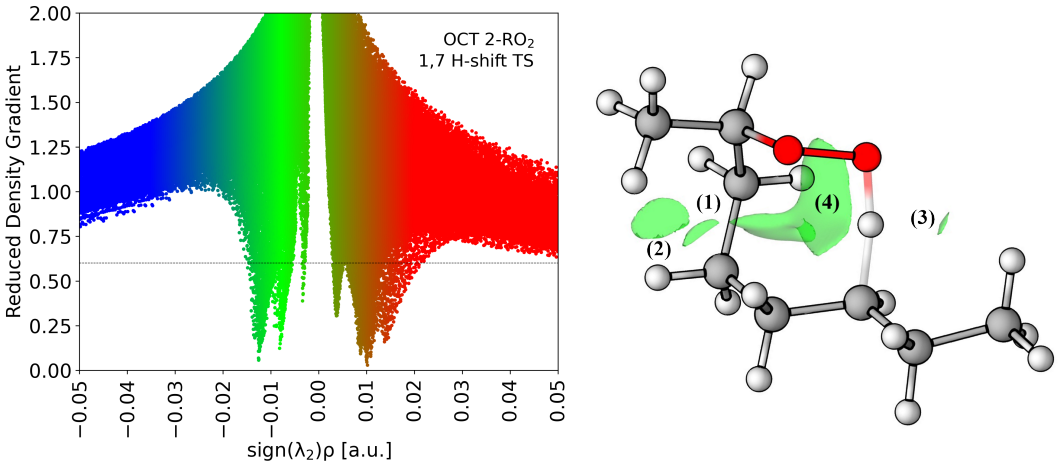

Figure S27: RDG plot (left) and NCI domains at $s(\rho) < 0.6$ for OCT 2-RO_2 1,7 H-shift TS (right).

Table S31: NCI domain volumes and indices at $s(\rho) < 0.6$ for OCT 2-RO_2 1,8 H-shift TS.

Domain	1	2	total
q_{att} [a.u.]	0.000180	0.003291	0.003471
q_{rep} [a.u.]	0.000572	0.008832	0.009404
q_{bind} [a.u.]	0.000392	0.005541	0.005933
$V_{\lambda_2<0}$ [bohr^3]	0.109	1.452	1.561
$V_{\lambda_2>0}$ [bohr^3]	0.251	4.196	4.447

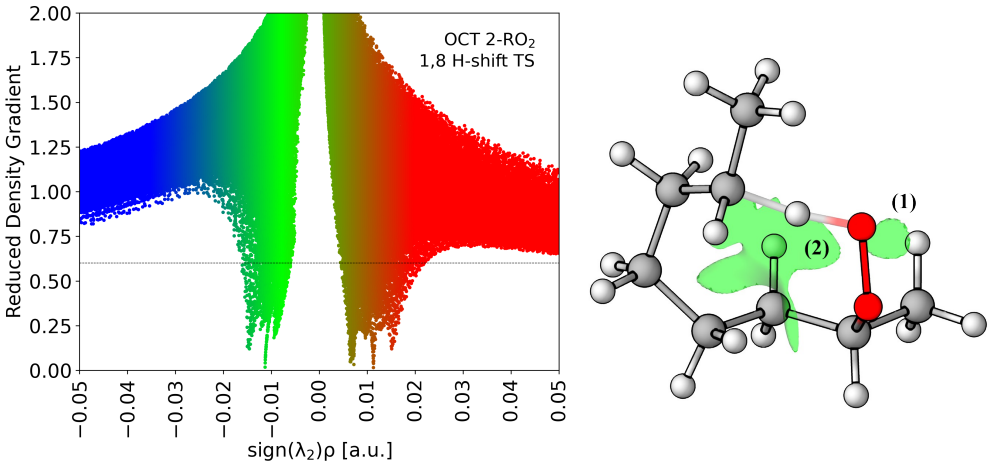

Figure S28: RDG plot (left) and NCI domains at $s(\rho) < 0.6$ for OCT 2-RO_2 1,8 H-shift TS (right).

5.6 Natural Steric Analysis

Natural steric analysis[27,28] was also used to assess the impact of steric effects on H-shift selectivity. The quantity selected for this analysis was the total steric exchange energy, calculated from the energy difference between natural localized molecular orbitals (NLMO) and their respective pre-orthogonalization (PNLMO) counterparts. Results from these calculations are shown in Table S32.

Table S32: Total natural localized molecular orbital (NLMO) steric energy from natural steric analysis for α and β NLMOs ($E_{\text{steric}}(\alpha)$ and $E_{\text{steric}}(\beta)$), and spin-averaged value (E_{steric}), calculated at the ωB97X-D/aug-cc-pVTZ level of theory, for OCT 2-RO_2, DEE 2-RO_2, EP 2-RO_2, EP 7-RO_2, and their respective $1,n$ H-shift transition states. Activation steric energy calculated as $\Delta^{\ddagger}E_{\text{steric}} = E_{\text{steric}}(\text{TS}) - E_{\text{steric}}(RO_2)$.

System	Species	$E_{\text{steric}}(\alpha)$ [kcal mol^{-1}]	$E_{\text{steric}}(\beta)$ [kcal mol^{-1}]	E_{steric} [kcal mol^{-1}]	$\Delta^{\ddagger}E_{\text{steric}}$ [kcal mol^{-1}]
DEE 2-RO_2	RO_2	185	177	362	—
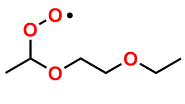	1,5 H-shift TS	226	198	424	62.2
	1,6 H-shift TS	220	193	412	50.0
	1,8 H-shift TS	228	199	427	65.1
EP 2-RO_2	RO_2	203	194	397	—
	1,5 H-shift TS	253	225	477	80.5
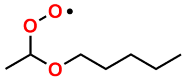	1,6 H-shift TS	248	215	463	65.8
	1,7 H-shift TS	252	215	467	69.6
	1,8 H-shift TS	249	214	464	66.7
EP 7-RO_2	RO_2	202	194	396	—
	1,4 H-shift TS	254	219	473	76.7
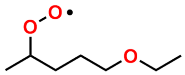	1,5 H-shift TS	255	215	470	74.1
	1,6 H-shift TS	241	211	452	56.2
	1,8 H-shift TS	245	217	462	65.8
OCT 7-RO_2	RO_2	221	212	433	—
	1,4 H-shift TS	270	236	507	73.7
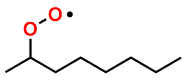	1,5 H-shift TS	272	234	505	72.1
	1,6 H-shift TS	262	228	490	56.7
	1,7 H-shift TS	269	233	501	68.1
	1,8 H-shift TS	278	244	522	89

5.7 Generalized Anomeric Effects

As discussed in the mainuscript, some effect is working to counteract the inductive C−H deactivation by β-oxyl substitution in 1,6 H-shift reactions. The reaction energy barrier of this pathway is slightly higher for EP 2-RO_2 and EP 7-RO_2, compared to OCT 2-RO_2 and DEE 2-RO_2 respectively. We hypothesize that this counteracting effect is due to the fact that the β-oxyl group is endocyclic in the ring-like transition state, providing it with some degree of stabilization that an analogous exocyclic group would not. Differences in transannular strain, invoked to explain the energy barrier trends in 1,8 H-shifts, cannot account for this relative stabilization because this type of interactions should be minimal in 1,6 H-shift transition states. This is in agreement with the natural steric analysis and NCI analysis calculations done here. Furthermore, while we show that smaller transannular strain is part of the explanation why DEE 2-RO_2 is selective towards the 1,8 H-shift pathway in comparison to OCT 2-RO_2, it cannot fully explain why the 1,8 H-shift energy barrier is lower for DEE 2-RO_2 than it is for EP 7-RO_2 (see Tables S11 and S32).

We speculate on possible explanations for these inconsistencies. The effect is apparently related to the replacement of a β-peroxyl methylene group by an oxygen atom. In the same way that a σ-withdrawing group can make abstraction sites in β-positions less nucleophilic, it can also make a β-peroxyl group more electrophilic, and therefore a better H atom acceptor. Consequently, RO_2 with electronegative heteroatoms at β-peroxyl positions (DEE 2-RO_2 and EP 2-RO_2) become more reactive towards intramolecular H-shifts *overall*. However, this hypothesis is not supported by the calculated local electrophilicity indices (Table S10). While ω^+ is larger for EP 2-RO_2 than it is for EP 7-RO_2 and OCT 2-RO_2, it has the smallest value for DEE 2-RO_2 among RO_2 reactants. Another effect that could possibly be affecting the reaction barrier heights is hyperconjugation between a lone-pair on the ether oxygen and the σ^*_{CO} orbital on the alkylperoxyl group, analogous to what happens in the generalized anomeric effect.[29]

The generalized anomeric effect is a well-known factor controlling the reaction thermodynamics and kinetics of compounds such as acetals, often rationalized in terms of hyperconjugative interactions between the p-type lone-pair orbital (n_O) on an oxygen atom and the σ^*_{CO} orbital on a vicinal C−O bond.[30–32] We argue that this type of interaction acts to enhance H-shift reaction rates in α-oxyl peroxyl radicals, such as DEE 2-RO_2 and EP 2-RO_2, which we shall discuss from the perspective of spin-orbitals occupied by β-spin electrons, as shown in Scheme X. In the reactant, the vacant p-type spin-orbital on the peroxyl group's terminal O atom interacts with a filled spin-orbital on the adjacent O atom, resulting in a bonding π_{OO} spin-orbital. At the H-shift transition state, a three-center σ bonding spin-orbital (σ_{3c}) is formed, such that the π_{OO} spin-orbital is replaced by a non-bonding n_O spin-orbital. Given a

proper alignment between functional groups, both π_{OO} and n_O orbitals can interact via hyperconjugation with the σ^*_{CO} orbital on the vicinal C−O bond. However, since non-bonding orbitals are, in general, better electron donors than bonding orbitals, a $n_O \rightarrow \sigma^*_{CO}$ interaction is stronger than a $\pi_{OO} \rightarrow \sigma^*_{CO}$ interaction and the anomeric effect stabilizes the transition state to a greater extent than it does the reactant, lowering the reaction energy barrier. An analogous enhancement in hyperconjugation can also assist H-shift reactions in hydrocarbon-derived RO_2, but to a much lesser extent, because σ^*_{CC} orbitals are poor electron acceptors. Due to electronegativity differences, the (bonding) σ_{CO} orbital is polarized towards the O atom, while the (anti-bonding) σ^*_{CO} is polarized towards the C atom. As a consequence, the overlap between donor and acceptor orbitals is larger for $n_O \rightarrow \sigma^*_{CO}$ than it is for $n_O \rightarrow \sigma^*_{CC}$.

Our hypothesis is supported by second-order perturbation theory analysis of NBO donor-acceptor interactions. For β-spin electrons, the calculated change in the $\pi_{OO}/n_O \rightarrow \sigma^*_{CX}$ (X = O, C) interaction energy ($E_{(2)}$) between the 1,6 H-shift transition state and the RO_2 reactant, for instance, is 7.3 and 4.1 kcal/mol for DEE 2-RO_2 and EP 2-RO_2 respectively (X = O), while it is 3.3 and 2.6 kcal/mol for EP 7-RO_2 and OCT 2-RO_2 respectively (X = C). The greater change observed for DEE 2-RO_2 is associated with the fact that the peroxyl group in the reactant is aligned at (almost) an antiperiplanar conformation relative to the C−O bond, optimizing the $\pi_{OO} \rightarrow \sigma^*_{CC}$ interaction instead. Comparison of interaction energies calculated for α-spin-orbitals reveals that, also for them, $n_O \rightarrow \sigma^*_{CX}$ hyperconjugation is enhanced at the transition state. Perhaps this is due to an increase in the energy of the donor orbital once the β electron density increases in the same space. A more rigorous analysis of this effect, considering the total change in $E_{(2)}$ for the interaction of the donor orbital with the antibonding orbital on the vicinal C−H and C−CH_3 bonds ($\pi_{OO}/n_O \rightarrow \sigma^*_{CC}$ and $\pi_{OO}/n_O \rightarrow \sigma^*_{CH}$) as well, for both α and β electrons, indicate a more pronounced difference in TS stabilization. The total change in $\pi_{OO}/n_O \rightarrow \sigma^*_{CX}$ interaction energy between the 1,6 H-shift transition state and the RO_2 reactant is 14.0 and 9.2 kcal/mol for DEE 2-RO_2 and EP 2-RO_2 respectively (X = O, C, and H), while it is 5.9 and 6.1 kcal/mol for EP 7-RO_2 and OCT 2-RO_2 respectively (X = C, C, and H).

5.8 Intramolecular H-bond in 2-OO-5-ROOH radical

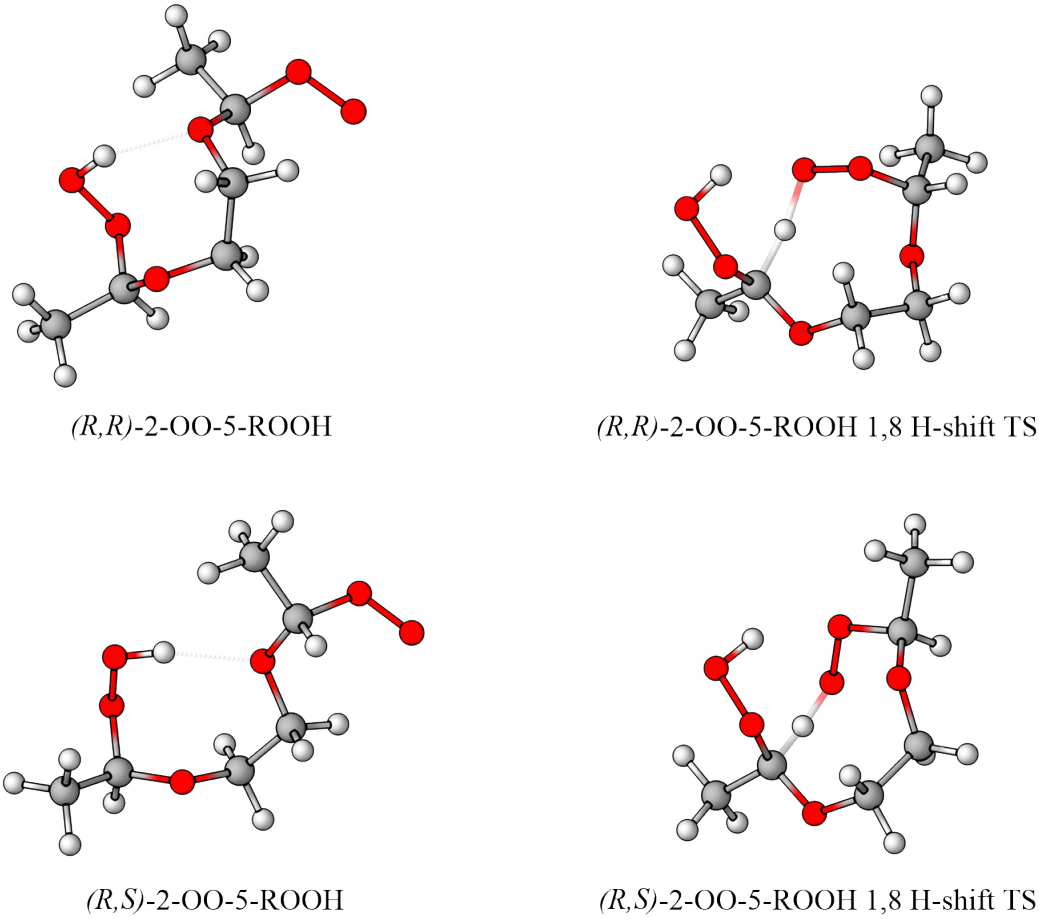

Figure S29: Molecular structure of lowest conformers of (*R,S*)/(*R,R*)-2-OO-5-ROOH and their respective 1,8 H-shift transition states, optimized at the ωB97X-D/aug-cc-pVTZ level of theory. Faded bonds are partially broken. Color code: Gray = C; Red = O; White = H.

6 Box Model Implementation

We implement in the photochemical box model a photo-oxidation mechanism of 1,2-DEE, including the reactions of major peroxy radicals, formation of the first-generation closed-shell products, and important secondary reactions of those products. The full mechanism in .txt is available at: doi.org/10.22002/h46t8-rc655. The reaction kinetics involving formation of key oxidation products discussed in this work are listed in Table S33.

Table S33: Major bimolecular and unimolecular reactions and respective rate constants. All rate constants are evaluated at 294 K and 993 hPa. [a] Calculated based on Calvert et al.[33] [b] Calculated based on Jenkin et al.[3] [c] Branching ratios of bimolecular reactions, rate coefficients of RO_2 H-shift reactions, and equilibrium constants of equilibrium reactions come from derivations in this work.

Bimolecular Reaction	**Rate Constant** ($\times 10^{-11}$ $\frac{cm^3}{molecule \cdot s}$)	**Branching Ratio** [c] (α)
1,2-DEE + OH → 1-RO_2	5.86 [a]	0.01
→ 2-RO_2		0.45
→ 3-RO_2		0.54
1-RO_2 + HO_2 → 1-ROOH + O_2	1.96 [b]	0.96
2-RO_2 + HO_2 → 2-ROOH + O_2	1.96 [b]	0.79
3-RO_2 + HO_2 → 3-ROOH + O_2	1.96 [b]	0.51
2-OO-5-ROOH + HO_2 → 2,5-DiROOH + O_2	2.10 [b]	0.65
→ 2-oxo-5-ROOH + OH + HO_2		0.26
→ 2-O-5-ROOH + OH + O_2		0.09
2-OO-4-ROOH + HO_2 → 2,4-DiROOH + O_2	2.10 [b]	0.80
→ 2-oxo-4-ROOH + OH + HO_2		0.10
→ 2-O-4-ROOH + OH + O_2		0.10
4-OO-2-ROOH + HO_2 → 2,4-DiROOH + O_2	2.10 [b]	0.64
→ 4-oxo-2-ROOH + OH + HO_2		0.13
→ 4-O-2-ROOH + OH + O_2		0.23
Unimolecular Reaction	**Rate Constant** [c] (s^{-1})	
Sum of 1-RO_2 H-shift reactions	0.085	
2-RO_2 $\xrightarrow{O_2}$ 2-OO-5-ROOH (1,8 H-shift)	1.17	
Average of 2-RO_2 and 3-RO_2 1,6 H-shifts	0.18	
Average of 2-RO_2 and 3-RO_2 1,5 H-shifts	0.06	
(*R,R*)-2-OO-5-ROOH → 2-oxo-5-ROOH + OH (1,8 H-shift)	0.027	
(*R,S*)-2-OO-5-ROOH → 2-oxo-5-ROOH + OH (1,8 H-shift)	0.007	
2-OO-5-ROOH 1,5 + 1,6 H-shifts	0.12	

2-OO-4-ROOH → 4-oxo-2-ROOH + OH	(1,6 H-shift)	0.058
4-OO-2-ROOH → 2-oxo-4-ROOH + OH	(1,6 H-shift)	0.029
Chemical Equilibrium		**Equilibrium constant** [c]
2-OO-4-ROOH ⇔ 4-OO-2-ROOH		$\frac{5}{6}$

Major secondary reactions of first-generation closed-shell products include their reactions with OH and photolysis. The reaction kinetics of the OH reactions are directly adopted from Master Chemical Mechanism (MCM, mcm.york.ac.uk/home.htt). For compounds that lack information regarding their OH reactions, the kinetics of structurally similar compounds are used.

The photolytic properties of many functionalized oxidation products (hydroperoxides, aldehydes, and ketohydroperoxides) we examined in this study have so far been understudied. The photolysis rate coefficients of organic hydroperoxides are expected to be close to that of H_2O_2, given the similar absorption cross sections for H_2O_2 and organic hydroperoxides in the 200-350 nm range.[34] The photolysis rate coefficients of H_2O_2 in our chamber are measured in previous studies to be 1.7×10^{-6} s^{-1} under eight 350 nm bulbs and 2.7×10^{-4} s^{-1} under eight 254 nm bulbs.[35,36] These rates are applied to all hydroperoxides in the box model. For ketohydroperoxides, their photolysis rates are estimated assuming additivity of the absorption cross sections of carbonyls and hydroperoxides.[34] Due to lack of knowledge of potential influences on the cross section by the interaction between the functional groups,[37] our estimated photolysis rates of the multifunctional products can be off. Our estimation of the photolysis rate coefficients are in Table S34.

Table S34: Estimated photolysis reaction rate coefficients of relevant compound classes in the system.

	Wavelength	
Molecules	**254 nm**	**350 nm**
H_2O_2 and hydroperoxides	$2.7\ (\pm\ 0.4)\times10^{-4}$ s^{-1}	$1.7\ (\pm\ 0.2)\times10^{-6}$ s^{-1}
Ketohydroperoxides	$3.0\ (\pm\ 0.4)\times10^{-4}$ s^{-1}	$1.9\ (\pm\ 0.2)\times10^{-6}$ s^{-1}

Overall, we estimate that secondary chemistry of the oxidation products accounts for ~8% loss in their measured concentrations. Since our analysis in this study is derived from ratios between concentrations of oxidation products with similar secondary chemistry, the influence of secondary chemistry on our analysis of the key reaction parameters is much smaller.

7 Experimental Results

7.1 Table of Results

Table S35: Experimental results with all data corrected. All concentrations are in ppb. HO_2 concentrations are determined by the box model. [a] Here we assume that the remaining two GC peaks in Figure S4 all refer to 2,4-DiROOH. This assumption is further discussed in Section S8.3

Exp. No.	[HO_2]	[1-ROOH]	[2-ROOH]	[3-ROOH]	[2-oxo-5-ROOH]	[4-oxo-2-ROOH]	[2-oxo-4-ROOH]	[3-oxo-2-ROOH] + [2-oxo-3-ROOH]
1	0.18	0.009	0.04	0.15	0.13	0.08	0.04	0.01
2	2.33	0.08	1.55	2.18	0.53	0.07	0.05	0.05
		0.15	3.04	4.37	1.00	0.13	0.11	0.08
3	1.33	0.39	5.13	9.43	2.87	0.48	0.35	0.25
4	0.10	0.02	0.06	0.23	0.36	0.25	0.12	0.04
5	0.19	0.008	0.04	0.14	0.15	0.09	0.05	0.02
		0.05	0.26	0.91	1.16	0.65	0.33	0.14
6	1.01	0.22	2.72	5.41	2.04	0.41	0.28	0.17
		0.28	3.80	7.38	2.80	0.58	0.39	0.23
7	0.07	0.01	0.04	0.15	0.31	0.23	0.10	0.03
		0.01	0.05	0.18	0.37	0.29	0.12	0.04
8	1.86	0.17	2.68	4.18	1.09	0.17	0.12	0.10
		0.32	5.17	8.06	2.11	0.34	0.26	0.18
9	0.13	0.02	0.08	0.28	0.28	0.19	0.08	0.04
		0.03	0.14	0.50	0.58	0.36	0.17	0.07
10	0.09	0.02	0.06	0.22	0.29	0.20	0.09	0.04
		0.02	0.07	0.27	0.35	0.25	0.11	0.4
11	1.36	0.21	3.13	5.43	1.66	0.28	0.20	0.16
		0.39	6.32	10.9	3.23	0.59	0.43	0.27
12	0.99	0.09	1.21	2.48	0.89	0.18	0.12	0.09
		0.18	2.35	4.64	1.82	0.36	0.26	0.15

Exp. No.	[HO_2]	[1-ROOH]	[2-ROOH]	[3-ROOH]	[2-oxo-5-ROOH]	[4-oxo-2-ROOH]	[2-oxo-4-ROOH]	[3-oxo-2-ROOH] + [2-oxo-3-ROOH]
13	2.27	0.10	1.94	2.85	0.65	0.10	0.07	0.05
		0.21	3.93	5.73	1.27	0.20	0.16	0.11

Exp. No.	[HO_2]	[2-OOH-5-R'CHO]	[3-OOH-5-R'CHO]	[(*R*,*S*)-2,5-DiROOH]	[(*R*,*R*)-2,5-DiROOH]	[2,4-DiROOH][a]
1	0.18	0.03	0.01	0.10	0.10	0.14
2	2.33	0.16	0.05	0.63	0.64	0.60
		0.30	0.09	1.28	1.27	1.29
3	1.33	0.94	0.27	3.50	3.40	3.40
4	0.10	0.04	0.02	0.20	0.18	0.25
5	0.19	0.03	0.01	0.11	0.10	0.14
		0.18	0.08	0.89	0.83	1.12
6	1.01	0.56	0.19	2.24	2.21	2.33
		0.73	0.26	3.25	3.23	3.42
7	0.07	0.03	0.01	0.14	0.12	0.17
		0.04	0.02	0.18	0.16	0.22
8	1.86	0.38	0.09	1.28	1.26	1.42
		0.76	0.23	2.42	2.37	2.82
9	0.13	0.06	0.02	0.18	0.17	0.23
		0.10	0.03	0.36	0.34	0.48
10	0.09	0.04	0.02	0.16	0.15	0.19
		0.05	0.02	0.21	0.19	0.25
11	1.36	0.49	0.16	1.88	1.91	2.11
		1.09	0.32	3.91	3.96	3.91
12	0.99	0.23	0.09	1.06	1.04	1.17
		0.46	0.17	2.05	1.99	2.31
13	2.27	0.20	0.06	0.80	0.82	0.83
		0.43	0.13	1.60	1.56	1.67

7.2 Vapor Wall Loss

Vapor wall loss refers to the partitioning of gas-phase organic products onto chamber walls, thereby removing them from the system. The vapor wall loss of major oxidation products are quantified by measuring their decay after irradiation. We then correct the yields of the oxidation products using the estimated wall loss rate. The wall loss rate is estimated by fitting the dark decay of the compounds of interests, which gives 9.38×10^{-6} s^{-1} for ROOH's, 3.30×10^{-5} s^{-1} for ketohydroperoxides, and 4.95×10^{-5} s^{-1} for dihydroperoxides.

The observed vapor wall loss rate for dihydroperoxides are smaller than our expectation, since those compounds are expected to have very low volatility and would readily partition into the condensed phase.[38] The potential underestimation is likely due to the short equilibrium timescale for low-volatility vapor between the gas-phase and the wall-phase.[39,40] Smaller the vapor-wall equilibrium timescale of a compound, earlier the wall loss process starts to affect its detectable gas phase concentration. The compound likely already approaches gas-wall equilibrium during the oxidation period, which would result in a smaller decay observed after oxidation. The potential underestimation of wall loss of dihydroperoxides can lead to biases in our estimations of some parameters. For example, overestimation in the slope in Fig. 6 and 7 would lead to underestimation of 1,8 H-shift rate coefficient of 2-RO_2 and overestimation of 1,8 H-shift rate coefficient of 2-OO-5-ROOH.

7.3 GC Transmission Efficiency

A certain portion of the reaction products can be lost by decomposition and/or reaction with the column surface as they are traveling through the column. The GC transmission efficiencies of the products are evaluated by comparing their measured concentrations when sampled directly from the chamber with those when sampled from GC. Losses are often greater for compounds eluting at higher temperature. In our experiments, we observe no noticeable loss for products eluting at lower temperatures (<80 °C), i.e. the hydroperoxides and ketohydroperoxides. For dihydroperoxides eluting at >100 °C, we observe a GC transmission rate at ~80-90%, which is accounted for when quantifying the yields of those products.

8 Additional Results and Discussion

8.1 $\alpha_{\mathbf{RO_2}}$ and $\alpha_{\mathbf{ROOH}}$

The branching fractions of respective simple RO_2 (α_{RO_2}) during the initiation step and the branching fractions to the formation of respective ROOH (α_{ROOH}) from bimolecular reactions RO_2+HO_2 (Scheme S1) can be derived by analyzing the variation in the yields of ROOHs as a function of $[HO_2]$.

Here we use the ratio of the yields of 2-ROOH and 1-ROOH ([2-ROOH]/[1-ROOH]) as an example. We assume the ratio of the yields of the two compounds is equal to the ratio of their formation rates, which can be formulated as:

$$\frac{[\text{2-ROOH}]}{[\text{1-ROOH}]} = \frac{\alpha_{\text{2-ROOH}} k_{\text{2-RO}_2+\text{HO}_2} [\text{2-RO}_2]_{ss} [\text{HO}_2]}{\alpha_{\text{1-ROOH}} k_{\text{1-RO}_2+\text{HO}_2} [\text{1-RO}_2]_{ss} [\text{HO}_2]} = \frac{\alpha_{\text{2-ROOH}} [\text{2-RO}_2]_{ss}}{\alpha_{\text{1-ROOH}} [\text{1-RO}_2]_{ss}} \tag{S19}$$

where $[\text{2-RO}_2]_{ss}$ and $[\text{1-RO}_2]_{ss}$ indicates steady state concentrations of $[\text{2-RO}_2]$ and $[\text{1-RO}_2]$.

To derive expressions for $[\text{2-RO}_2]_{ss}$ and $[\text{1-RO}_2]_{ss}$, we start with the rate equations of $[\text{2-RO}_2]$ and $[\text{1-RO}_2]$:

$$\begin{aligned} \frac{d}{dt}[\text{2-RO}_2] = {} & \alpha_{\text{2-RO}_2} k_{DEE+OH} [\text{DEE}][\text{OH}] - k_{\text{2-RO}_2+\text{HO}_2} [\text{2-RO}_2][\text{HO}_2] \\ & - k_{\text{H-shifts,2-RO}_2} [\text{2-RO}_2] \end{aligned} \tag{S20}$$

$$\begin{aligned} \frac{d}{dt}[\text{1-RO}_2] = {} & \alpha_{\text{1-RO}_2} k_{DEE+OH} [\text{DEE}][\text{OH}] - k_{\text{1-RO}_2+\text{HO}_2} [\text{1-RO}_2][\text{HO}_2] \\ & - k_{\text{H-shifts,1-RO}_2} [\text{1-RO}_2] \end{aligned} \tag{S21}$$

where $k_{\text{H-shifts, RO}_2}$ indicates the total H-shift rate coefficients of respective RO_2. Assuming steady states for equation S20 and S21 gives:

$$[\text{2-RO}_2]_{ss} = \frac{\alpha_{\text{2-RO}_2} k_{DE+OH} [\text{DEE}][\text{OH}]}{k_{\text{2-RO}_2+\text{HO}_2} [\text{HO}_2] + k_{\text{H-shifts,2-RO}_2}} \tag{S22}$$

$$[\text{1-RO}_2]_{ss} = \frac{\alpha_{\text{1-RO}_2} k_{DEE+OH} [\text{DEE}][\text{OH}]}{k_{\text{1-RO}_2+\text{HO}_2} [\text{HO}_2] + k_{\text{H-shifts,1-RO}_2}} \tag{S23}$$

Plugging equation S22 and S23 into equation S19 gives:

$$\begin{aligned} \frac{[\text{2-ROOH}]}{[\text{1-ROOH}]} &= \frac{\alpha_{\text{2-ROOH}} [\text{2-RO}_2]_{ss}}{\alpha_{\text{1-ROOH}} [\text{1-RO}_2]_{ss}} \\ &= \frac{\alpha_{\text{2-ROOH}}}{\alpha_{\text{1-ROOH}}} \cdot \frac{\alpha_{\text{2-RO}_2}}{\alpha_{\text{1-RO}_2}} \cdot \frac{k_{\text{1-RO}_2+\text{HO}_2} [\text{HO}_2] + k_{\text{H-shifts,1-RO}_2}}{k_{\text{2-RO}_2+\text{HO}_2} [\text{HO}_2] + k_{\text{H-shifts,2-RO}_2}} \end{aligned} \tag{S24}$$

Based on Equation S24, the yield of simple hydroperoxides in the system is mainly governed by the following parameters: 1) the branching ratio of simple RO_2 in the initiation step, 2) the branching ratio of RO_2+HO_2 reaction to ROOH formation, and 3) the unimolecular H-shift reaction rate coefficients of RO_2. When [HO_2] is sufficiently high that the RO_2 bimolecular reaction rates vastly exceed their H-shift reaction rates, ideally, the ratio of the yields of ROOHs should equal to the ratio of branching fractions of the ROOH formation pathways ($(\alpha_{2\text{-}RO_2} \cdot \alpha_{2\text{-}ROOH})/(\alpha_{1\text{-}RO_2} \cdot \alpha_{1\text{-}ROOH}$) in Equation S24). As [$HO_2$] decreases, the H-shift reactions become more significant in influencing the ratio of the product yields. We use box model simulations to facilitate our estimation of those parameters to produce the best model fit to experimental data.

We first estimate the branching ratio of simple RO_2 in the initiation step (α_{RO_2}) based on observed yields of relevant oxidation products. The branching fraction to formation of 1-RO_2 (α_{1-RO_2}) is estimated by comparing the yield of 1-ROOH to that of all oxidation products in the system, given that 1-ROOH is the dominant oxidation product from 1-RO_2 pathway. From this analysis, $\alpha_{1\text{-}RO_2}$ is estimated to be 0.01 (1%). The branching fraction of 2-RO_2 ($\alpha_{2\text{-}RO_2}$) is estimated by comparing the yields of 2-ROOH and all products from 2-RO_2 1,8 H-shift – its major autoxidation pathway – to the total yield of oxidation products, which gives $\alpha_{2\text{-}RO_2}$ = 0.45. The remaining $\alpha_{3\text{-}RO_2}$ is thereby derived by calculating $1 - \alpha_{1\text{-}RO_2} - \alpha_{2\text{-}RO_2}$, which equals 0.54. The branching fractions of RO_2 from oxidation of 1,2-DEE-d_4 are derived by comparing the yields of deuterated ROOH with those of their non-deuterated counterparts (Scheme S1, Figure S1). We observe that the abstraction of a D atom from the methylene site between the two oxygen atoms ($\alpha_{3\text{-}RO_2\text{-}d_3}$) is about a factor of 2.6 slower than the abstraction of an H atom ($\alpha_{3\text{-}RO_2}$).

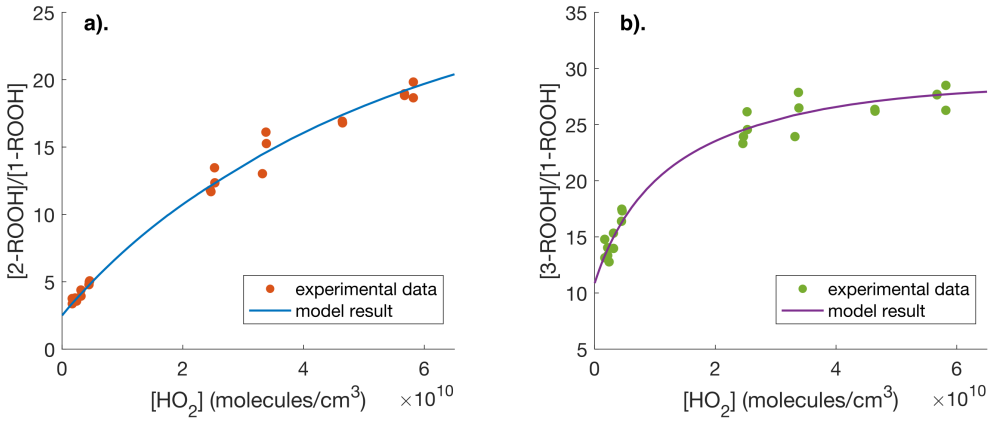

Figure S30: **(a)** [2-ROOH]/[1-ROOH] vs. [HO_2], and **(b)** [3-ROOH]/[1-ROOH] vs. [HO_2]. The solid lines represent the optimized model fit to the data. In box model simulation here, we use $k_{\text{H-shifts, 1-RO}_2}$ = 0.085 s^{-1}, $k_{\text{H-shifts, 2-RO}_2}$ = 1.4 s^{-1}, and $k_{\text{H-shifts, 3-RO}_2}$ = 0.25 s^{-1}.

With the derived α_{RO_2}, we estimate α_{ROOH} and the total H-shift rate coefficients of involved RO_2 ($k_{\text{H-shifts, RO}_2}$) based on the variation of [2-ROOH]/[1-ROOH] and

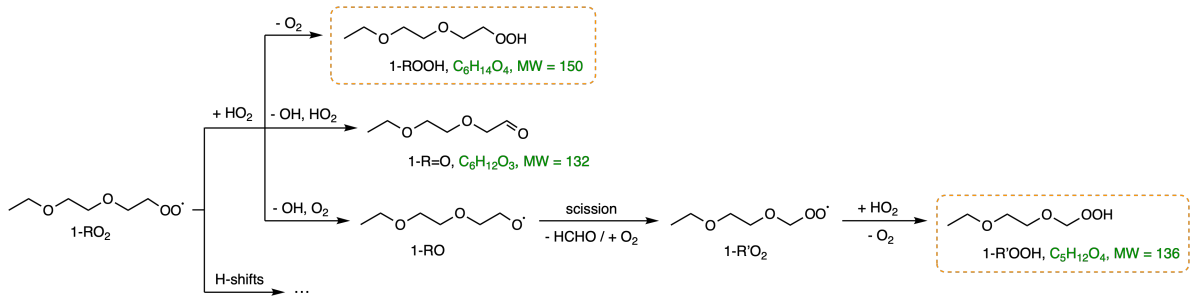

Scheme S7: Proposed mechanism of 1,2-DEE 1-RO_2+HO_2 reactions. The molecular masses of major closed-shell products are denoted in green. The products detected by our instrument are shown in orange boxes.

[3-ROOH]/[1-ROOH] as a function of [HO_2], which is shown in Figure S30. The resulted reaction parameters from the best fit of the model to the experimental data are in Table S33. Here we assume that $\alpha_{\text{1-ROOH}}$ = 0.96 based on our observation of reaction products from 1-RO_2+HO_2 reaction (Scheme S7). We detect low yield of 1-R'OOH in Scheme S7 at ~4% of the yield of 1-ROOH in our experiments. The simple assumption that 1-ROOH and 1-R'OOH are the only products from 1-RO_2+HO_2 reaction may lead to a slight overestimation of $\alpha_{\text{1-ROOH}}$, leading to overestimation of $\alpha_{\text{2-ROOH}}$, $\alpha_{\text{3-ROOH}}$, and 2-RO_2 and 3-RO_2 H-shift rates. However, the observed yields of relevant reaction products and previous studies suggest that $\alpha_{\text{1-ROOH}}$ is likely >0.9,[3] and thus our assumption here should not contribute significantly to the overall uncertainty in our estimated reaction parameters.

8.2 2-OO-5-ROOH reactions

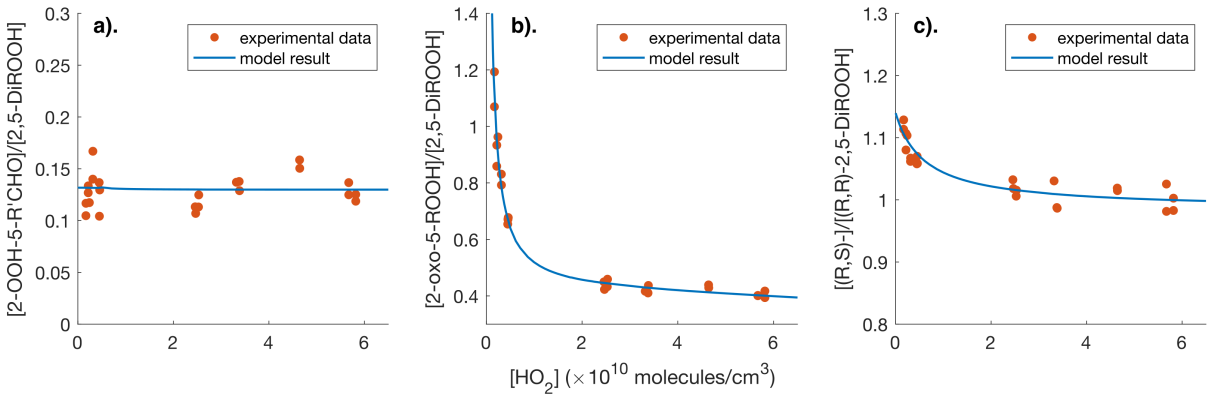

Figure S31: Yields of various oxidation products from 2-OO-5-ROOH vs. [HO_2]. **(a)** [2-OOH-5-R'CHO]/[2,5-DiROOH], **(b)** [2-oxo-5-ROOH]/[2,5-DiROOH], **(c)** [(*R,S*)-2,5-DiROOH]/[(*R,R*)-2,5-DiROOH]. Model results are based on derived parameters shown in Table S33.

Shown in Figure S31 is experimental and modeled results of the variations in the yields of various oxidation products from 2-OO-5-ROOH reactions as a function of [HO_2]. Those relationships are used to derived reaction parameters of 2-OO-5-ROOH bimolecular and unimolecular reactions (Fig. 4), which are shown in Table 2 and Table S33.

The ratios of [2-OOH-5-R'CHO]/[2,5-DiROOH] and [2-oxo-5-ROOH]/[2,5-DiROOH] (Figure S31a and b), as discussed in the main text, are used to estimate the branching fractions of three channels of bimolecular reaction 2-OO-5-ROOH + HO_2 (Fig. 4), as well as the 1,8 H-shift rate coefficient of 2-OO-5-ROOH. Since we do not observe products from other possible reaction pathways of 2-O-5-ROOH (e.g. alkoxy radical isomerization), we assume the scission pathway that leads to formation of 2-OOH-5'CHO the only product derived from 2-O-5-ROOH. The variation in [2-OOH-5-R'CHO]/[2,5-DiROOH] at varied [HO_2] is small, since both products are produced through reaction 2-OO-5-ROOH + HO_2 and the ratio is largely determined by the ratio between the branching fractions $\alpha_{\text{2-O-5-ROOH}}/\alpha_{\text{2,5-DiROOH}}$. In constrast, with the decrease of [HO_2], the yield of 2-oxo-5-ROOH increases compared to that of 2,5-DiROOH as 1,8 H-shift reaction of 2-OO-5-ROOH becomes more important in the formation of 2-oxo-5-ROOH.

Figure S31c shows the ratios between the yields of the two diatereomers of 2,5-DiROOH based on our tentative peak assignment in Fig. 5 and S4. The stereoisomer-specific 1,8 H-shift rate coefficient of 2-OO-5-ROOH can be derived by comparing the yields of the two diastereomers as a function of HO_2 concentrations. The stereoisomer with higher H-shift rate coefficient should produce less corresponding dihydroperoxides at lower HO_2 level. If the tentative peak assignment in Fig. 5 is incorrect, our analysis of (*R,S*) and (*R,R*) diastereomers would be reversed. By fitting the experimental data by box model simulation, we estimate the 1,8 H-shift rate coefficient of (*R,R*)-2-OO-5-ROOH to be 0.027 ± 0.017 s^{-1}, and that of the (*R,S*) isomer to be 0.007 ± 0.004 s^{-1}. Although our estimates do not fully agree with the theoretical predictions (Table S7), they capture the trend that the H-shift rate of the (*R,R*) isomer is ~4 times that of the (*R,S*) isomer.

To estimate the rate coefficients of H-shift processes other than the 1,8 H-shift of 2-OO-5-ROOH, i.e. its 1,5 and 1,6 H-shift, we again look at the ratio between the yields of 2-ROOH and direct oxidation products from 2-OO-5-ROOH. The linear relationship between the ratio and [HO_2] shows an intercept of ~0.06. This non-zero intercept likely attributes to 1,5 and 1,6 H-shift reactions of 2-OO-5-ROOH, which reduce the overall yield of its oxidation products from bimolecular and 1,8 H-shift reactions. From the intercept, we estimate the sum of 1,5 and 1,6 H-shift rate coefficients of 2-OO-5-ROOH through box model simulation, as shown in Figure S32. By fitting the experimental data with different 2-OO-5-ROOH 1,5 + 1,6 H-shift rate coefficients, we estimate that the combined rate of these shifts is ~0.12 s^{-1}, which is within a factor of 5 of the theoretical values of those H-shifts (Table S7).

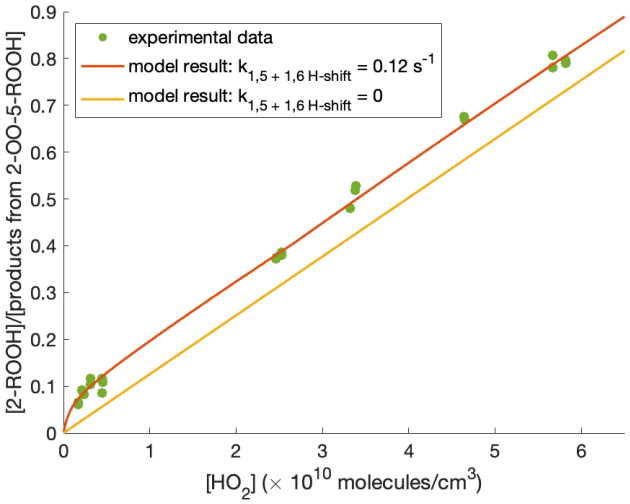

Figure S32: [2-ROOH]/([2-oxo-5-ROOH] + [2-OOH-5-R'CHO] + [2,5-DiROOH]) vs. [HO_2] at ambient temperature (294K), with model results of this relationship at different 1,5 + 1,6 H-shift rate coefficients of 2-OO-5-ROOH.

8.3 1,5 and 1,6 H-shifts of 2- and 3-RO_2

Due to the rapid OOH H-scrambling reaction between the hydroperoxy RO_2 formed via 1,5/1,6 H-shift reactions of 2-RO_2 and 3-RO_2 (Scheme S2 and S3), we are unable to distinguish the oxidation products from 1,5/1,6 H-shift of each individual RO_2. Therefore, our estimated rate coefficients of the H-shift reactions represent an average of the process for both RO_2 species. We start with discussion of estimation of the average 1,6 H-shift rates, as the reaction products from 1,6 H-shift pathways have higher yields and thus are better resolved. Note that here we attribute the last two DiROOH GC peaks in Figure S4 all to 2,4-DiROOH as denoted in Table S35, since we are unable to distinguish 2,3-DiROOH from 2,4-DiROOH under our chromatographic conditions and we assume based on computational results that the 1,5 H-shifts are much slower than the 1,6 H-shifts. Given that it is possible that 2,3-DiROOH co-elute with 2,4-DiROOH, our following estimation of 1,6 H-shifts should be regarded as an upper limit. We also refrain from conducting stereoselective analyses for the reaction processes discussed below, as the current peak assignments remain uncertain.

Similar to our estimation of the 2-RO_2 1,8 H-shift rate coefficient, we compare the rates of the bimolecular pathway of both RO_2 with their unimolecular pathway:

$$\begin{aligned}
&\frac{[\text{2-ROOH}]/\alpha_{\text{2-ROOH}} + [\text{3-ROOH}]/\alpha_{\text{3-ROOH}}}{[\text{all products from 2-RO2 and 3-RO2 1,6 H-shifts}]} \\
&= \frac{[\text{2-ROOH}]/\alpha_{\text{2-ROOH}} + [\text{3-ROOH}]/\alpha_{\text{3-ROOH}}}{[\text{2,4-DiROOH}] + [\text{2-oxo-4-ROOH}] + [\text{4-oxo-2-ROOH}] + [\text{3-OOH-5-R'CHO}] + [\text{4-O-2-ROOH}]} \\
&= \frac{k_{RO_2+HO_2}[\text{2-}RO_2][HO_2] + k_{RO_2+HO_2}[\text{3-}RO_2][HO_2]}{k_{\text{1,6 H-shifts, 2-RO2 \& 3-RO2}}([\text{2-}RO_2] + [\text{3-}RO_2])} \\
&= \frac{k_{RO_2+HO_2}}{k_{\text{1,6 H-shifts, 2-RO2 \& 3-RO2}}}[HO_2]
\end{aligned} \tag{S25}$$

From Equation S25, we should observe a linear relationship between the yields of simple ROOHs divided by their branching fractions from RO_2+HO_2 reaction and the total yields of all oxidation products from the 1,6 H-shift pathways (Scheme S3). The only unknown quantity from the expression is the yield of the alkoxy radical 4-O-2-ROOH, which likely undergoes scission reation forming a variety of C3 products (Scheme S8). However, the C3 products from 1,2-DEE oxidation can arise through a variety of pathways, making it particularly challenging to resolve individual contributions of each pathway, which is not the focus of this study. Thus, we resort to estimate the branching fractions of 2-OO-4-ROOH+HO_2 and 4-OO-2-ROOH+HO_2 reactions, which also enables us to derive the yield of 4-O-2-ROOH.

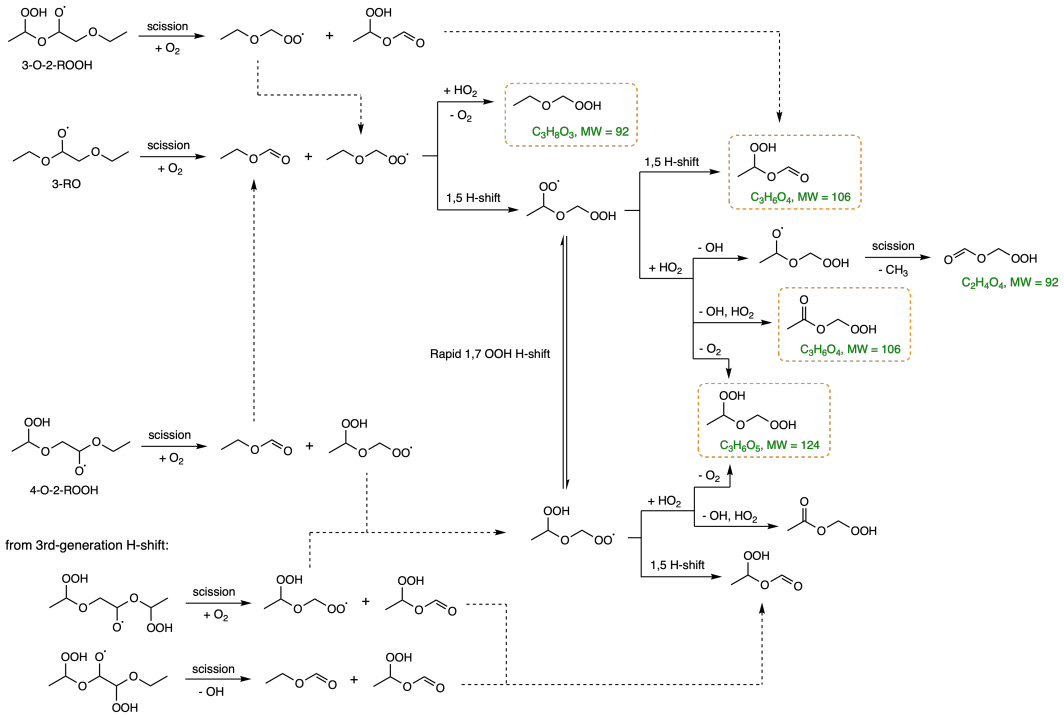

Scheme S8: Proposed formation pathways of C3 products from 1,2-DEE oxidation. The molecular masses of major closed-shell products are denoted in green. Products detected by our instrument are shown in orange boxes.

Similar to the approach discussed in the main text and the previous section, we analyze the following ratios of oxidation product yields to estimate the branching ratios: [3-OOH-5-R'CHO]/[2,4-DiROOH], ([2-oxo-4-ROOH]+[4-oxo-2-ROOH])/[2,4-DiROOH], and [4-oxo-2-ROOH]/[2-oxo-4-ROOH], as shown in Figure S33. The first two ratios are used to estimate the average values of key reaction parameters of 2-OO-4-ROOH and 4-OO-2-ROOH bimolecular and unimolecular reactions, the latter one is used to determine the equilibrium constant of 2-OO-4-ROOH ⇔ 4-OO-2-ROOH and differentiate the performance of 2-OO-4-ROOH and 4-OO-2-ROOH reactions. Our estimates of key reaction parameters are shown in Table S33 and S36, including the branching fractions of 2-OO-4-ROOH and 4-OO-2-ROOH + HO_2 reactions, equilibrium constant of 2-OO-4-ROOH ⇔ 4-OO-2-ROOH, and the rate coefficients

of 1,6 H-shift reactions of 2-OO-4-ROOH and 4-OO-2-ROOH.

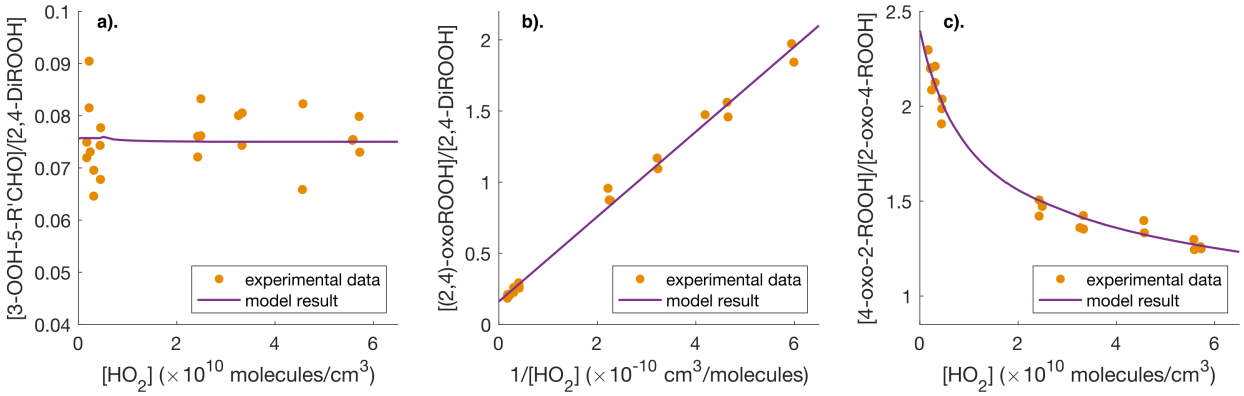

Figure S33: Yields of various oxidation products from 2-OO-4-ROOH and 4-OO-2-ROOH vs. [HO_2]. **(a)** [3-OOH-5-R'CHO]/[2,4-DiROOH], **(b)** ([2-oxo-4-ROOH]+[4-oxo-2-ROOH])/[2,4-DiROOH], **(c)** [4-oxo-2-ROOH]/[2-oxo-4-ROOH]. Model results are based on derived parameters shown in Table S33 and S36.

Table S36: Estimates of key reaction parameters involving 2-OO-4-ROOH and 4-OO-2-ROOH. [a] Chemical equilibrium of 2-OO-4-ROOH ⇔ 4-OO-2-ROOH. [b] Branching fractions of bimolecular reactions with HO_2 [c] Rate coefficients of H-shift reactions.

2-OO-4-ROOH	$f_{\text{2-OO-4-ROOH}}$ [a]	$\alpha_{\text{2,4-DiROOH}}$ [b]	$\alpha_{\text{2-oxo-4-ROOH}}$ [b]	$\alpha_{\text{2-O-4-ROOH}}$ [b]	$k_{\text{1,6 H-shift}}$ (s^{-1})[c]
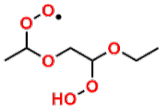	$\frac{6}{11}$	0.80	0.10	0.10	0.058
4-OO-2-ROOH	$f_{\text{4-OO-2-ROOH}}$ [a]	$\alpha_{\text{2,4-DiROOH}}$ [b]	$\alpha_{\text{4-oxo-2-ROOH}}$ [b]	$\alpha_{\text{4-O-2-ROOH}}$ [b]	$k_{\text{1,6 H-shift}}$ (s^{-1})[c]
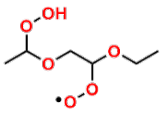	$\frac{5}{11}$	0.64	0.13	0.23	0.029

With the derived branching fractions of 2-OO-4-ROOH and 4-OO-2-ROOH + HO_2 reactions, Equation S25 can be rewritten as:

$$\frac{[\text{2-ROOH}]/\alpha_{\text{2-ROOH}} + [\text{3-ROOH}]/\alpha_{\text{3-ROOH}}}{[\text{2,4-DiROOH}] + [\text{2-oxo-4-ROOH}] + [\text{4-oxo-2-ROOH}] + [\text{3-OOH-5-R'CHO}] + [\text{4-O-2-ROOH}]}$$
$$= \frac{[\text{2-ROOH}]/\alpha_{\text{2-ROOH}} + [\text{3-ROOH}]/\alpha_{\text{3-ROOH}}}{[\text{2,4-DiROOH}]\left(1 + \frac{f_{\text{4-OO-2-ROOH}}\alpha_{\text{4-O-2-ROOH}}}{\alpha_{\text{2,4-DiROOH, average}}}\right) + [\text{2-oxo-4-ROOH}] + [\text{4-oxo-2-ROOH}] + [\text{3-OOH-5-R'CHO}]}$$
$$= \frac{k_{RO_2+HO_2}}{k_{\text{1,6 H-shifts, 2-RO2 \& 3-RO2}}}[HO_2] \quad \text{(S26)}$$

Based on Equation S26, a linear relationship is observed with a slope of (1.10 ± 0.35) × 10^{-10} cm^3 $molecules^{-1}$ as shown in Figure S34. The average of the rate coefficients of 2-RO_2 and 3-RO_2 1,6 H-shift reactions are thus estimated to be ~0.18 ± 0.11 s^{-1}.

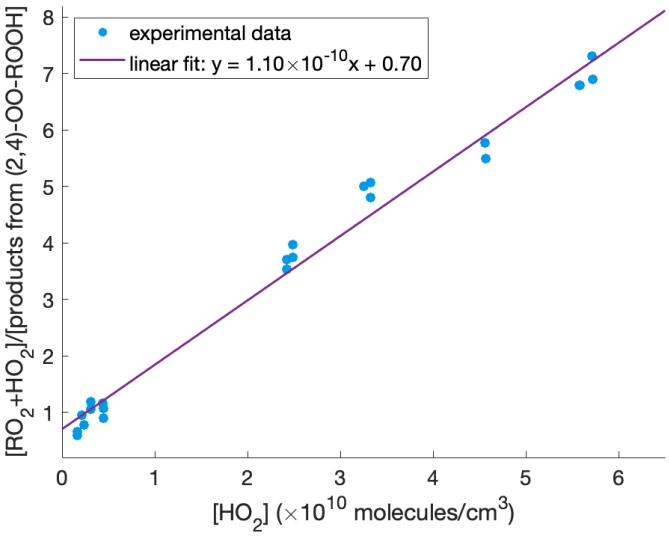

Figure S34: $k_{RO_2+HO_2}$ vs. $k_{1,6\text{ H-shift, 2-RO2 \& 3-RO2}}$ at ambient temperature (294 K), and the result from linear regression fit (R^2 = 0.985).

We met difficulties when quantifying the yields of products derived from the 1,5 H-shifts of 2-RO_2 and 3-RO_2, as these reactions likely proceed much more slowly than other H-shift processes (Table S33). To estimate the average 1,5 H-shift rate coefficients of 2-RO_2 and 3-RO_2, we compared the yields of 2-ROOH and 3-ROOH with those of 2-oxo-3-ROOH and 3-oxo-2-ROOH, which are the only resolvable products from the 1,5 H-shifts. With box model simulation, as shown in Figure S35, we estimate the rate coefficients to be ~0.06 s^{-1}.

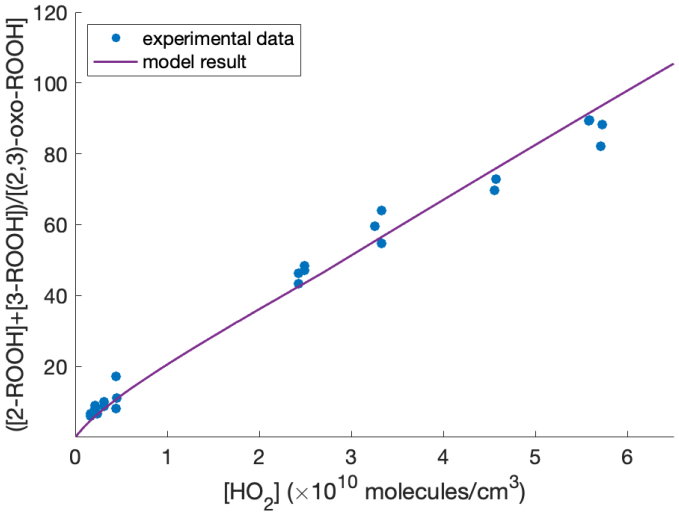

Figure S35: ([2-ROOH]+[3-ROOH])/([2-oxo-3-ROOH]+[3-oxo-2-ROOH]) vs. [HO_2]. Model result are based on parameters shown in Table S33. Here for 2-OO-3-ROOH and 3-OO-2-ROOH + HO_2 reactions, we assume they have the same reaction parameters as 2-OO-4-ROOH and 4-OO-2-ROOH + HO_2 reactions, respectively.

9 Estimation of Uncertainties

Similar method for determining uncertainties is also documented in our previous publications:[36,41] doi.org/10.1021/acs.jpca.3c04456 and doi.org/10.1021/acsestair.5c00204.

9.1 HO_2 Concentrations

The rate equations for the dominant production and loss pathways of HO_x species in our experiments are formulated as follows:

$$P(OH) = 2J_{H_2O_2}[H_2O_2] \tag{S27}$$

$$L(OH) = (k_{OH+H_2O_2}[H_2O_2] + k_{OH+CH_3OH}[CH_3OH] + k_{OH+VOC}[VOC])[OH] \tag{S28}$$

$$P(HO_2) = (k_{OH+H_2O_2}[H_2O_2] + k_{OH+CH_3OH}[CH_3OH] + \alpha \cdot k_{OH+VOC}[VOC])[OH] \tag{S29}$$

$$L(HO_2) = 2k_{HO_2+HO_2}[HO_2]^2 + k_{RO_2+HO_2}[RO_2][HO_2] \tag{S30}$$

where α in Equation S29 indicates the branching ratio for HO_2 production through reactions of VOCs and OH, $k_{OH+H_2O_2}$ = 1.8×10^{-12} cm^3 molecules^{-1} s^{-1} based on Vakhtin et al.,[42] k_{OH+CH_3OH} = 8.8×10^{-13} cm^3 molecules^{-1} s^{-1} at 294K based on MCM, and k_{OH+DEE} = 5.86×10^{-11} cm^3 molecules^{-1} s^{-1} at 294 K based on Calvert et al.[33] In our experiments, the concentration of CH_3OH is kept much higher than that of the VOCs in order to suppress RO_2+RO_2 chemistry. On average, ~82% of OH radical reacts with H_2O_2 and CH_3OH, and ~18% reacts with 1,2-DEE. We thereby simplify equations S28 to S30 as:

$$L(OH) \simeq (k_{OH+H_2O_2}[H_2O_2] + k_{OH+CH_3OH}[CH_3OH])[OH] \tag{S31}$$

$$P(HO_2) \simeq (k_{OH+H_2O_2}[H_2O_2] + k_{OH+CH_3OH}[CH_3OH])[OH] \tag{S32}$$

$$L(HO_2) \simeq 2k_{HO_2+HO_2}[HO_2]^2 \tag{S33}$$

Therefore, consumption of OH in our system mostly leads to formation of HO_2, and assuming steady state for OH and HO_2 equalizes the equations above and gives:

$$\begin{aligned} 2k_{HO_2+HO_2}[HO_2]^2 &\simeq 2J_{H_2O_2}[H_2O_2] \\ [HO_2] &\simeq \sqrt{\frac{J_{H_2O_2}[H_2O_2]}{k_{HO_2+HO_2}}} \end{aligned} \tag{S34}$$

which indicates that [HO_2] in our system is approximately proportional to the square root of the photolysis rate coefficient of H_2O_2, which can be modified by changing the number and wavelengths of the UV lamps in our chamber enclosure.

Based on Equation S34, the HO_2 concentrations in our system are mainly constrained by the photolysis rate coefficients of H_2O_2, H_2O_2 concentrations, and the rate coefficient of the self-reaction of HO_2. The uncertainties in the photolysis rate coefficients of H_2O_2 are determined by the uncertainties in the fitted slopes used to evaluate these rate coefficients (Table S34). The major source of uncertainties in the concentrations of H_2O_2 comes from our sample preparation procedure and instrumentation, which we estimate to introduce a ~20% systematic error in the measured [H_2O_2]. The uncertainty in $k_{HO_2+HO_2}$ is evaluated using the method in JPL documentation[43] to be ±21% at ambient temperature. As a result, propagation of error gives an uncertainty of ~16% in the estimated [HO_2] in our experiments.

9.2 Product Concentrations and Ratios of Product Yields

The major source of uncertainties in the measured concentrations of oxidation products lies in the instrument sensitivity of the product. The uncertainty in the measured sensitivity of ethylene glycol (Table S2) is calculated as the standard deviation of replicate measurements, which is ~8%. This part of uncertainty is then propagated to the calculated sensitivities of other oxidation products. However, since this component of error is correlated by common measurements, it cannot be used to propagate the error in the ratios between product concentrations.

Another source of uncertainty in the sensitivities comes from the error in the calculated ion-molecule collision rate coefficients, which can be derived from the error in the calculated polarizabilities and dipole moments.[5] The resulted ~20% error is not correlated and thus can be used to infer the uncertainties in the ratios between the yields of different products. Therefore, we estimate the uncertainties in the concentrations of detected products to be ~22%, and the uncertainties in the ratios between product concentrations to be ~28%.

Table S37: Sources of uncertainties for reaction parameters determined in this study. [a] Uncertainty in $k_{RO_2+HO_2}$ are derived from that of $k_{C_2H_5O_2+HO_2}$ based on method in JPL documentation.[43]

Quantity	Constraints	Sources of Uncertainty	Value
$\alpha_{\text{1-RO}_2}$	$\frac{\text{[1-ROOH]}}{\text{[all oxidation products]}}$ (28%)		0.01 ± 0.003
$\alpha_{\text{2-RO}_2}$	$\frac{\text{[2-ROOH]+[all products from 2-OO-5-ROOH]}}{\text{[all oxidation products]}}$ (28%)		0.45 ± 0.14
$\alpha_{\text{3-RO}_2}$	$1 - \alpha_{\text{2-RO}_2} - \alpha_{\text{3-RO}_2}$		0.54 ± 0.15
$\alpha_{\text{1-ROOH}}$	$\frac{\text{[1-R'OOH]}}{\text{[1-ROOH]}}$ (28%)		0.96 + 0.04 / − 0.27
$\alpha_{\text{2-ROOH}}$	$\frac{\text{[2-ROOH]}}{\text{[1-ROOH]}}$ (28%), $\frac{\alpha_{\text{2-RO}_2}}{\alpha_{\text{1-RO}_2} \cdot \alpha_{\text{1-ROOH}}}$ (28%)		0.79 + 0.21 / − 0.31
$\alpha_{\text{3-ROOH}}$	$\frac{\text{[3-ROOH]}}{\text{[1-ROOH]}}$ (28%), $\frac{\alpha_{\text{3-RO}_2}}{\alpha_{\text{1-RO}_2} \cdot \alpha_{\text{1-ROOH}}}$ (28%)		0.51 ± 0.20
Slope Fig. 2 $(\frac{\alpha_{\text{2-ROOH}} \cdot k_{\text{2-RO2+HO2}}}{k_{\text{1,8 H-shift, 2-RO2}}})$	slope fit Fig. 2 (1.0%), $\frac{[2-ROOH]}{\text{[all products from 2-OO-5-ROOH]}}$ (28%), [HO_2] (16%)		$(1.32 \pm 0.43) \times 10^{-11}$
$k_{\text{1,8 H-shift, 2-RO}_2}$	$\alpha_{\text{2-ROOH}} k_{\text{2-RO}_2+\text{HO}_2}$/(slope Fig. 2)	slope Fig. 2 (32%), $\alpha_{\text{2-ROOH}}$ (39%), $k_{RO_2+HO_2}$ (52%)[a]	1.17 ± 0.85
Slope Fig. 3 $(\frac{k_{\text{1,5 H-shift, 2-OO-5-ROOH}}}{\alpha_{\text{2,5-DiROOH}} \cdot k_{\text{2-OO-5-ROOH+HO2}}})$	slope fit Fig. 3 (2.9%), $\frac{\text{[2-oxo-5-ROOH]}}{\text{[2,5-DiROOH]}}$ (28%), [HO_2] (16%)		$(1.24 \pm 0.40) \times 10^{9}$
Intercept Fig. 3 $(\frac{\alpha_{\text{2-oxo-5-ROOH}}}{\alpha_{\text{2,5-DiROOH}}})$	intercept fit Fig. 3 (2.6%), $\frac{\text{[2-oxo-5-ROOH]}}{\text{[2,5-DiROOH]}}$ (28%)		0.39 ± 0.11
$\frac{\alpha_{\text{2-O-5-ROOH}}}{\alpha_{\text{2,5-DiROOH}}}$	$\frac{\text{[2-OOH-R'CHO]}}{\text{[2,5-DiROOH]}}$ (28%)		0.14 ± 0.04
$\alpha_{\text{2,5-DiROOH}}$	$\frac{1}{1+\frac{\alpha_{\text{2-oxo-5-ROOH}}}{\alpha_{\text{2,5-DiROOH}}}+\frac{\alpha_{\text{2-O-5-ROOH}}}{\alpha_{\text{2,5-DiROOH}}}}$		0.65 ± 0.09
$\alpha_{\text{2-oxo-5-ROOH}}$	$\alpha_{\text{2,5-DiROOH}} \times \frac{\alpha_{\text{2-oxo-5-ROOH}}}{\alpha_{\text{2,5-DiROOH}}}$	$\alpha_{\text{2,5-ROOH}}$ (14%), $\frac{\alpha_{\text{2-oxo-5-ROOH}}}{\alpha_{\text{2,5-DiROOH}}}$ (28%)	0.26 ± 0.07

Quantity	Constraints	Sources of Uncertainty	Value
$\alpha_{\text{2-O-5-ROOH}}$	$\alpha_{\text{2,5-DiROOH}} \times \frac{\alpha_{\text{2-O-5-ROOH}}}{\alpha_{\text{2,5-DiROOH}}}$	$\alpha_{\text{2,5-DiROOH}}$ (14%), $\frac{\alpha_{\text{2-O-5-ROOH}}}{\alpha_{\text{2,5-DiROOH}}}$ (28%)	0.09 ± 0.02
$k_{\text{1,8 H-shift, 2-OO-5-ROOH}}$	(slope Fig. 3)$\times\alpha_{\text{2,5-DiROOH}} k_{\text{2-OO-5-ROOH+HO}_2}$	slope Fig. 3 (32%), $\alpha_{\text{2,5-DiROOH}}$ (14%), $k_{RO_2+HO_2}$ (52%)	0.017 ± 0.011
Slope Fig. S33b ($\frac{k_{\text{1,6 H-shift, (2,4)-OOROOH average}}}{\alpha_{\text{2,4-DiROOH, average}} \cdot k_{\text{(2,4)-OOROOH+HO2}}}$)	slope fit Fig. S33b (1.8%), $\frac{\text{[2-oxo-4-ROOH]+[4-oxo-2-ROOH]}}{\text{[2,4-DiROOH]}}$ (28%), [HO_2] (16%)		$(2.98 \pm 0.96) \times 10^9$
Intercept Fig. S33b ($\frac{\alpha_{\text{(2,4)-oxo-ROOH, average}}}{\alpha_{\text{2,4-DiROOH, average}}}$)	intercept fit Fig. S33 (8.8%), $\frac{\text{[2-oxo-4-ROOH]+[4-oxo-2-ROOH]}}{\text{[2,4-DiROOH]}}$ (28%)		0.16 ± 0.05
$\alpha_{\text{2,4-DiROOH,2-OO-4-ROOH}}$	$\frac{\alpha_{\text{(2,4)-oxo-ROOH, average}}}{\alpha_{\text{2,4-DiROOH, average}}}$ (29%), $\frac{\alpha_{\text{2-O-4-ROOH}}}{\alpha_{\text{2,4-DiROOH, 2-OO-4-ROOH}}}$ (28%), $\frac{\text{[4-oxo-2-ROOH]}}{\text{[2-oxo-4-ROOH]}}$ (28%)		0.80 ± 0.07
$\alpha_{\text{2-oxo-4-ROOH}}$			0.10 ± 0.04
$\alpha_{\text{2-O-4-ROOH}}$			0.10 ± 0.03
$\alpha_{\text{2,4-DiROOH, 4-OO-2-ROOH}}$			0.64 ± 0.26
$\alpha_{\text{4-oxo-2-ROOH}}$			0.13 ± 0.05
$\alpha_{\text{4-O-2-ROOH}}$			0.23 ± 0.21
$k_{\text{1,6 H-shift, (2,4)-OOROOH average}}$	(slope Fig. S33b) $\times\alpha_{\text{2,4-DiROOH, average}} k_{\text{(2,4)-OOROOH+HO}_2}$	slope Fig. 3 (32%), $k_{RO_2+HO_2}$ (52%)[a], $\alpha_{\text{2,4-DiROOH, average}}$ (14%)	0.045 ± 0.028
Slope Fig. S34 ($\frac{k_{RO_2+HO_2}}{k_{\text{1,6 H-shift, 2-RO2 \& 3-RO2}}}$)	slope fit Fig. S34 (2.6%), Ratios from Equation S26 (28%), [HO_2] (16%)		$(1.10 \pm 0.35)\times10^{-10}$
$k_{\text{1,6 H-shift, 2-RO}_2\text{\&3-RO}_2}$	$k_{RO_2+HO_2}$/(slope Fig. S34)	slope Fig. S34 (32%), $k_{RO_2+HO_2}$ (52%)[a]	0.18 ± 0.11

References

(1) Jenkin, M. E.; Valorso, R.; Aumont, B.; Rickard, A. R.; Wallington, T. J. Estimation of rate coefficients and branching ratios for gas-phase reactions of OH with aliphatic organic compounds for use in automated mechanism construction. *Atmospheric Chemistry and Physics* **2018**, *18*, 9297–9328.

(2) Kwok, E. S.; Atkinson, R. Estimation of hydroxyl radical reaction rate constants for gas-phase organic compounds using a structure-reactivity relationship: An update. *Atmospheric Environment* **1995**, *29*, 1685–1695.

(3) Jenkin, M. E.; Valorso, R.; Aumont, B.; Rickard, A. R. Estimation of rate coefficients and branching ratios for reactions of organic peroxy radicals for use in automated mechanism construction. *Atmospheric Chemistry and Physics* **2019**, *19*, 7691–7717.

(4) Su, T.; Chesnavich, W. J. Parametrization of the ion-polar molecule collision rate constant by trajectory calculations. *J. Chem. Phys* **1982**, *76*, 5183.

(5) Garden, A. L.; Paulot, F.; Crounse, J. D.; Maxwell-Cameron, I. J.; Wennberg, P. O.; Kjaergaard, H. G. Calculation of conformationally weighted dipole moments useful in ion–molecule collision rate estimates. *Chemical Physics Letters* **2009**, *474*, 45–50.

(6) Møller, K. H.; Otkjær, R. V.; Hyttinen, N.; Kurtén, T.; Kjaergaard, H. G. Cost-Effective Implementation of Multiconformer Transition State Theory for Peroxy Radical Hydrogen Shift Reactions. *Journal of Physical Chemistry A* **2016**, *120*, 10072–10087.

(7) Zhao, Q.; Møller, K. H.; Chen, J.; Kjaergaard, H. G. Cost-effective implementation of multiconformer transition state theory for alkoxy radical unimolecular reactions. *The Journal of Physical Chemistry A* **2022**, *126*, 6483–6494.

(8) Møller, K. H.; Bates, K. H.; Kjaergaard, H. G. The importance of peroxy radical hydrogen-shift reactions in atmospheric isoprene oxidation. *The Journal of Physical Chemistry A* **2019**, *123*, 920–932.

(9) Short, M. A.; Blackburn, J. M.; Roizen, J. L. Sulfamate Esters Guide Selective Radical-Mediated Chlorination of Aliphatic C- H Bonds. *Angewandte Chemie International Edition* **2018**, *57*, 296–299.

(10) Short, M. A.; Shehata, M. F.; Sanders, M. A.; Roizen, J. L. Sulfamides direct radical-mediated chlorination of aliphatic C–H bonds. *Chemical Science* **2020**, *11*, 217–223.

(11) De Vleeschouwer, F.; Van Speybroeck, V.; Waroquier, M.; Geerlings, P.; De Proft, F. Electrophilicity and nucleophilicity index for radicals. *Organic letters* **2007**, *9*, 2721–2724.

(12) Hao, Z.; Ai, W.; Su, N. Q. Unveiling the Delicate Balance of Polarity and Strain Effect in Determining the Site-Selective Intramolecular Hydrogen Atom Transfers. *The Journal of Physical Chemistry A* **2025**.

(13) Roberts, B. P. Polarity-reversal catalysis of hydrogen-atom abstraction reactions: concepts and applications in organic chemistry. *Chemical Society Reviews* **1999**, *28*, 25–35.

(14) Garwood, J. J.; Chen, A. D.; Nagib, D. A. Radical polarity. *Journal of the American Chemical Society* **2024**, *146*, 28034–28059.

(15) Parr, R. G.; Szentpály, L. v.; Liu, S. Electrophilicity index. *Journal of the American Chemical Society* **1999**, *121*, 1922–1924.

(16) Parr, R. G.; Donnelly, R. A.; Levy, M.; Palke, W. E. Electronegativity: the density functional viewpoint. *The Journal of chemical physics* **1978**, *68*, 3801–3807.

(17) Parr, R. G.; Pearson, R. G. Absolute hardness: companion parameter to absolute electronegativity. *Journal of the American chemical society* **1983**, *105*, 7512–7516.

(18) Parr, R. G.; Yang, W. Density functional approach to the frontier-electron theory of chemical reactivity. *Journal of the American Chemical Society* **1984**, *106*, 4049–4050.

(19) Yang, W.; Mortier, W. J. The use of global and local molecular parameters for the analysis of the gas-phase basicity of amines. *Journal of the American Chemical Society* **1986**, *108*, 5708–5711.

(20) Reed, A. E.; Weinstock, R. B.; Weinhold, F. Natural population analysis. *The Journal of chemical physics* **1985**, *83*, 735–746.

(21) Domingo, L. R.; Pérez, P. Global and local reactivity indices for electrophilic/nucleophilic free radicals. *Organic & biomolecular chemistry* **2013**, *11*, 4350–4358.

(22) Johnson, E. R.; Keinan, S.; Mori-Sánchez, P.; Contreras-García, J.; Cohen, A. J.; Yang, W. Revealing noncovalent interactions. *Journal of the American Chemical Society* **2010**, *132*, 6498–6506.

(23) Contreras-García, J.; Yang, W.; Johnson, E. R. Analysis of hydrogen-bond interaction potentials from the electron density: integration of noncovalent interaction regions. *The Journal of Physical Chemistry A* **2011**, *115*, 12983–12990.

(24) Lu, T.; Chen, F. Multiwfn: A multifunctional wavefunction analyzer. *Journal of computational chemistry* **2012**, *33*, 580–592.

(25) Lu, T. A comprehensive electron wavefunction analysis toolbox for chemists, Multiwfn. *The Journal of chemical physics* **2024**, *161*.

(26) Bader, R. F. Atoms in molecules. *Accounts of chemical research* **1985**, *18*, 9–15.

(27) Badenhoop, J.; Weinhold, F. Natural bond orbital analysis of steric interactions. *The Journal of chemical physics* **1997**, *107*, 5406–5421.

(28) Badenhoop, J.; Weinhold, F. Natural steric analysis of internal rotation barriers. *International journal of quantum chemistry* **1999**, *72*, 269–280.

(29) Dos Passos Gomes, G.; Terent'ev, A.; Alabugin, I. V., et al. Stereoelectronic source of the anomalous stability of bis-peroxides. *Chemical science* **2015**, *6*, 6783–6791.

(30) Alabugin, I. V.; dos Passos Gomes, G.; Abdo, M. A. Hyperconjugation. *Wiley Interdisciplinary Reviews: Computational Molecular Science* **2019**, *9*, e1389.

(31) Alabugin, I. V.; Kuhn, L.; Medvedev, M. G.; Krivoshchapov, N. V.; Vil, V. A.; Yaremenko, I. A.; Mehaffy, P.; Yarie, M.; Terent'ev, A. O.; Zolfigol, M. A. Stereoelectronic power of oxygen in control of chemical reactivity: the anomeric effect is not alone. *Chemical Society Reviews* **2021**, *50*, 10253–10345.

(32) David, S.; Eisenstein, O.; Hehre, W. J.; Salem, L.; Hoffmann, R. Superjacent orbital control. Interpretation of the anomeric effect. *Journal of the American Chemical Society* **1973**, *95*, 3806–3807.

(33) Calvert, J. G.; Mellouki, A.; Orlando, J. J.; Pilling, M. J.; Wallington, T. J., *The Mechanisms of Atmospheric Oxidation of the Oxygenates*; Oxford University Press, Inc.: 2011.

(34) Keller-Rudek, H.; Moortgat, G. K.; Sander, R.; Sörensen, R. The MPI-Mainz UV/VIS spectral atlas of gaseous molecules of atmospheric interest. *Earth System Science Data* **2013**, *5*, 365–373.

(35) Murphy, S. E.; Crounse, J. D.; Møller, K. H.; Rezgui, S. P.; Hafeman, N. J.; Park, J.; Kjaergaard, H. G.; Stoltz, B. M.; Wennberg, P. O. Accretion product formation in the self-reaction of ethene-derived hydroxy peroxy radicals. *Environmental Science: Atmospheres* **2023**, *3*, 882–893.

(36) Yu, H.; Møller, K. H.; Buenconsejo, R. S.; Crounse, J. D.; Kjaergaard, H. G.; Wennberg, P. O. Atmospheric Photo-Oxidation of 2-Ethoxyethanol: Autoxidation Chemistry of Glycol Ethers. *The Journal of Physical Chemistry A* **2023**, *127*, 9579.

(37) Liu, Z.; Nguyen, V. S.; Harvey, J.; Müller, J. F.; Peeters, J. The photolysis of α-hydroperoxycarbonyls. *Physical Chemistry Chemical Physics* **2018**, *20*, 6970–6979.

(38) Yeh, G. K.; Ziemann, P. J. Gas-wall partitioning of oxygenated organic compounds: Measurements, structure-activity relationships, and correlation with gas chromatographic retention factor. *Aerosol Science and Technology* **2015**, *49*, 727–738.

(39) Huang, Y.; Zhao, R.; Charan, S. M.; Kenseth, C. M.; Zhang, X.; Seinfeld, J. H. Unified Theory of Vapor-Wall Mass Transport in Teflon-Walled Environmental Chambers. *Environmental Science and Technology* **2018**, *52*, 2134–2142.

(40) Zhang, X.; Schwantes, R. H.; McVay, R. C.; Lignell, H.; Coggon, M. M.; Flagan, R. C.; Seinfeld, J. H. Vapor wall deposition in Teflon chambers. *Atmospheric Chemistry and Physics* **2015**, *15*, 4197–4214.

(41) Yu, H.; Chen, J.; Crounse, J. D.; Almeida, T. G.; Kjaergaard, H. G.; Wennberg, P. O. Atmospheric Autoxidation Chemistry of Diethyl Ether. *ACS ES&T Air* **2025**.

(42) Vakhtin, A. B.; McCabe, D. C.; Ravishankara, A. R.; Leone, S. R. Low-Temperature Kinetics of the Reaction of the OH Radical with Hydrogen Peroxide†. *Journal of Physical Chemistry A* **2003**, *107*, 10642–10647.

(43) Burkholder, J. B.; Sander, S. P.; Abbatt, J. P. D.; Barker, J. R.; Huie, R. E.; Kolb, C. E.; Kurylo, M. J.; Orkin, V. L.; Wilmouth, D. M.; Wine, P. H. Chemical Kinetics and Photochemical Data for Use in Atmospheric Studies, Evaluation No. 19. *JPL Publications 19-5* **2020**, 1–153.